DETECTING AND UNDERSTANDING CLIMATE CHANGE USING HYPERSPECTRAL RADIATIVE MEASUREMENTS

LEI LIU

Department of Atmospheric and Oceanic Sciences

McGill University, Montreal

JUNE, 2024

A thesis submitted to McGill University in partial fulfillment of

the requirements of the degree of

DOCTOR OF PHILOSOPHY

TABLE OF CONTENTS

ABSTRACT

Unraveling the complexities of climate change hinges on a detailed analysis of Earth's energy balance and associated atmospheric processes, tasks for which hyperspectral radiative instruments are particularly suited. These instruments not only facilitate a comprehensive evaluation of energy balance changes by leveraging their sensitivity to key meteorological variables but also enable the disentanglement of various contributing factors. Moreover, retrieving atmospheric profiles from these measurements provides a comprehensive view of climate change, capturing its impacts across different atmospheric levels.

This thesis mainly involves two hyperspectral instruments: the Atmospheric Emitted Radiance Interferometer (AERI), which measures the downwelling longwave radiance (DLR) emitted by the atmosphere at ground level in the infrared spectral range, and the High Spectral Resolution Airborne Microwave Sounder (HiSRAMS), designed for measuring microwave radiation and adaptable for use on research aircraft or at the surface. These instruments, with their high spectral resolutions, offer a multidimensional perspective on climate change.

The objective of this thesis is to detect and understand climate change using hyperspectral radiative measurements from AERI and HiSRAMS. This goal is approached from two perspectives: radiative observations, which involve analyzing the spectral signals of various climate change agents and the evolution of the Earth's energy balance, and the application of hyperspectral radiative measurements to retrieve key atmospheric variables for further climate change analysis. Our objectives include obtaining a long-term DLR record from AERI observations at the Southern Great Plains (SGP) site and detecting and separating climate change signals. Additionally, we aim to address the radiometric accuracy of HiSRAMS measurements

and perform retrievals of temperature and water vapor concentrations using both AERI and HiSRAMS measurements under clear-sky conditions.

For long-term climate change detection, we homogenize a 23-year DLR record observed by two AERIs at the SGP site, which includes an overlapping 10-year observational period. A neural network classifies the DLR spectra into distinct sky conditions: clear-sky, thin-cloud, and thick-cloud conditions. Employing a weighted linear regression model that incorporates a first-order autoregressive process, we determine unique long-term DLR trends across various AERI channels and sky conditions. The spectral characteristics of these DLR trends reflect the impact of varying meteorological variables. For example, we identify significant positive DLR trends in temperature-sensitive channels, indicative of atmospheric warming, particularly at the surface due to strong absorption in these channels. Interestingly, we observe DLR trends with different signs in the window band between all-sky and clear-sky conditions, implying the significant impact of clouds on the longwave surface energy balance. Our study also highlights the early detectability of climate change in weak absorption channels and suggests that the primary source of uncertainty in DLR trends at the SGP site arises from internal climate variability, rather than measurement errors, emphasizing the importance of continuous spectrally resolved DLR observations for climate change detection and attribution.

In terms of atmospheric profiling capabilities, we conduct a comparative assessment of radiative accuracy and performance in temperature and water vapor retrievals between AERI and HiSRAMS under clear-sky conditions based on three field campaigns carried out in Ottawa, Canada. HiSRAMS's radiative accuracy is initially assessed against AERI through radiative closure tests. We compare the relationship between radiometric biases determined from the radiative closure tests and total column optical depth within the instrument's viewing geometry to assess the radiative accuracy of different instruments. Radiative closure results indicate that the radiative accuracy of HiSRAMS's nadir-pointing measurements is comparable to that of corrected AERI observations, which remove the warm bias detected in the window band. Nonetheless, the zenith-pointing measurements from HiSRAMS exhibit relatively lower radiative accuracy. We further adopt an optimal estimation method to simultaneously retrieve clear-sky temperature and water vapor concentration profiles utilizing AERI and HiSRAMS measurements. AERI demonstrates better retrieval performance in terms of degree of freedom of signal (DFS), retrieval uncertainty, and the resolvability of fine vertical features in temperature and water vapor when adopting ground-based zenith-pointing measurements only. A synergy of HiSRAMS nadir-pointing hyperspectral measurement at high altitude and AERI ground-based zenith-pointing hyperspectral measurement increases the DFS and reduces the retrieval uncertainty in both temperature and water vapor retrievals.

This thesis underscores the critical role of hyperspectral radiative measurements in detecting and understanding the multifaceted nature of climate change, providing insights into atmospheric mechanisms driving changes and enhancing our ability to monitor and predict climate change.

ABRÉGÉ

Comprendre les complexités du changement climatique repose sur une analyse détaillée de la balance énergétique de la Terre et des processus atmosphériques associés, des tâches pour lesquelles les instruments radiatifs hyperspectraux sont particulièrement adaptés. Ces instruments facilitent non seulement une évaluation complète des changements de balance énergétique en exploitant leur sensibilité aux variables météorologiques clés, mais permettent également de démêler les différents facteurs contributifs. De plus, l'extraction de profils atmosphériques à partir de ces mesures offre une vue complète du changement climatique, capturant ses impacts à différents niveaux atmosphériques.

Cette thèse implique principalement deux instruments hyperspectraux : l'Atmospheric Emitted Radiance Interferometer (AERI), qui mesure la radiance à longue onde descendante (RLOD) émise par l'atmosphère vers le sol dans la gamme spectrale infrarouge, et le High Spectral Resolution Airborne Microwave Sounder (HiSRAMS), conçu pour mesurer le rayonnement micro-onde et adaptable pour une utilisation au sol ou sur des avions de recherche. Ces instruments, de par leurs hautes résolutions spectrales, offrent une perspective multidimensionnelle sur le changement climatique.

L'objectif de cette thèse est de détecter et de comprendre le changement climatique en utilisant des mesures radiatives hyperspectrales d'AERI et de HiSRAMS. Cet objectif est abordé sous deux perspectives : les observations radiatives, qui impliquent l'analyse des signaux spectraux de divers agents du changement climatique et l'évolution du bilan énergétique de la Terre, et l'application des mesures radiatives hyperspectrales pour obtenir des variables atmosphériques clés pour une analyse plus approfondie du changement climatique. Nos objectifs incluent l'obtention d'un enregistrement à long terme du RLOD à partir des observations d'AERI sur le site des Southern Great Plains (SGP) et la détection et la séparation des signaux de changement climatique. De plus, nous visons à aborder la précision radiométrique des mesures de HiSRAMS et à effectuer des récupérations de la température et des concentrations de vapeur d'eau en utilisant les mesures d'AERI et de HiSRAMS dans des conditions ciel dégagé.

Pour la détection du changement climatique à long terme, nous homogénéisons un enregistrement RLOD de 23 ans observé par deux AERI sur le site des SGP, qui comprend une période d'observation superposée de 10 ans. Un réseau de neurones classe les spectres RLOD en fonction de la condition nuageuse: ciel dégagé, nuages minces et conditions de nuages épais. En utilisant un modèle de régression linéaire pondérée qui intègre un processus autorégressif du premier ordre, nous déterminons les tendances RLOD à long terme uniques à travers divers canaux AERI et conditions nuageuses. Les caractéristiques spectrales de ces tendances RLOD reflètent l'impact de multiples variables météorologiques. Par exemple, nous identifions des tendances RLOD positives significatives dans les canaux sensibles à la température, indicatives d'un réchauffement atmosphérique, en particulier à la surface en raison d'une forte absorption dans ces canaux. De manière intéressante, nous observons des tendances RLOD avec des signes différents dans la fenêtre atmosphérique entre toutes les conditions nuageuses, impliquant l'impact significatif des nuages sur la balance énergétique de surface à onde longue. Notre étude met également en évidence la détectabilité précoce du changement climatique dans les canaux de faible absorption et suggère que la principale source d'incertitude dans les tendances RLOD sur le site SGP provient de la variabilité climatique interne, plutôt que des erreurs de mesure, soulignant l'importance des observations RLOD résolues spectralement pour la détection et l'attribution du changement climatique.

En termes de capacités de profilage atmosphérique, nous réalisons une évaluation comparative de la précision radiative et de la performance dans les récupérations de température et de vapeur d'eau entre AERI et HiSRAMS dans des conditions de ciel clair, basée sur trois campagnes sur le terrain menées à Ottawa, Canada. La précision radiative de HiSRAMS est initialement évaluée par rapport à AERI à travers des tests de fermeture radiative. Nous comparons la relation entre les biais radiométriques déterminés à partir des tests de fermeture radiative et la profondeur optique de la colonne totale dans la géométrie de visualisation de l'instrument pour évaluer la précision radiative de différents instruments. Les résultats de la fermeture radiative indiquent que la précision radiative des mesures de HiSRAMS pointant vers le nadir est comparable à celle des observations AERI corrigées, qui éliminent le biais chaud détecté dans la fenêtre atmosphérique. Néanmoins, les mesures pointant vers le zénith de HiSRAMS présentent une précision radiative relativement inférieure. Nous adoptons en outre la méthode d'estimation optimale pour récupérer simultanément les profils de température et de concentration de vapeur d'eau sous un ciel clair en utilisant les mesures de AERI et HiSRAMS. AERI démontre une meilleure performance de récupération en termes de degré de liberté du signal (DLS), d'incertitude de récupération et de la résolvabilité des caractéristiques verticales fines en température et en vapeur d'eau lors de l'adoption de mesures hyperspectrales au sol pointant uniquement vers le zénith. Une synergie des mesures hyperspectrales de HiSRAMS pointant vers le nadir à haute altitude et des mesures hyperspectrales au sol de AERI pointant vers le zénith augmente le DLS et réduit l'incertitude de récupération à la fois dans les récupérations de température et de vapeur d'eau.

Cette thèse souligne le rôle critique des mesures radiatives hyperspectrales dans la détection et la compréhension de la nature multifacette du changement climatique, fournissant des aperçus des mécanismes atmosphériques entraînant des changements et améliorant notre capacité à surveiller et à prédire le changement climatique.

ACKNOWLEDGMENTS

First and foremost, I would like to express my deepest gratitude to my supervisors, Prof. Yi Huang and Prof. John Gyakum, for their invaluable guidance and patience throughout my Ph.D. studies. They afforded me the precious freedom to explore topics of my interest while being readily available for support and guidance. My Ph.D. journey, enriched by opportunities to delve into instrument operation and scientific inquiries, was made possible by their backing. I had the privilege of participating in several field campaigns focusing on different hyperspectral instruments, including weather balloon launchings. I cannot thank Yi and John enough for not only fostering a positive working environment but also exemplifying the qualities of outstanding mentors.

My Ph.D. thesis could not have been realized without the contributions of all my collaborators, including Dr. David Turner, Dr. Jonathan Gero, Natalia Bliankinshtein, Dr. Philip Gabriel, Shiqi Xu, and Dr. Mengistu Wolde. I extend my thanks to Prof. Andreas Zuend for serving as a member of my Ph.D. committee.

It was not until I immersed myself in the work that I fully appreciated the myriad of challenges that can arise during instrument operations, a process that proved to be profoundly educational. I am especially thankful to Dr. Jonathan Gero for his continuous suggestions and guidance in troubleshooting the instrument and analyzing data. My gratitude also goes to Natalia Bliankinshtein for her companionship during the various field campaigns we undertook together, braving all manner of weather conditions. I would like to acknowledge the McGill operations team as well as the Airborne Facilities for Atmospheric Research and Reconnaissance (AFARR) team from the National Research Council of Canada, for their efforts in data collection for this thesis.

I extend my thanks to the former and current members of both the Atmospheric Radiation Group and the Synoptic-Dynamic Meteorology Group at McGill, who provided valuable feedback on my work. Special thanks to Jing Feng, Yuwei Wang, Qiurun Yu, Han Huang, and Ruogu He for their friendship and companionship throughout my Ph.D. studies.

I am deeply grateful to my partner and friends in both China and Canada who supported me through all the challenging times. Their unwavering support is the cornerstone of my ability to complete this thesis.

Last but certainly not least, I owe a debt of gratitude to my family, and most importantly, to my parents, Huiling Li and Xianyong Liu, and my sister, Ying Liu, for their endless support over the years. This thesis is dedicated to them.

CONTRIBUTION TO ORIGINAL KNOWLEDGE

1. A comprehensive homogenization of the long-term downwelling longwave radiance (DLR) record, as observed by the Atmospheric Emitted Radiance Interferometer (AERI) at the Southern Great Plains (SGP) site, has been conducted. This effort has resulted in a "hyperspectral radiative Keeling Curve," establishing a solid foundation for climate change detection and attribution analysis. Long-term trends across all AERI channels have been analyzed under various sky conditions, enabling the extraction of distinct pieces of climate change information.
2. Participation in the design and operation of three field campaigns in Ottawa, Canada, marked the first effort to collect collocated measurements from hyperspectral infrared and microwave radiometers, alongside radiosonde observations. The data from these campaigns provide a unique opportunity to systematically assess the radiometric accuracy of the newly developed hyperspectral microwave radiometer, the High Spectral Resolution Airborne Microwave Sounder, for the first time. Furthermore, these data allow for the testing of clear-sky temperature and water vapor retrieval capabilities using the hyperspectral microwave radiometer.
3. A novel method has been proposed to assess the radiative accuracy of various hyperspectral instruments operating across different spectral ranges. This method is based on correlating the radiative bias, derived from radiative closure analysis, with the total column optical depth, as observed within the view geometry of the hyperspectral radiometer. It offers a straightforward yet effective approach to comparing the radiometric accuracy of different hyperspectral radiometers.

4. Retrieval algorithms for clear-sky temperature and water vapor, tailored to AERI measurements, have been developed. Additionally, a synergistic retrieval algorithm that utilizes both AERI and HiSRAMS hyperspectral measurements has been introduced. Infrared hyperspectral measurements offer a higher information content and superior vertical resolution for the retrieval of temperature and water vapor profiles compared to their microwave counterparts. The integration of ground-based infrared and airborne microwave hyperspectrometers provides a significant advantage for accurate sounding of temperature and water vapor profiles.

CONTRIBUTION OF AUTHORS

This thesis comprises five chapters: an introductory chapter, two peer-reviewed manuscripts presented in Chapters 2 and 3, one submitted manuscript included in Chapter 4, and a concluding chapter. Chapters 2 and 3 have been published in the *Journal of Geophysical Research-Atmospheres* and *Atmospheric Measurement Techniques*, respectively. Chapter 4 is currently under review in *Atmospheric Measurement Techniques*.

The thesis author served as the main investigator for all three research manuscripts, with contributions from collaborators. In each case, the thesis author carried out the primary analysis under the supervision of Prof. Yi Huang and Prof. John Gyakum, and wrote the manuscripts with incorporated insights and revisions from all co-authors.

For the first work, Yi Huang conceived the research. Lei Liu, Yi Huang, John Gyakum, David Turner, and Jonathon Gero co-developed the AERI data processing workflow. Lei Liu performed the analysis and led the writing of the manuscript, with contributions from all co-authors.

For the second work, Yi Huang conceived the research. Yi Huang, John Gyakum, Natalia Bliankinshtein, Philip Gabriel, and Mengistu Wolde co-designed the measurement experiment. Lei Liu and Yi Huang developed the AERI forward model and performed AERI data collection and analysis. Natalia Bliankinshtein and Philip Gabriel developed HiSRAMS forward model; Natalia Bliankinshtein, Philip Gabriel, and Shiqi Xu performed HiSRAMS data collection and analysis. Lei Liu led the writing of the manuscript with contributions from all co-authors.

For the third work, Yi Huang, Natalia Bliankinshtein, John Gyakum, and Mengistu Wolde conceived the research. Natalia Bliankinshtein, Lei Liu, Shiqi Xu and Yi Huang conducted the field data collection. Lei Liu developed the AERI retrieval algorithm. Natalia

Bliankinshtein and Philip Gabriel, with modifications provided by Lei Liu, developed the HiSRAMS retrieval algorithm. Furthermore, Lei Liu developed the joint retrieval algorithm. Lei Liu led the manuscript writing process, with contributions from all co-authors.

LIST OF FIGURES

LIST OF TABLES

Chapter 1 INTRODUCTION

The widespread influence and complex nature of climate change demand thorough investigation and analysis. Detecting and understanding its patterns is one of the central tasks toward enhancing our capabilities in monitoring and predicting climate change. As the planet navigates the consequences of climate change, the interrelated changes in Earth's energy balance and atmospheric conditions play a pivotal role, acting to either amplify or mitigate global warming, characterized by the surface air temperature increases.

The climate forcing and feedback framework, described by Equation 1.1, has been widely used to systematically understand and predict the climate change. This framework, which can be applied at both the top-of-atmosphere (TOA, Huang, 2013b; Soden et al., 2008) and at the surface (Andrews et al., 2009; Colman, 2015), quantitatively connects shifts in the Earth's energy balance—represented by the energy imbalance (ΔN), radiative forcing perturbation (ΔF), and surface air temperature change (ΔT_s).

$$\Delta N = \Delta F + \lambda \Delta T_s \tag{1.1}$$

Here, λ is defined as the climate feedback parameter, reflecting the sensitivity of the climate system to external changes. Feedback mechanisms, which involves climate system factors such as water vapor, atmospheric temperature, cloud, and surface albedo, are closely monitored for their relationship with energy imbalance and surface air temperature changes, as shown in Equation 1.2. In this equation, λ_i quantifies the specific feedback parameter associated with changes in the climate system factor x_i.

$$\lambda_i = \frac{\partial N}{\partial x_i} \times \frac{\partial x_i}{\partial T_s} \tag{1.2}$$

In summary, the climate forcing and feedback framework underscores the importance of closely monitoring and analyzing Earth's energy balance and atmospheric states to detect and understand climate change. Within this context, hyperspectral radiative instruments are invaluable for their ability to monitor the evolution of the Earth's energy budget and retrieve key atmospheric variables. These capabilities enable the detailed observation and analysis necessary to bridge critical areas in climate science.

1.1 Climate change and Earth's energy balance

Earth's energy balance represents that the energy entering Earth should be in equilibrium with the energy exiting Earth, which plays a pivotal role in regulating the global climate. This balance can be analyzed at various levels: the TOA (e.g., Harries et al., 2001; Huang & Ramaswamy, 2009; Loeb et al., 2018; Wielicki et al., 2002), the surface (e.g., Wild et al., 2012), and within the atmosphere (e.g., Lin et al., 2008). Under equilibrium, all energy budgets at these levels are balanced. However, disturbances such as the greenhouse effect, driven by increased greenhouse gas emissions, disrupt this balance, leading to climate changes like surface warming. Monitoring the changes of Earth's energy balance is crucial for detecting climate change (Loeb et al., 2016).

The energy entering and exiting the Earth is in the form of electromagnetic energy, as shown in Figure 1.1. The electromagnetic spectrum illustrates the energy distribution across different wavelengths, i.e. different wavenumbers or frequencies. This distribution underlies the operation of hyperspectral instruments, which are devices capable of measuring radiance with high spectral resolution. Energy balances at various levels consist of distinct components, primarily categorized by their wavelengths into longwave and shortwave radiation. Changes in each component have significant implications for climate change.

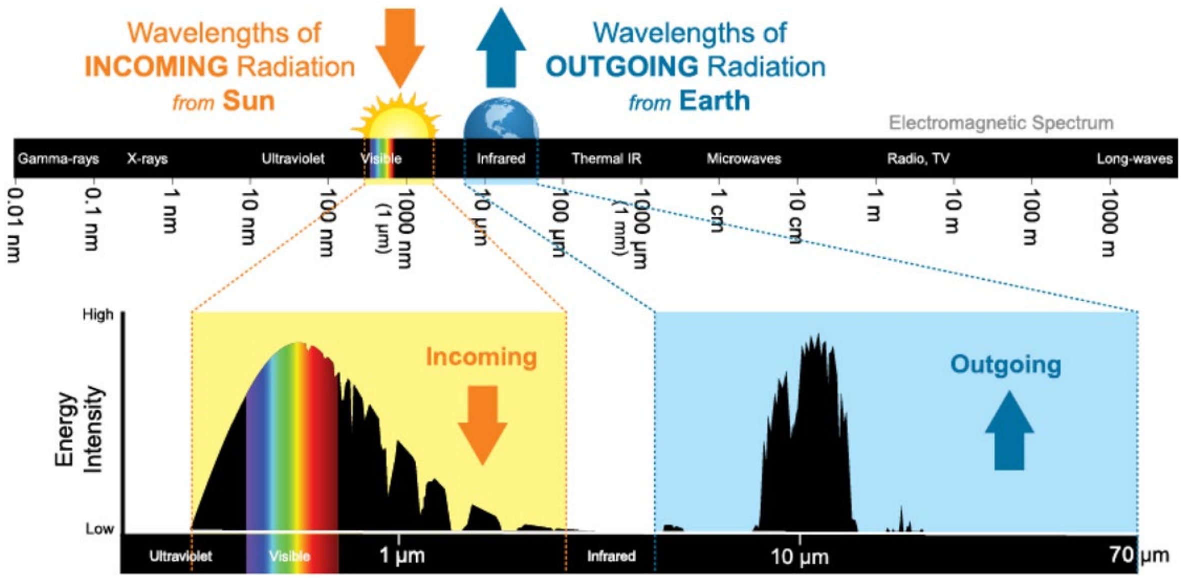

Figure 1.1 The schematic of electromagnetic spectrum, obtained from https://www.noaa.gov/jetstream/satellites/absorb.

1.2 Climate change and atmospheric thermodynamic states

Atmospheric soundings, including temperature and water vapor vertical profiles, are vital for understanding Earth's energy balance and weather systems (Cess, 1974; Guo et al., 2020; Laroche & Sarrazin, 2010; Thorne et al., 2011; Wang et al., 2016), necessitating continuous monitoring for climate change detection and understanding. Long-term monitoring of these profiles not only provides direct signals of climate change (Allan et al., 2022; Vuille & Bradley, 2000; Zhou et al., 2021) but also informs atmospheric diagnostics like stability and radiation analysis (Doherty & Newell, 1984; Toporov & Löhnert, 2020).

Radiosondes offer one of the most accurate atmospheric state measurements. However, there are challenges like drifting issues and limited temporal and spatial coverages. With global climate change, there is a need for vertical temperature and water vapor profiles in high temporal and spatial resolutions to improve weather forecasts and climate monitoring.

1.3 Hyperspectral radiative instruments in climate research

Hyperspectral instruments, observing Earth's radiation at high spectral and temporal resolutions, can be utilized to monitor Earth's energy balance (Gero and Turner, 2011; Loeb et al., 2018; Palchetti et al., 2020; Wielicki et al., 2002) and retrieve atmospheric states (Aires et al., 2015; Blackwell et al., 2010; Clerbaux et al., 2009; Susskind et al., 2010; Turner & Blumberg, 2018). Various hyperspectral instruments typically span specific spectral ranges of Earth's radiation. This is often considered as a criterion to classify these instruments, such as infrared and microwave hyperspectrometers. Depending on the deployment location of an instrument, it is possible to analyze the energy balance across different vertical levels and retrieve atmospheric profiles within the instrument's viewing geometry. For instance, an infrared hyperspectrometer stationed at the surface can be utilized to monitor the downwelling longwave radiance (DLR) emitted by the atmosphere.

The utilization of hyperspectral instruments in climate research is grounded in the distinct absorption characteristics of atmospheric gases. Figure 1.2 illustrates the spectral signatures of different atmospheric components within the DLR as observed from the Earth's surface. These unique spectral responses enable the attribution of total climate change signals to various contributors within the energy balance analysis, as well as the retrieval of atmospheric profiles. In terms of energy balance analysis, spectrally resolved observations provide not only a broadband understanding of Earth's radiation but also facilitate the disentanglement of the total climate change signals into contributions from different meteorological variables (Brindley & Bantges, 2016; Hilton et al., 2012; Huang & Ramaswamy, 2009). For the retrieval of atmospheric states, the enhanced temporal resolution afforded by hyperspectral instruments enables the detailed monitoring of atmospheric profiles.

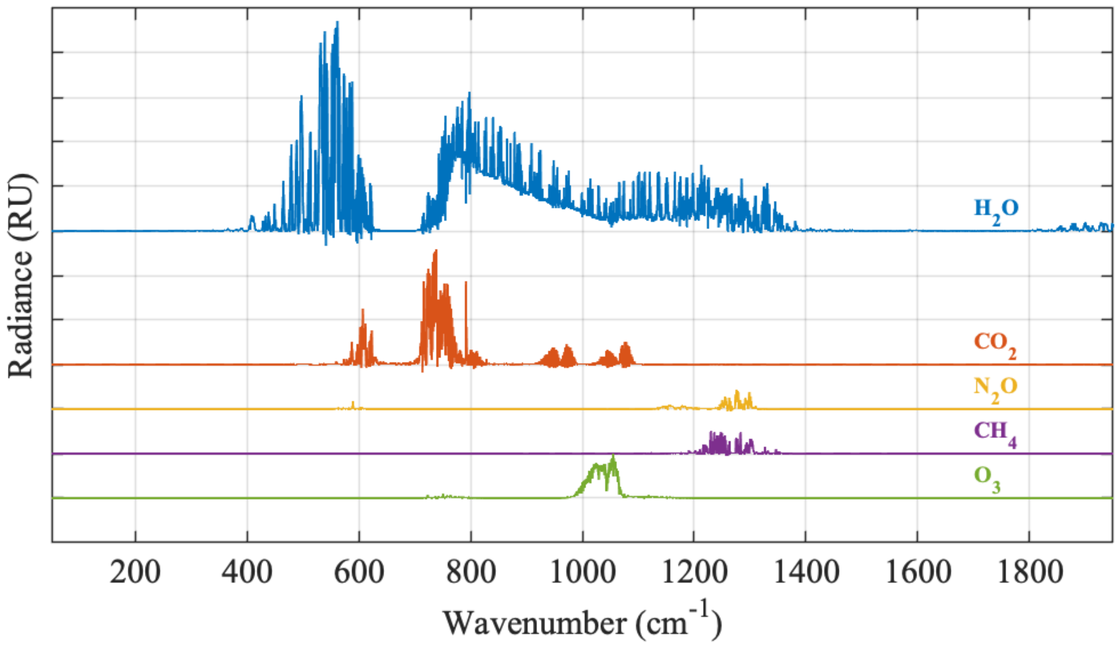

Figure 1.2 The spectral signatures of different atmospheric components in the downwelling longwave radiance (DLR) at the Earth's surface simulated by the Line-By-Line Radiative Transfer Model. The background profile is the standard mid-latitude summer (MLS) profile. The spectral resolution presented is 0.5 cm^{-1}. This figure illustrates the difference in DLR when employing original MLS concentrations compared to using half of those concentrations. RU stands for Radiance Unit, where 1 RU equals to 1 $mW/m^2/cm^{-1}/sr$. Each bin represents 10 RU.

One of the most important factors in Earth's observational science is the reliability of the data obtained. A notable illustration is the Keeling Curve (Keeling et al., 1976), which represents the time series of atmospheric carbon dioxide (CO_2) observed by nondispersive infrared analyzers at the Mauna Loa Observatory since 1958. It provides incontrovertible evidence of the escalating levels of atmospheric CO2. Thus, to rigorously evaluate the application of hyperspectral radiative measurements, it is crucial to validate the radiometric performance of these instruments, including assessing radiometric accuracy, the signal-to-noise ratio, and stability. Various methods have been developed to assess the radiometric performance of hyperspectral instruments, including various calibration tests and radiative closure tests (Delamere, et al., 2010; Knuteson et al., 2004b; Turner et al., 2004).

1.3.1 Hyperspectral infrared radiometer: AERI

The Atmospheric Emitted Radiance Interferometer (AERI) is a pivotal hyperspectral radiative radiometer discussed in this thesis. AERI captures DLR from 520 to 3020 cm^{-1} with a high spectral resolution of 0.5 cm^{-1} and a temporal resolution of approximately 20 seconds (Knuteson et al., 2004a, 2004b). As an SI-traceable instrument, AERI upholds absolute radiometric accuracy, rendering it suitable for sustained radiative observations.

AERI has proven crucial for the detection and attribution of climate change. Feldman et al. (2015) and Feldman et al. (2018) employed long-term AERI observations to ascertain the radiative forcing of surface CO_2 and CH_4 at specific sites. Gero and Turner (2011) determined DLR trends across various seasons for different sky conditions, leveraging a neural network approach developed in Turner and Gero (2011), at the Southern Great Plains (SGP) site based on a 14-year data series.

Retrieval algorithms have been developed for AERI measurements, both individually and in synergy with other passive or active instruments, to acquire temperature, water vapor, and cloud information (Feltz et al., 1998, 2003; Turner & Blumberg, 2018; Turner et al., 2000). AERI's measurements are most sensitive to the near-surface atmospheric profiles influenced by its location, offering invaluable insights into the monitoring of boundary layer thermodynamics.

1.3.2 Hyperspectral microwave radiometer: HiSRAMS

While energy in the microwave spectral range contributes minimally to Earth's energy balance due to its relatively low intensity, the capacity of microwave radiometers to penetrate clouds allows for the retrieval of crucial atmospheric states in all weather conditions. This ability enhances their interaction with both Earth's energy budget and hydrological cycle, making them a popular choice for remote sensing applications (Aires et al., 2015; Blackwell et al., 2010; Simmer, 1999; Smith et al., 2021).

In contrast to hyperspectral infrared radiometers, which offer a plenty of channels, most microwave radiometers are limited to only a few dozen channels, constraining the vertical resolution of the atmospheric states they retrieve. However, advancements in microwave technology, specifically fast Fourier transform (FFT) filters, have paved the way for the development of hyperspectral microwave radiometers. Through a collaborative effort involving Omnisys Instruments AB, the European Space Agency, the National Research Council of Canada, and McGill University, the High Spectral Resolution Airborne Microwave Sounder (HiSRAMS) was designed and developed, capturing hyperspectral microwave spectra across thousands of channels (Auriacombe et al., 2022; Bliankinshtein, Liu, et al., 2023).

HiSRAMS, an airborne dual-radiometer system, operates within both the oxygen and water vapor absorption bands. This instrument is capable of measuring spectra in single or dual polarization modes at various altitudes, with configurations for both zenith-pointing (upward-looking) and nadir-pointing (downward-looking) observations.

1.4 Research motivation and questions

Hyperspectral radiative measurements are instrumental in the detection and interpretation of climate change, offering insights into the Earth's energy budget and atmospheric state dynamics. These measurements serve as a pivotal link in unraveling the complex interplay between the Earth's energy budget and its atmospheric states. Recognizing the critical role of hyperspectral instruments in climate studies, this thesis aims to investigate their application in detecting and comprehending climate change. It seeks to address the following research questions:

1. Analogous to the "Keeling Curve" for CO_2 concentration, is it possible to establish a dependable "hyperspectral radiative Keeling Curve" using long-term, spectrally resolved DLR observations from AERIs at the SGP site? If so, can such a "Keeling Curve" serve as a means to detect and monitor climate change?
2. Evaluating the newly developed hyperspectral microwave radiometer, HiSRAMS: What is its radiative performance? How does it compare to other hyperspectral instruments like AERI in terms of radiometric accuracy?
3. With comparable number of channels, can hyperspectral microwave radiometers match the performance of hyperspectral infrared radiometers in retrieving temperature and water vapor profiles under clear-sky conditions? Furthermore, what is the potential of combining ground-based hyperspectral infrared with airborne hyperspectral microwave instruments for enhanced retrieval of these profiles?

The thesis is organized to systematically explore the stated research questions, and is divided into the following chapters:

1. Chapter 2 synthesizes a 23-year DLR record observed by two AERIs deployed at the SGP site. Using a weighted linear regression that accounts for the first auto-regression process, long-term DLR trends under various sky conditions are identified. Both interannual variability and measurement uncertainty are considered in the trend detection process and climate change signals are analyzed through the long-term trend in DLR.

2. Chapter 3 details three field campaigns we conducted in Ottawa, Canada, which gathered both hyperspectral infrared and microwave measurements alongside radiosonde observations under clear-sky conditions. Radiative closure tests are employed to assess the radiometric accuracy of AERI and HiSRAMS. A novel comparative approach involving the total column optical depth within the instrument's geometry and the radiative bias is introduced to evaluate the radiative performance between AERI and HiSRAMS.
3. Chapter 4 examines and compares the performance of clear-sky temperature and water vapor profile retrievals using both ground-based hyperspectral infrared and microwave measurements. A synergistic retrieval method, integrating both ground-based hyperspectral infrared and airborne hyperspectral microwave measurements, is developed. The performance of this synergistic retrieval is then compared against single-instrument retrieval results.
4. Chapter 5 summarizes the analytical findings aimed at addressing the previously raised research questions. Future work involving hyperspectral radiative measurements in detecting and understanding climate change is also proposed.

Chapter 2 TRENDS IN DOWNWELLING LONGWAVE RADIANCE OVER THE SOUTHERN GREAT PLAINS

Chapter 2, in full, is a reprint of the material as it appears in Liu, L., Huang, Y., Gyakum, J. R., Turner, D. D., & Gero, P. J. (2022). Trends in downwelling longwave radiance over the Southern Great Plains. *Journal of Geophysical Research: Atmospheres*, 127, e2021JD035949. https://doi. org/10.1029/2021JD035949. The thesis author was the primary investigator and author of this paper.

Trends in Downwelling Longwave Radiance over the Southern Great Plains

Lei Liu[1], Yi Huang[1], John R. Gyakum[1], David D. Turner[2], P. Jonathan Gero[3]

[1]Department of Atmospheric and Oceanic Sciences, McGill University, Montreal, QC, Canada.

[2]NOAA/OAR/Global Systems Laboratory, Boulder, CO, USA.

[3]Space Science and Engineering Center, University of Wisconsin-Madison, Madison, WI, USA.

Corresponding author: Lei Liu (lei.liu5@mail.mcgill.ca)

Key Points

- Long-term downwelling longwave radiance observations reveal distinctive trends across the infrared spectrum.
- Significant positive radiance trends in weak absorption bands indicate earlier detectability of climate change.
- Radiance trend uncertainty mainly results from natural variability, emphasizing the need to continue the measurements.

Abstract

Downwelling longwave radiation is an important part of the surface energy budget. Spectral trends in the downwelling longwave radiance (DLR) provide insight into the radiative drivers of climate change. In this research, we process and analyze a 23-year DLR record measured by the Atmospheric Emitted Radiance Interferometer (AERI) at the U.S. Department of Energy Atmospheric Radiation Program Southern Great Plains (SGP) site. Two AERIs were deployed at SGP with an overlapping observation period of about 10 years, which allows us to examine the consistency and accuracy of the measurements and to account for discrepancies between them due to errors associated with the instruments themselves. We then analyzed the all-sky radiance trends in DLR, which are associated with the surface warming trend at SGP during this same period and also the complex changes in meteorological conditions. For instance, the observed radiance in the CO_2 absorption band follows closely the near-surface air temperature variations. The significant positive radiance trends in weak absorption channels, such as in the wings of the CO_2 band and in the weak absorption channels in the H_2O vibration-rotational band, show earlier detectability of climate change. The magnitude of the radiance trend uncertainty in the DLR record mainly results from internal climate variability rather than from measurement error, which highlights the importance of continuing the DLR spectral measurements to unambiguously detect and attribute climate change.

2.1 Introduction

Longwave radiation is a key component of the atmospheric energy budget that drives climate change. At the top of the atmosphere (TOA), the outgoing longwave radiation (OLR), as well as its spectrally resolved radiance, is monitored by satellites with global coverage and long-term records (e.g., Liebmann & Smith, 1996; Stephens et al., 2012). This allows us to study changes in OLR and to test climate models (e.g., Brindley & Bantges, 2016; Harries et al., 2001; Huang & Ramaswamy, 2009; Huang, Ramaswamy, Huang, et al., 2007; Huang, Ramaswamy, & Soden, 2007; Palchetti et al., 2020; Pan et al., 2015; Wielicki et al., 2002). Even when there is continuous spatiotemporal coverage of OLR spectra, the compensating effects of greenhouse gas opacity and temperature warming make it difficult to detect climate change in satellite measurements (Huang, 2013a; Huang & Ramaswamy, 2009).

Downwelling longwave radiation emitted by the atmosphere is one key component in the surface energy budget (Stephens et al., 2012; Trenberth et al., 2009). Compared to the radiation budget at the TOA, the surface radiation budget is more uncertain and longwave radiation is a main contributor to the uncertainty (Trenberth et al., 2009; Wild et al., 2012). This is largely due to the paucity of global and long-term downwelling longwave radiance (DLR) observations. Despite the limits of spectrally resolved DLR records, it has been demonstrated that DLR measurements are useful for understanding the surface energy balance and testing climate models. For example, Lubin (1994) explained the super greenhouse effect by using observed DLR spectra over equatorial oceans; Feldman et al. (2015) used the DLR spectra to measure CO_2 radiative forcing at the Southern Great Plains (SGP) and the North Slope Alaska sites; Huang et al. (2019), Kapsch et al. (2016), Shupe and Intrieri (2004), Sokolowsky et al. (2020) and several others diagnosed the DLR variability in relation to sea ice, clouds and other climate changes in polar regions.

Climate change is driven by changes in energy balance. This leads us to an overarching question regarding the surface energy balance: can climate change be detected and understood by monitoring the DLR spectrum? One advantage of the DLR, compared to the OLR, is that the compensating effects mentioned earlier vanish. In the DLR, the greenhouse gas opacity and temperature warming effects reinforce each other to increase DLR. This makes DLR a potentially advantageous observation for monitoring climate change (Huang, 2013a). The signals from different meteorological variables such as temperature, greenhouse gases, and clouds imprint different spectral signatures. This allows for a spectral fingerprinting of their changes (Huang, Leroy, & Anderson, 2010). At the SGP site, the fifth generation European Centre for Medium-Range Weather Forecasts atmospheric reanalysis dataset, ERA5 (Hersbach et al., 2020), shows that there has been a significant warming in surface air temperature with a magnitude of ~0.045 K/year between 1996 and 2018 (Figure 2.1). Can this warming be detected from the DLR spectral records at that site?

We have two primary objectives in this paper. First, we are interested in constructing a long-term monthly DLR spectral record based on 23 years of measurements by the Atmospheric Emitted Radiance Interferometers (AERIs) installed at the U.S. Department of Energy Atmospheric Radiation Measurement (ARM) SGP site. Two AERIs have been deployed at this site and have rendered 10 years of overlapping observations but with different sampling strategies (i.e., 3 min sky average every 8 min vs multiple 20-s sky average observations every 4 min). We will examine the accuracy and consistency of the measurements and assess them against synthetic spectra simulated from collocated atmospheric measurements using a benchmark radiation model. Second, we will analyze the combined long-term DLR spectral trends for the period of 1996-2018. We are interested in ascertaining if the radiance trends in the AERI bands dominated by near-surface emission are consistent with the warming temperature trend shown by ERA5 (Figure 2.1). This work will also test the veracity of the trends documented by Gero and Turner (2011) using the early years of the DLR record and analyze the contributions from different sky conditions.

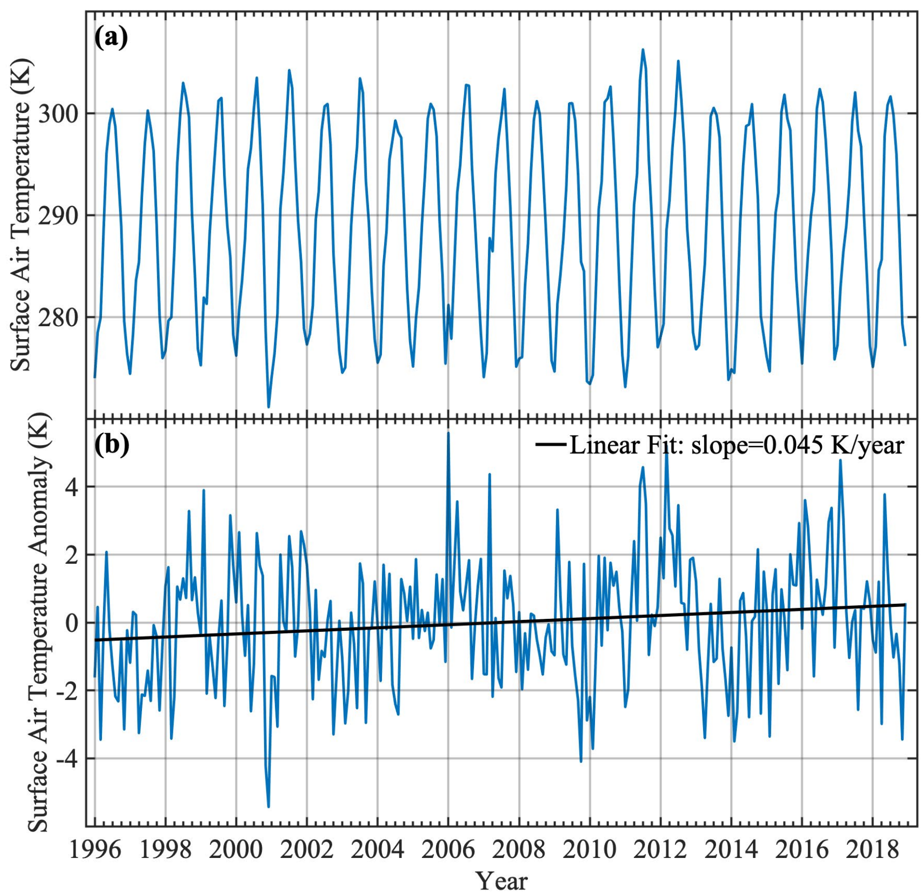

Figure 2.1: Warming trend at Southern Great Plains (SGP). Shown here is the ERA5 monthly mean 2 m air temperature time series at the SGP site (average of nine 0.25°x0.25° resolution grid boxes centered at: 97.5° W and 36.5° N) between 1996 and 2018. The anomaly is defined with respect to multi-year monthly mean of each calendar month.

2.2 Data and methods

2.2.1 AERI data processing

The AERI is a ground-based Fourier transform spectrometer that measures the DLR emitted from the atmosphere with an accuracy of 1% ambient radiance at high temporal and spectral resolution (Knuteson et al., 2004a, 2004b). The measurements cover the spectral range between 520 and 3020 cm^{-1} with a resolution of 0.5 cm^{-1}; however, we focus on the mid-infrared spectral range from 520 to 1800 cm^{-1} in this paper. Two high-emissivity blackbodies, a hot blackbody with a fixed temperature at 60°C and another blackbody at ambient temperature (Knuteson et al., 2004a), are used for radiometric calibration based on the method of Revercomb et al. (1988). The long-term average of all 23 annual mean DLR spectra and the standard deviation of monthly mean DLR spectra over the 23 years for different sky conditions at the SGP site are shown in Figure 2.2. We classify the scene into three different conditions: clear-sky, thin-cloud, and thick-cloud; the classification method will be explained in Section 2.2.2. The main difference in DLR between different sky conditions is primarily in the window portion of the spectrum (between 800 – 1200 cm^{-1}) shown in Figure 2.2a. The standard deviation of thick-cloud DLR is found to be the smallest among all the different sky conditions in the window band (Figure 2.2b), which indicates small variability of the radiating temperature of the thick clouds.

The two AERIs deployed at SGP have different observational periods and different sampling frequencies. AERI-01 operated from July 1995 to March 2014, while AERI-C1 has operated from February 2004 to the present. C1 is the designator of the Central Facility location of the SGP site. Historically E14 was an alternate designator for the same location. AERI-C1 was named AERI-E14 before 2011, for example, in Gero and Turner (2011). The two AERIs were deployed side-by-side (within 5 m of each other). Given their vertical field of view (FOV) of 2.6° full-angle, both instruments view the same portion of the sky; 86% of the FOVs of the two AERIs are overlapped at the altitude of 1 km. The overlapping observations make it possible to test the accuracy and consistency of the measurements. However, the two instruments differ with respect to their sampling frequency. AERI-01 measures one DLR spectrum approximately every 8 min; its measurement cycle includes a 200-s sky-dwell period (Knuteson et al., 2004b) and the rest of the cycle is used for viewing the blackbodies for calibration. AERI-C1 uses a rapid mode with ~20-s sampling cycle (Turner et al., 2006). Such differences in the measurements necessitate appropriate procedures to homogenize the data from the two AERIs for inter-comparisons and trend analyses.

Figure 2.3 shows the flowchart illustrating the data processing adopted in this paper. First, rigorous quality control is performed on the data to retain reliable observations. During the long history of observations at the SGP site, many factors have caused errors including: contamination of the scene mirror, malfunction of the interferometer, and failure of the detector temperature sensor. We first discard all the erroneous data based on the AERI quality control reports from the ARM program (https://adc.arm.gov/discovery/#/results/instrument_class_code::aeri). In addition, similar to the quality control method described in Turner and Gero (2011), the hatch status and the sky view noise equivalent radiance tests are also implemented.

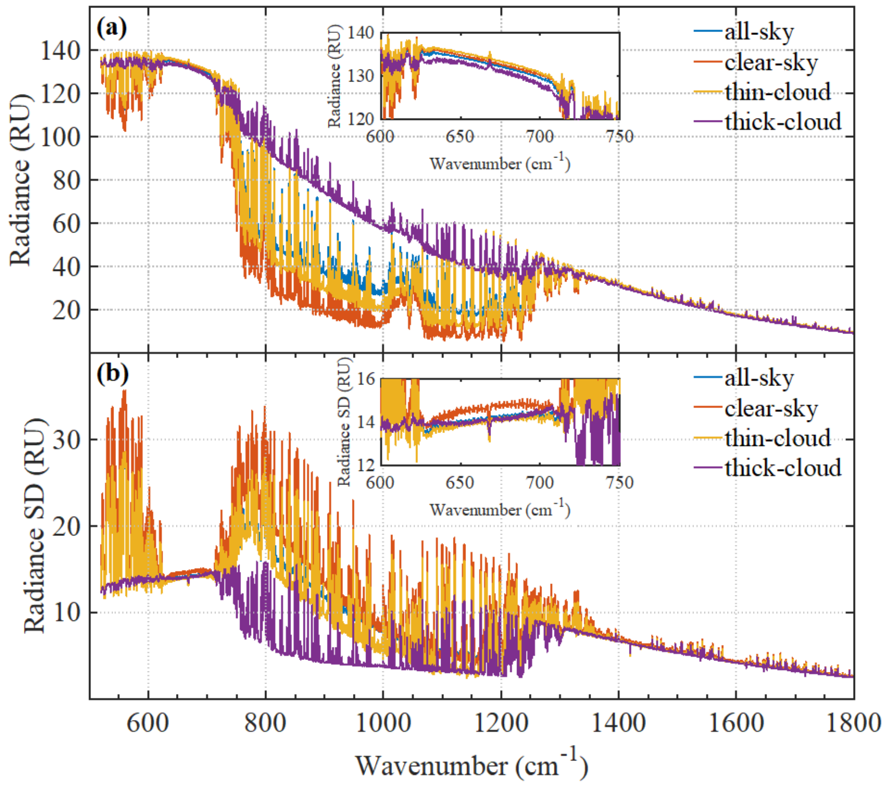

Figure 2.2: (a) Long-term average of all 23 annual mean AERI spectra for different sky conditions at Southern Great Plains (SGP). (b) Standard deviation of monthly mean AERI spectra for different sky conditions at SGP. (RU: Radiance Units; 1 RU = 1 mW/[m^2 sr cm^{-1}]) The insets in the two panels indicate the corresponding zoomed-in results in the CO_2 absorption band.

After the *Quality Control* step, we average the AERI-C1 spectra over 8 min intervals, to be consistent with the AERI-01 sampling period. Then, in the *Sky Classification* step, we apply a machine learning algorithm (detailed in Section 2.2.2 below) to classify the sky conditions as one of clear, thin cloud, or thick cloud overhead based on the 8 min mean radiance spectra. Next, we compute averages of all 8 min spectra of each sky type within each hour and then average the hourly spectra of the same hour of the day to obtain a monthly averaged diurnal cycle. It is verified that there is uniform diurnal sampling in each month; no data of the 24-hr diurnal cycle is missing. Next, the monthly mean spectra are obtained by averaging the monthly averaged diurnal cycle. Monthly means are discarded when the count of hourly spectra is below 400 (~ 55%).

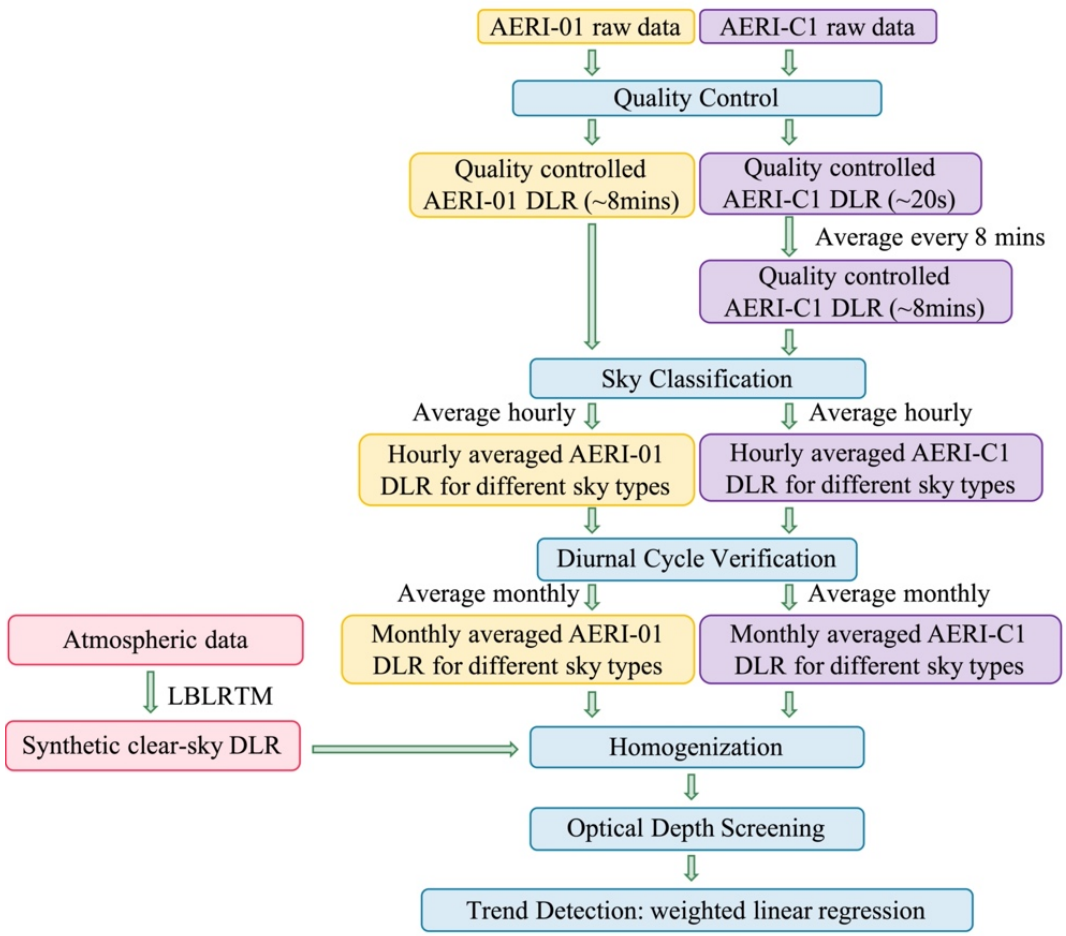

Figure 2.3: Data processing flowchart. Yellow and purple squares represent AERI-01 and AERI-C1 DLR data respectively. Blue squares represent important data processing steps. Pink squares represent radiative transfer model simulations. Details of processing steps are provided in the text.

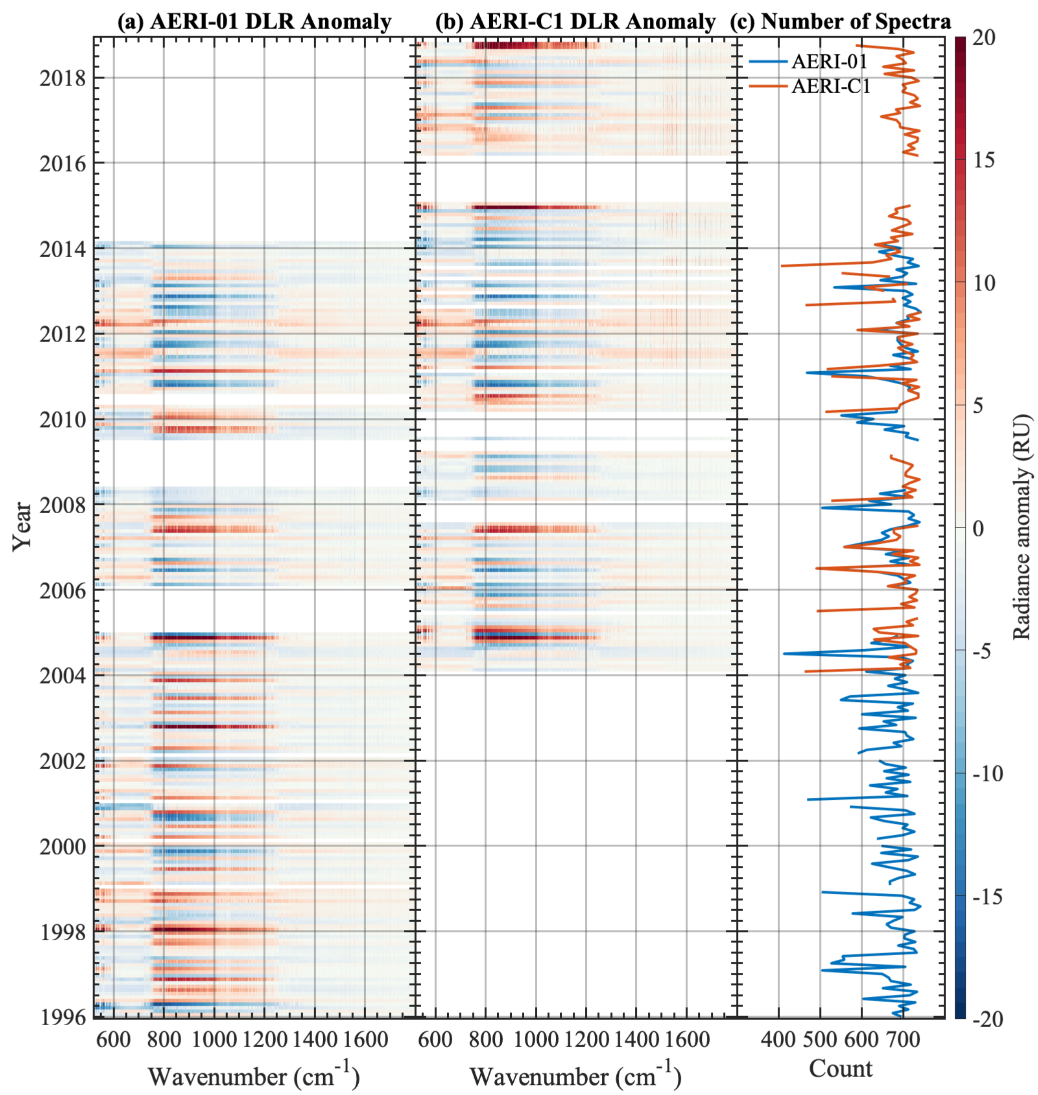

Figure 2.4: Monthly anomalies of AERI-observed downwelling longwave radiance spectra and hourly spectra count in each month.

Some channels in the center of the CO_2 absorption band (~ 667 cm^{-1}) and the water vapor absorption band (1300 – 1800 cm^{-1}) for which the near-surface atmosphere is so opaque that the channels are essentially uncalibrated are discarded in the *Optical Depth Screening* step. These strongly opaque channels are identified using the criterion that the gaseous optical depth for a 1 m layer of atmosphere at the surface is above 0.5. Finally, the monthly anomaly spectra are obtained by subtracting from each monthly mean spectra the long-term average of all 23 monthly mean spectra for that calendar month (which effectively removes the seasonal cycle). These monthly anomaly time series are illustrated in Figure 2.4, and are used in the following analyses and figures. The long-term trends in the DLR monthly mean spectra are analyzed based on the monthly anomaly spectra. Synthetic clear-sky DLR, computed using collocated radiosonde data and a radiative transfer model (described below), are used as a baseline to evaluate the measurements of the two AERIs during the overlapping period; details are provided in Section 2.5.

Both AERIs produced more than 600 hourly mean spectra per month nearly 90% of the time (Figure 2.4c). The strongest monthly DLR anomalies are seen in the window band (800 – 1200 cm^{-1}; Figure 2.4a and Figure 2.4b). The pattern of the DLR anomalies in the overlapping observational period is similar in both AERI-01 and AERI-C1.

2.2.2 Sky classification

Clouds strongly influence the DLR spectra, especially in the atmospheric window (800 – 1200 cm^{-1}). In order to identify the causes of the DLR trends, we separate the clear-sky spectra from the cloudy cases and examine their trends separately.

A sky-classification model is developed using a machine-learning method based upon the k-nearest neighbor (k-NN) algorithm (Cunningham & Delany, 2020). The 8 min AERI-01 and AERI-C1 spectra for the period between 1 March 2011 and 31 July 2012 are used to train the k-NN model. We use the same inputs and truth data from Raman Lidar as in Turner and Gero (2011). The k-NN classification achieves an accuracy of 94.8%. This algorithm determines the sky to be *clear* or *cloudy*, while the cloudy sky is then further classified to be *thin-cloud* when 70 min averaged 985 cm^{-1} brightness temperature is lower than 250K; otherwise, it is classified to be *thick-cloud*. We also tried a classical backpropagation gradient-descent classification algorithm as used by Turner and Gero (2011), which achieves an accuracy of 90%. The resulting trends are not sensitive to the classification method chosen. The results presented below are based on the k-NN algorithm.

Based on the classification of *thin-cloud* and *thick-cloud*, the *thick-cloud* emitting temperature range is smaller than that for *thin-cloud*, primarily because *thick-clouds* are opaque clouds relatively close to the surface while *thin-cloud* may be either partially cloudy scenes or clouds higher in the troposphere. This is why the *thick-cloud* classification has the smallest standard deviation of DLR among the three different sky conditions.

2.2.3 Homogenization

During the overlapping observational period, discrepancies larger than the documented AERI absolute calibration uncertainty (Knuteson et al., 2004a) were observed between the monthly mean spectra observed by AERI-01 and AERI-C1. Large radiance discrepancies occur, especially in the window band, and are found to mainly come from clear-sky scenes (see Figure 2.14 and discussions in Section 2.6). This suggests that the discrepancies likely result from calibration (Rowe, Neshyba, Cox, & Walden, 2011; Rowe, Neshyba, & Walden, 2011) and other undetected errors (e.g., something in the FOV of one instrument but not the other). In order to avoid discarding meaningful data in the trend analysis, we simulate the clear-sky DLR spectra using a radiation model together with collocated atmospheric measurements and use these synthetic spectra as a reference to assign proper weights in combining the data of AERI-01 and AERI-C1, based on the findings of previous radiance closure studies (e.g., Turner et al., 2004) that demonstrated high accuracy in such synthetic spectra.

The radiation model used here is the Line-by-Line Radiative Transfer Model (LBLRTM v12.9; Clough et al., 2005). To compute the clear-sky DLR spectra at SGP, we use the temperature and water vapor profiles from the ARM Balloon-Borne Sounding System (https://www.arm.gov/capabilities/instruments/sonde). The water vapor mixing ratio profiles derived from radiosondes are scaled with a height-independent factor to match the precipitable water vapor (PWV) retrieved by the microwave radiometer at the SGP site. This approach has been used to compensate for the dry-bias issue found in the radiosonde water vapor data (Holdridge, 2020; Revercomb et al., 2003; Turner et al., 2003; Wang et al., 2002). CO_2 and CH_4 concentration profiles are obtained from the CarbonTracker website (http://carbontracker.noaa.gov, Jacobson et al., 2020; Peters et al., 2007). O_3 concentration profiles are adjusted from NASA's Modern-Era Retrospective analysis for Research and Applications, Version 2 (MERRA-2, Gelaro et al., 2017) ozone product to get a better radiative closure with AERI-observed DLR (see more details in Section 2.6). We use a 200-level input profile for the LBLRTM simulations. The first and second levels are at 0 and 10 m above ground level respectively. The depth of each subsequent layer is increased by 2% relative to the one below.

As radiosonde observations of near-surface layers are essential to the DLR spectra, the AERI data are selected to match the radiosonde launch time. We keep the spectra whose observation time is within 10 min of the radiosonde launch time. For each month, about 70 clear-sky DLR spectra are simulated on average. The absolute values of the radiance biases (R_{bias}) are determined as the monthly mean radiance differences between the synthetic and observed DLR spectra.

During the overlapping observational period, the monthly mean AERI-01 and AERI-C1 DLR spectra are combined according to Equation 2.1 and Equation 2.2 using the ratio r, which represents the proximity of the AERI's observed DLR spectra to the synthetic DLR spectra. r is a function of wavenumber. The 5th, 50th and 95th percentiles of the ratio r across all AERI channels over the 23-year period are 0.55, 2.06, and 12.84 respectively. The weighted radiance used in the trend analysis is given by Equation 2.2, where $R_{AERI-01}$ and $R_{AERI-C1}$ represent the observed AERI-01 and AERI-C1 monthly mean DLR respectively.

$$r = \frac{R_{bias(AERI-01\ -LBLRTM)}}{R_{bias(AERI-C1\ -LBLRTM)}} \tag{2.1}$$

$$R = R_{AERI-01} \times \frac{1}{1+r} + R_{AERI-C1} \times \frac{r}{1+r} \tag{2.2}$$

2.2.4 Trend detection

A weighted linear regression method is applied to determine if there are any trends in the observed DLR. We develop our weighted linear regression model based on the regression model developed by Tiao et al. (1990) and Weatherhead et al. (1998).

This model determines the radiance trend, $\widehat{\omega}$, in each AERI channel, as:

$$\widehat{\omega} = \frac{\sum_{t=1}^{T} W_t\left(t-\bar{t}\right){y_t}^{\star}}{\frac{1-\phi}{12}\sum_{t=1}^{T} W_t(t-\bar{t})^2} \tag{2.3}$$

In Equation 2.3, T represents the total number of months and $\bar{t}$ represents the mean value of t. ϕ is the autocorrelation in the noise of the time series considering a first-order autoregressive (AR1) process, and ${y_t}^{\star}$ represents the transformed radiance anomalies (see Figure 2.11) after removing the effect of the AR1 process (see details in Section 2.5). W_t represents the weights which are determined as the intra-month variability of the all-sky observed DLR, shown in Equation 2.4:

$$W_t = \frac{N_t}{{\sigma_t}^2} \tag{2.4}$$

where N_t and ${\sigma_t}^2$ represent the number and variance of hourly observations in each month. Large variability of DLR results in smaller weights. We use the same weights for all sky conditions.

Along with the magnitude of the trend it is also important to determine the associated uncertainty, $\sigma_{\widehat{\omega}}$, which is shown in Equation 2.5. In Equation 2.5, ${\sigma_N}^2$ and ${\sigma_e}^2$ represent the variance of the error due to internal variability in the time series and the variance of the measurement error respectively. Here, we mainly account for two sources of uncertainty. First, there is the uncertainty arising from internal climate variability. This is accounted for by the term in Equation 2.5 associated with σ_N and ϕ. Second, there is the uncertainty arising from instrumentation errors accounted for by the term in Equation 2.5 associated with σ_e. We use the radiance difference between clear-sky LBLRTM simulation and clear-sky AERI-observation as the measurement error. We assume that these two sources of uncertainty are independent of each other. The derivation of Equation 2.5 is given in Section 2.5.

$$\sigma_{\widehat{\omega}} = \frac{12\sqrt{\sum_{t=1}^{T} {W_t}^2 (t-\bar{t})^2}}{\sum_{t=1}^{T} W_t (t-\bar{t})^2} \sqrt{{\sigma_N}^2 \frac{1+\phi}{1-\phi} + {\sigma_e}^2} \tag{2.5}$$

The derived $\sigma_{\widehat{\omega}}$ in Equation 2.5 is referred to as the standard error of the trend magnitude. It is used to test whether the trends deviate significantly from 0 at the 95% significance level. A trend is considered to be significant at the 95% significance level if the trend magnitude is larger than $2\sigma_{\hat{\omega}}$. In following figures, the uncertainty envelope plotted in gray corresponds to the 95% confidence interval.

2.3 Results

2.3.1 All-sky radiance trends

The homogenized DLR records have been constructed, based on monthly averaged AERI-01 data from 1996 to 2013 and AERI-C1 data from 2004 to 2018. In total, we have 23 years of DLR data at SGP for analysis.

It can be inferred from the monthly anomalies shown in Figure 2.4 that the DLR trends depend on the analysis period as the anomalies do not show monotonic changes over this 23-year period. The AERI-01 data (Figure 2.4a) show more frequent negative anomalies after 2011 in the window band (800-1200 cm^{-1}), which is consistent with the negative trends reported in Gero and Turner (2011) for this instrument. However, including AERI-C1 data (Figure 2.4b) affords a longer DLR spectral record, and the latest several years are characterized by warm anomalies.

The long-term all-sky radiance trends during the 1996-2018 period are shown in Figure 2.5. The all-sky DLR trends have different features in different spectral regions. In the CO_2 absorption band centered around 667 cm^{-1}, the trends are generally positive (i.e., radiance is increasing over time) and are statistically significant in the band wings but not at the center. In the window band (800-1200 cm^{-1}), there are very few statistically significant trends. In the water vapor absorption band (1300-1800 cm^{-1}), similar to the CO_2 absorption band, the radiance trends are generally positive and statistically significant.

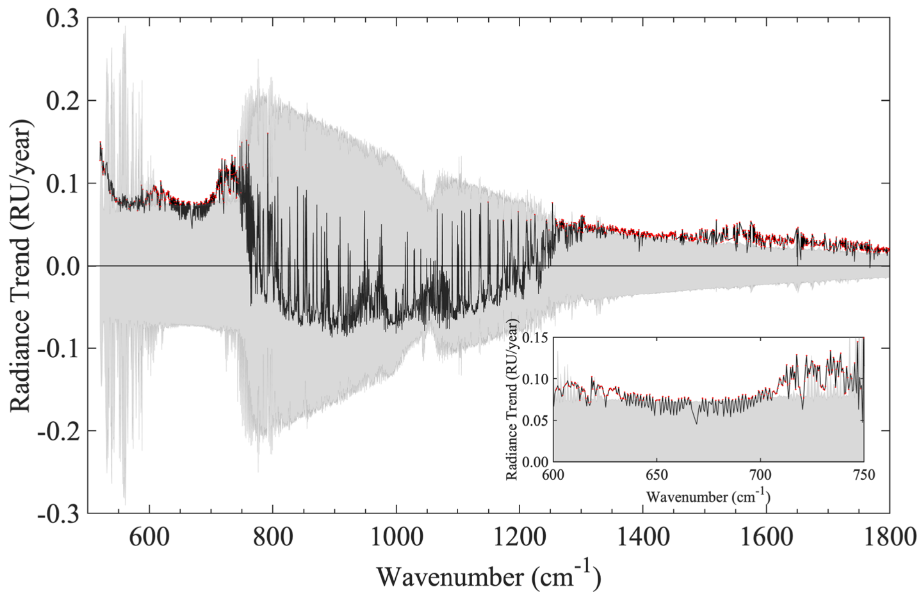

Figure 2.5: The all-sky radiance trends. The spectral elements indicated with red dots have trends that exceed the 95% significant test. The shading in the figure is the 95% confidence interval. The inset shows the zoomed-in results of CO_2 absorption band.

DLR in different AERI channels are controlled by different meteorological variables. To illustrate this point, Figure 2.6a shows the correlation coefficients between the deseasonalized and detrended monthly anomalies in the radiance (brightness temperature) spectra from the two AERIs and surface air temperature from ERA5. Note that AERI-01 and AERI-C1 have different observational periods, which result in different correlation coefficients especially in the window band. In the center of the CO_2 absorption band (667 cm^{-1}) and channels corresponding to strong H_2O absorption lines, the correlation coefficient is close to one, indicating that the variance in the radiance in these channels is primarily controlled by the surface air temperature. This is because the atmospheric absorption is strongly saturated in these channels and thus they are less sensitive to variations in the concentrations of the gases themselves and to temperatures of the atmospheric constituents farther removed from the surface. In comparison, in the wings of the

CO_2 band and the weaker H_2O absorption lines, the atmospheric absorption is not saturated so that variability in DLR is subject to the variation in the temperature and gas concentration throughout the vertical column. This means that the trends both in temperature and gas concentrations drive the radiance to increase, which explains the stronger and statistically more significant trend signals in these channels, as seen in Figure 2.5.

In Figure 2.6, the time series of the brightness temperature in four selected AERI channels: a CO_2 channel at 655.72 cm^{-1}, a window channel at 887.63 cm^{-1}, a O_3 channel at 1023.60 cm^{-1}, and a H_2O channel at 1447.89 cm^{-1} (Figure 2.6b-2.6e) are displayed. There is good consistency between the AERI-01 and AERI-C1 observed brightness temperature in all four channels. The all-sky brightness temperature at the CO_2 channel follows closely with the surface air temperature from ERA5 (Figure 2.6b). The near-surface warming of 0.045 K/year (Figure 2.1) is equivalent to 0.071 RU/year at this channel, which is close to the observed all-sky radiance trend of ~0.072 RU/year (averaged trend between 5 nearby channels). In the H_2O channel, the brightness temperature measured by the AERIs also follows the near surface air temperature (Figure 2.6e) but not as closely as the CO_2 channel (Figure 2.6b). In contrast, the brightness temperature anomalies in the window and O_3 channels have larger fluctuations than that in the CO_2 and H_2O channels and are evidently decoupled from the near surface air temperature (Figure 2.6c and Figure 2.6d).

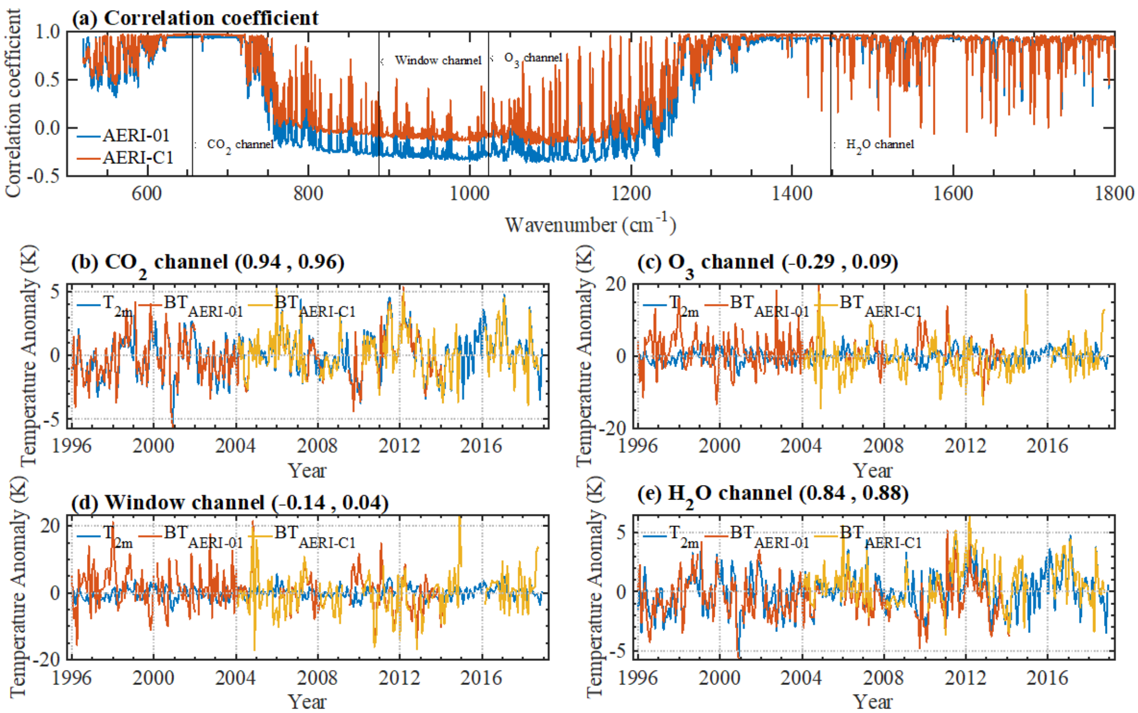

Figure 2.6: (a) The correlation coefficient between the AERI-observed brightness temperature spectra and near-surface air temperature from ERA5 at the SGP site over the 23-year period. (b-e) The time series of the deseasonalized brightness temperature and near surface air temperature in four AERI channels. In each title, the values in the parentheses are the correlation coefficients between near-surface air temperature from ERA5 and observed brightness temperature by AERI-01 and AERI-C1, respectively.

That the radiance trend is reinforced by both warming and opacity effects in the weak absorption channels indicates the benefits of using these AERI measurements in climate change detection. Assuming the trend magnitude and uncertainty determined from this 23-year record remain unchanged into future, the years to detect a significant trend, $n^{\star}$, at 90% significance level is:

$$n^{\star} \approx \frac{3.3\sigma_{\widehat{\omega}}}{|\widehat{\omega}|} \times 23\ years \tag{2.6}$$

where $\widehat{\omega}$ is the 23-year trend determined by Equation 2.3 and $\sigma_{\widehat{\omega}}$ is the trend uncertainty determined by Equation 2.5. The derivation of Equation 2.6 is given in Section 2.5.4. Although the trends are considered significant when $|\widehat{\omega}| > 2\sigma_{\widehat{\omega}}$, we require $|\widehat{\omega}| > 3.3\sigma_{\widehat{\omega}}$ when computing $n^{\star}$. As discussed in Section 2.7, this yields a more conservative estimation of $n^{\star}$ compared to the method of Leroy et al. (2008).

Based on this equation, approximately 30 years are needed to detect a significant trend in the 2 m air temperature from the ERA5 data shown in Figure 2.1 when $\widehat{\omega}$ and $\sigma_{\widehat{\omega}}$ are substituted with the 2 m air temperature trend magnitude and trend uncertainty, respectively. In comparison, Figure 2.7 shows earlier detectability of the radiance trends in weak absorption channels, such as in the wings of the CO_2 band and in the weak absorption channels in the H_2O vibration-rotational band. In Figure 2.7c, the earlier detectability of the radiance trends in the H_2O vibration-rotational band is noticeable in the wings of strong absorption lines (i.e., where the optical depth is relatively lower). We can conclude that it is advantageous to monitor the DLR in these weaker-absorption channels for climate change detection.

Trend detection in the radiance record is determined by comparing the trend signal to the uncertainties arising from different causes. Here, based on Equation 2.5, we account for uncertainties arising from climate internal variability (σ_N) and also instrumentation error (σ_e; Figure 2.5). The overall uncertainty is notably large in the window band for the all-sky condition (Figure 2.5), which impedes the detection of any significant radiance trends in this especially variable spectral region. Analysis of the respective parameters in Section 2.5 (see Figure 2.12) indicates that internal climate variability dominates instrumentation error when shaping the overall uncertainty envelope in Figure 2.5. It is also found that the influence of the autoregressive process does not strongly influence the trend uncertainty, as evident by the small value of ϕ, especially in the window band (Figure 2.12). We conclude that the trend uncertainty mainly arises from internal climate variability.

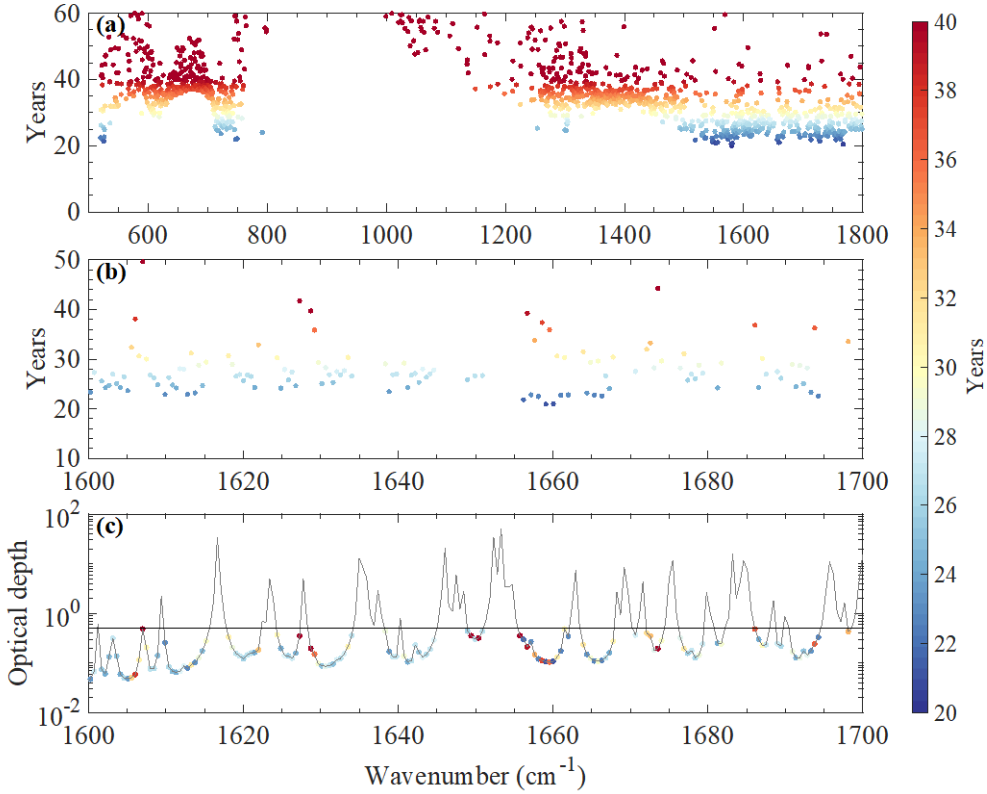

Figure 2.7: Trend detectability. (a) Time to detect (T2D) radiance trends at 90% significance level in different AERI channels; in comparison, the T2D for the 2 m temperature from the ERA5 reanalysis is about 30 years. (b) Zoomed-in figure of panel (a) in the water vapor absorption band. (c) The T2D (color-coded), in relation to atmospheric absorption strength, measured by the optical depth of a 1 m-thick atmospheric layer near the surface. The horizontal line marks optical depth of 0.5.

2.3.2 Trends in different cloud conditions

The results presented in the previous subsection demonstrate that the radiance trends in the window band are different from the greenhouse gas absorption bands; the window band is also prone to high levels of uncertainty due to the marked variability of the signal that ranges from small values in clear sky conditions to large values when opaque low-altitude clouds are overhead. Given the fact that clouds are a significant factor that influences this band (see Figure 2.2), we analyze the radiance trends under different cloud conditions in this subsection.

The fraction of time that each sky condition occurs in 1 month (referred to as "sky fraction") based on the hourly spectra are shown in Figure 2.8. First, there is a good agreement between AERI-01 and AERI-C1 in the sky fraction monthly time series, with correlation coefficients of 0.94, 0.89, and 0.94 for clear-sky, thin-cloud, and thick-cloud, respectively. The clear-sky fraction between June 1996 and May 2010 from our classification is around 42% which is comparable to what was found by Turner and Gero (2011).

The clear-sky fraction increases at a rate of 0.17 ± 0.09 % per year, while the thick-cloud fraction decreases at a rate of -0.18 ± 0.09 % per year. There is no significant trend for thin-cloud fraction. Understanding the atmospheric mechanisms that drive the trends in the sky fraction for different sky conditions are the subject of investigation in a future work.

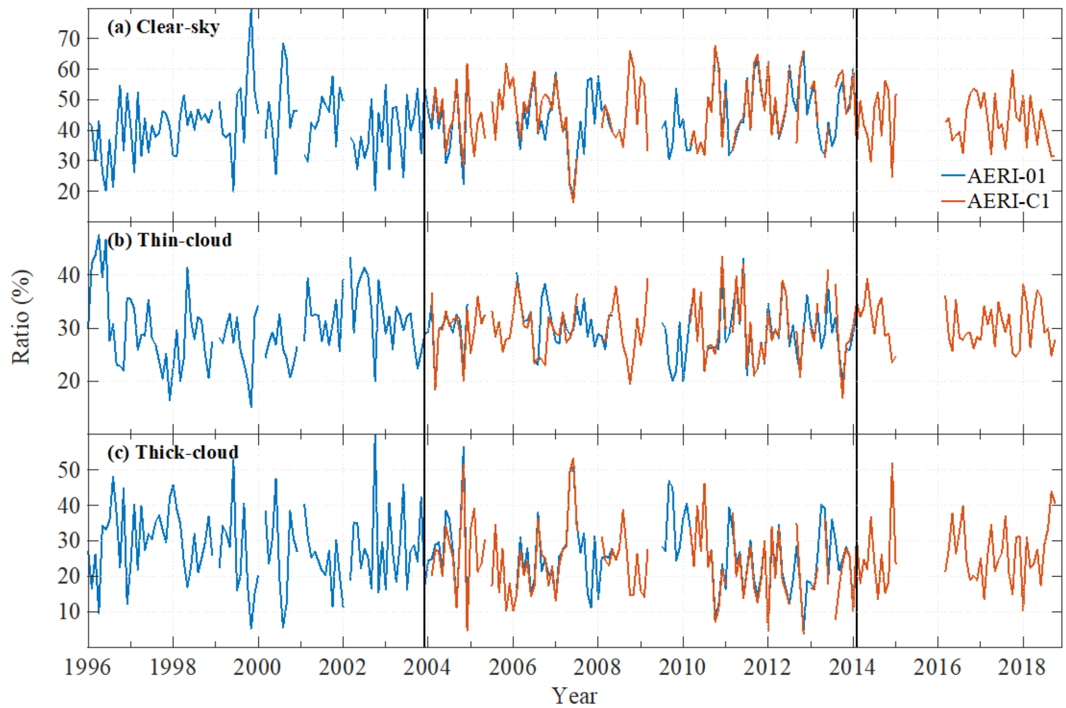

Figure 2.8: The monthly sky fractions of different sky conditions, categorized based on 8 min mean spectra at the Southern Great Plains site. The overlapping observational period is between the two vertical thick black lines.

Trends in AERI-observed DLR for different sky conditions based on the k-NN classifier are shown in Figure 2.9. In the window band, the clear-sky and thin-cloud trends are positive, while the thick-cloud trends are negative; however, none of those trends are statistically significant from zero because of the notably large trend uncertainty. The positive trend in the window band in the clear-sky data is likely due to increases in PWV, as hypothesized by Gero and Turner (2011). The positive trend in the thin-cloud classification suggests that either the clouds in these scenes are becoming more opaque, the clouds are becoming warmer (perhaps by moving lower in the troposphere), the PWV is increasing, or some combination of the three. The decrease in the thick-cloud trend in the window suggests that these thicker clouds are either becoming cooler or moving higher in the troposphere. In the spectral regions outside the window band, the trends for different sky conditions are generally positive and have the same features as the all-sky scenes.

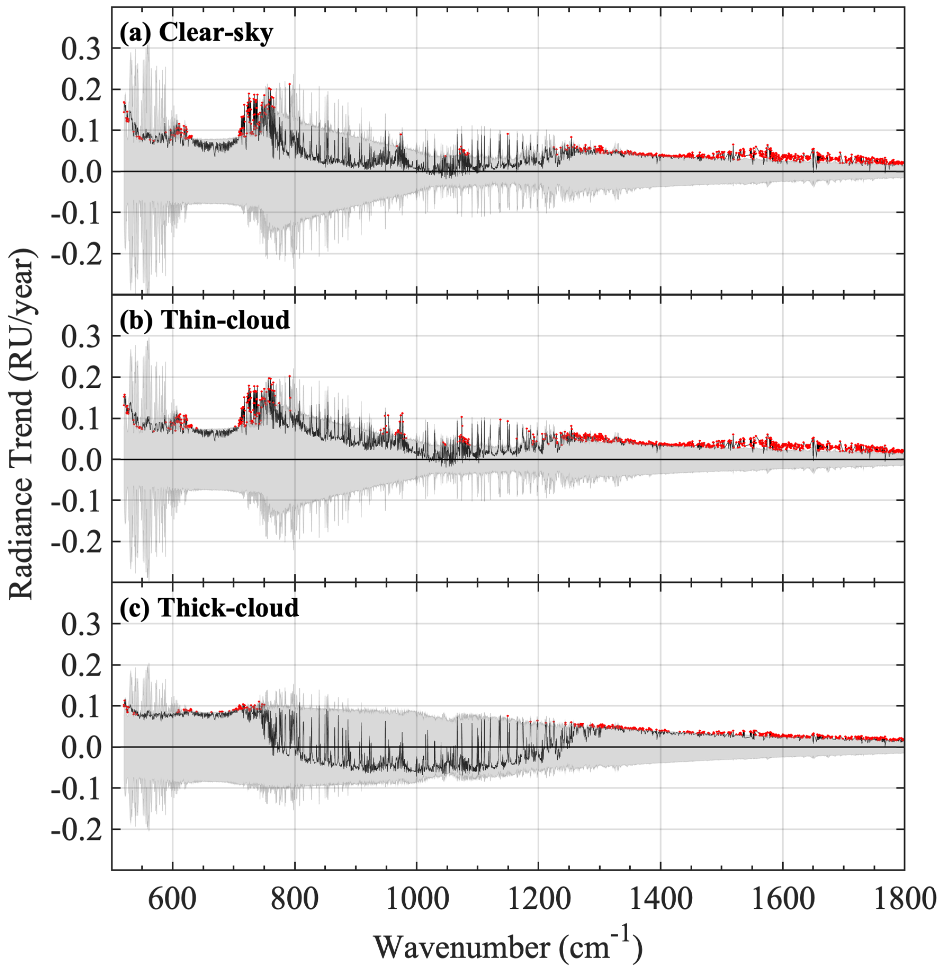

Figure 2.9: The trends in AERI-observed downwelling longwave radiance for different sky conditions at the Southern Great Plains site. The spectral elements marked with red dots indicate that the trends pass the 95% significance test. The shading in the figure is the 95% confidence interval.

The all-sky DLR trends are caused by changes in both sky fraction and the radiance of each sky condition. We use Equation 2.7 to separate the contributions from these factors, in which R_{all} represents the all-sky radiance, f_i and R_i represent the sky fraction and mean radiance for different sky conditions.

$$\frac{dR_{all}}{dt} = \sum \frac{df_i}{dt} R_i + \sum \frac{dR_i}{dt} f_i + residual \tag{2.7}$$

The results of the decomposed trends based on Equation 2.7 are shown in Figure 2.10. The small residual term (purple line in Figure 2.10a), which comes from nonlinear effects, suggests that the overall all-sky radiance trends can be well explained by Equation 2.7. In the window band, the overall radiance trends are a result of the compensation between the sky fraction change (orange line in Figure 2.10a) and the radiance change (yellow line in Figure 2.10a). In the opaque portions of the CO_2 absorption band (centered at 667 cm^{-1}) and H_2O absorption band (1300 – 1800 cm^{-1}), the overall radiance trends are caused by radiance change which is due almost entirely to the increases in the near-surface temperature because the atmosphere is already too opaque to reflect any gas concentration changes.

The overall radiance trends caused by sky fraction changes (orange line in Figure 2.10a) are a result of the compensation between changes in the clear-sky (blue line in Figure 2.10b) and the thick-cloud fraction (yellow line in Figure 2.10b) except in the opaque regions of the CO_2 absorption band (centered at 667 cm^{-1}) and H_2O absorption band (1300 – 1800 cm^{-1}). In the CO_2 absorption band and H_2O absorption band, the perfect compensation between positive trends caused by clear-sky and thin-cloud sky fraction changes and the negative trends caused by thick-cloud sky fraction changes results in almost no trends. In the window band, the negative trends are mainly caused by the thick-cloud fraction change.

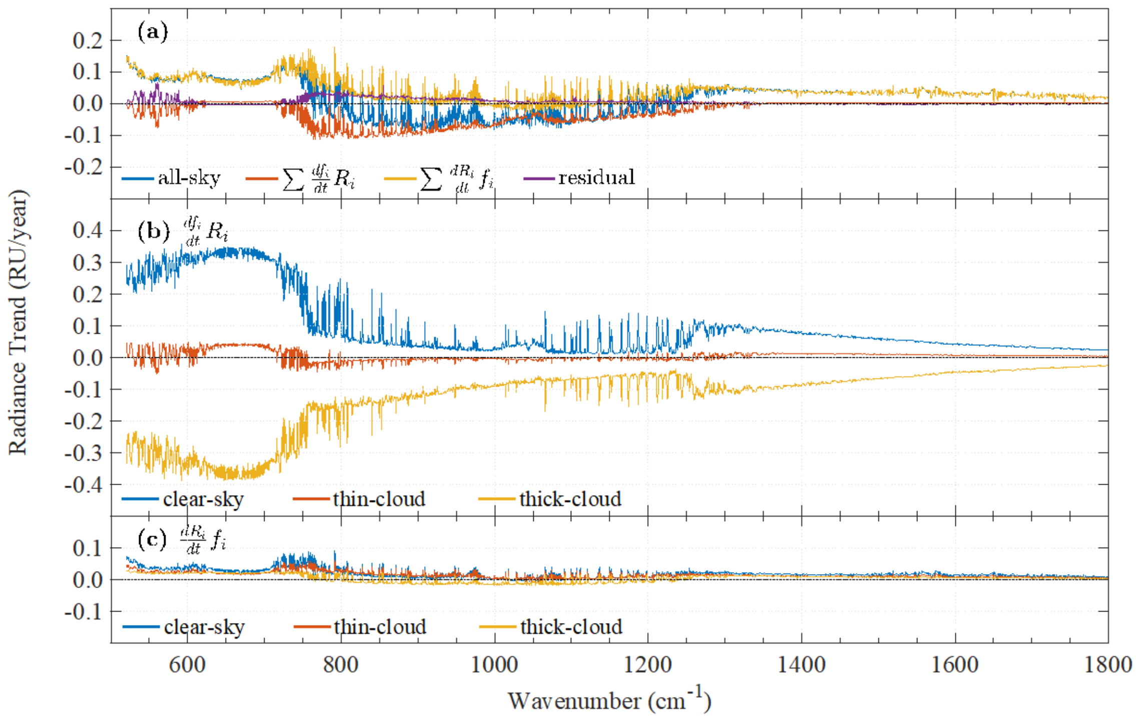

Figure 2.10: The all-sky downwelling longwave radiance (DLR) trends decomposed into the contributions from the sky fraction and radiance changes of different sky conditions. (a) The blue line represents the calculated all-sky DLR trends, which is the same as that from Figure 2.5. The orange and yellow lines represent the contributions from sky fraction change and radiance change determined using Equation 2.7, respectively. The purple line is the residual term from Equation 2.7; (b) The all-sky DLR trends caused by sky fraction change. The blue, orange, and yellow lines represent the contributions from clear-sky, thin-cloud, and thick-cloud fraction changes respectively; (c) The all-sky DLR trends caused by radiance change. The blue, orange, and yellow lines represent the contributions from clear-sky, thin-cloud, and thick-cloud radiance changes respectively.

In the window band (800 -1200 cm^{-1}), the overall radiance trends caused by radiance change (yellow line in Figure 2.10a) result from the compensation between positive clear-sky and thin-cloud radiance change trends and negative thick-cloud sky radiance change trends (Figure 2.10c). By contrast, in the CO_2 absorption band (centered at 667 cm^{-1}) and H_2O absorption band (1300 – 1800 cm^{-1}), the radiance changes for the three sky conditions all contribute similarly to the overall radiance trends caused by radiance change.

2.4 Discussion and conclusions

In this study, a long-term record of DLR at the SGP site has been constructed for analyzing the DLR trends, based on a weighted linear regression method that takes into account both natural climate variability and measurement error. Compared to previous studies, our analysis is based on a longer DLR record combined from the two AERIs at the SGP site, and makes use of synthetic DLR data in validating and differentiating the AERI measurements over their overlapping observational period. In addition, we quantitatively decompose the overall radiance trends due to the contributions from sky fraction change and the radiance change in each of these sky conditions.

The trends in DLR in different spectral ranges have different features. The trends are generally positive in the CO_2 and H_2O absorption bands, while no statistically significant trends are detected in the window band (Figure 2.5). We find that in the more opaque regions (the center of the CO_2 and H_2O absorption bands), the radiance is controlled by the near-surface air temperature (Figure 2.6) because of the strong atmospheric absorption. The sensitivity of DLR to near-surface air temperature indicates the potential of DLR to monitor climate change. In the wings of these absorption bands, both the near-surface atmospheric warming and the increase of the abundance of these trace gases contribute to the radiance trends (Feldman et al., 2015), which makes a climate trend signal more readily detectable, as hypothesized by Huang (2013a). In the window band, the radiance is decoupled from the near-surface air temperature (Figure 2.6) because of the impact of sky-fraction changes of different scenes (clear and cloudy-skies).

We find that the sky-fraction change and the radiance change led to compensating effects on the DLR trends. This compensation results in weakly (statistically insignificant) negative radiance trends in the window band (Figure 2.10). In contrast, the radiance trends are dominated by the radiance change in the CO_2 and H_2O absorption bands, which are similar in all three sky conditions.

The influences of both natural climate variability and measurement error are considered when determining the uncertainty of the trend magnitude (Equation 2.5, Figure 2.12). We find that for all sky conditions, the majority of the uncertainty comes from the natural variability. This underlines the necessity of continuous DLR measurements to ascertain the DLR trends, especially in the window band (Figure 2.5).

The two AERIs at the SGP site provide us with an excellent opportunity to test the accuracy and consistency of the instruments. The discrepancies between the two AERIs in the overlapping periods may have come from calibration error and other undetected instrumentation errors. In this study, we use synthetic data to differentiate and combine the two AERIs' observations. Further investigation is required to understand the origin of the discrepancies and therefore to assure the measurement accuracy.

This paper has focused on the detection, as opposed to attribution, of the DLR trends. In the clear-sky case, atmospheric temperature and radiative gas concentration changes (primarily water vapor) are likely the main contributors to the DLR changes. As for the cloudy-sky case, changes in both the atmospheric states and cloud properties may contribute to the DLR changes.

Future work is warranted to understand and quantitatively attribute the DLR trends disclosed in this paper to different meteorological variables.

2.5 Appendix A: Trend detection

We first summarize the linear trend model and trend estimation from Tiao et al. (1990) and Weatherhead et al. (1998) in Sections 2.5.1 and 2.5.2. We adopt the notation in their papers. Then we add the measurement error term to the trend detection in Section 2.5.3 following Tiao et al. (1990).

2.5.1 Basic linear trend modeling

In order to detect a linear trend, we first construct a simple model that describes the monthly mean radiance Y_t as:

$$Y_t = \mu + S_t + \omega X_t + N_t, t = 1, \cdots, T \tag{2.8}$$

where μ is a constant term, S_t represents the seasonal component, ω is the trend magnitude to be determined, $X_t = \frac{t}{12}$ represents time measured in the units of year, N_t represents the unexplained portion of the data (i.e., the noise), and T represents the length of the data set in months.

The seasonal component S_t is determined by computing a long-term average of each calendar month. This component is subsequently removed from the monthly mean.

$$y_t = Y_t - S_t = \mu + \omega X_t + N_t, t = 1, \cdots, T \tag{2.9}$$

The noise N_t is assumed to be autoregressive of the order of 1 (AR1):

$$N_t = \phi N_{t-1} + \epsilon_t \tag{2.10}$$

where ϵ_t is assumed to be random white noise with zero mean and common variance ${\sigma_\epsilon}^2$, $\epsilon_t \sim W(0, {\sigma_\epsilon}^2)$. The autocorrelations in the noise come from various natural factors. ϕ is determined as the autocorrelation coefficient of the AR1 process after removing from y_t a linear trend component obtained by regressing y_t to time using a simple weighted linear least squares method (i.e., neglecting the AR1). The all-sky ϕ is shown in Figure 2.12a.

The variance of the noise N_t can also be determined from the detrended y_t time series:

$$\begin{aligned} {\sigma_N}^2 &= Cov(N_t, N_t) = Cov(\phi N_{t-1} + \epsilon_t, \phi N_{t-1} + \epsilon_t) \\ &= \phi^2 Cov(N_{t-1}, N_{t-1}) + Cov(\epsilon_t, \epsilon_t) \\ &= \phi^2 {\sigma_N}^2 + {\sigma_\epsilon}^2 \end{aligned} \tag{2.11}$$

Thus,

$${\sigma_N}^2 = \frac{{\sigma_\epsilon}^2}{1 - \phi^2} \tag{2.12}$$

2.5.2 Trend estimation with weights

Given ϕ, to obtain the trend estimation, we consider a transformed model:

$$\begin{aligned} {y_t}^\star &= y_t - \phi y_{t-1} \\ &= \mu(1-\phi) + \omega(X_t - \phi X_{t-1}) + \epsilon_t \\ &= \mu(1-\phi) + \omega\left[\frac{t - \phi(t-1)}{12}\right] + \epsilon_t \\ &= \mu(1-\phi) + \frac{\omega\phi}{12} + \frac{\omega(1-\phi)t}{12} + \epsilon_t \\ &= \mu^\star + \omega t^\star + \epsilon_t \end{aligned} \tag{2.13}$$

where $\mu^\star = \mu(1-\phi) + \frac{\omega\phi}{12}$ and $t^\star = \frac{(1-\phi)t}{12}$. Thus, in the transformed model, the noise term N_t has been removed. The transformed DLR ${y_t}^\star$ is shown in Figure 2.11.

According to the weighted least squares estimation:

$$\widehat{\omega} = \frac{\sum_{t=1}^{T} W_t\left(t^\star - \overline{t^\star}\right){y_t}^\star}{\sum_{t=1}^{T} W_t\left(t^\star - \overline{t^\star}\right)^2} = \frac{\sum_{t=1}^{T} W_t\left(t - \bar{t}\right){y_t}^\star}{\frac{1-\phi}{12}\sum_{t=1}^{T} W_t\left(t - \bar{t}\right)^2} \tag{2.14}$$

where W_t represents the weights determined according to Equation 2.4, $\overline{y_t{}^\star} = \frac{\sum_{t=1}^{T} W_t y_t{}^\star}{\sum_{t=1}^{T} W_t}$, $\overline{t^\star} = \frac{\sum_{t=1}^{T} W_t t^\star}{\sum_{t=1}^{T} W_t}$, and $\bar{t} = \frac{\sum_{t=1}^{T} W_t t}{\sum_{t=1}^{T} W_t}$.

The variance of the estimated ω:

$$
\begin{aligned}
\sigma_{\widehat{\omega}}{}^2 = Var(\widehat{\omega}) &= Var\left[\frac{\sum_{t=1}^{T} W_t\big(t-\bar{t}\big)y_t{}^\star}{\frac{1-\phi}{12}\sum_{t=1}^{T} W_t(t-\bar{t})^2}\right] \\
&= \frac{Var\left[\sum_{t=1}^{T} W_t\big(t-\bar{t}\big)y_t{}^\star\right]}{(\frac{1-\phi}{12})^2\left[\sum_{t=1}^{T} W_t(t-\bar{t})^2\right]^2} \\
&= \frac{Var\left[\sum_{t=1}^{T} W_t\big(t-\bar{t}\big)\epsilon_t\right]}{(\frac{1-\phi}{12})^2\left[\sum_{t=1}^{T} W_t(t-\bar{t})^2\right]^2} \\
&= \frac{\sum_{t=1}^{T}[Var[W_t\big(t-\bar{t}\big)\epsilon_t]]}{(\frac{1-\phi}{12})^2\left[\sum_{t=1}^{T} W_t(t-\bar{t})^2\right]^2} \\
&= \frac{Var(\epsilon_t)\,\sum_{t=1}^{T} W_t{}^2(t-\bar{t})^2}{(\frac{1-\phi}{12})^2\left[\sum_{t=1}^{T} W_t(t-\bar{t})^2\right]^2} \\
&= \frac{\sigma_\epsilon{}^2\,\sum_{t=1}^{T} W_t{}^2(t-\bar{t})^2}{(\frac{1-\phi}{12})^2\left[\sum_{t=1}^{T} W_t(t-\bar{t})^2\right]^2}
\end{aligned}
\tag{2.15}
$$

$$
\sigma_{\widehat{\omega}} = \frac{\sigma_\epsilon}{\frac{1-\phi}{12}}\frac{\sqrt{\sum_{t=1}^{T} W_t{}^2(t-\bar{t})^2}}{\sum_{t=1}^{T} W_t(t-\bar{t})^2} = \sigma_N g(T,\phi,W) \tag{2.16}
$$

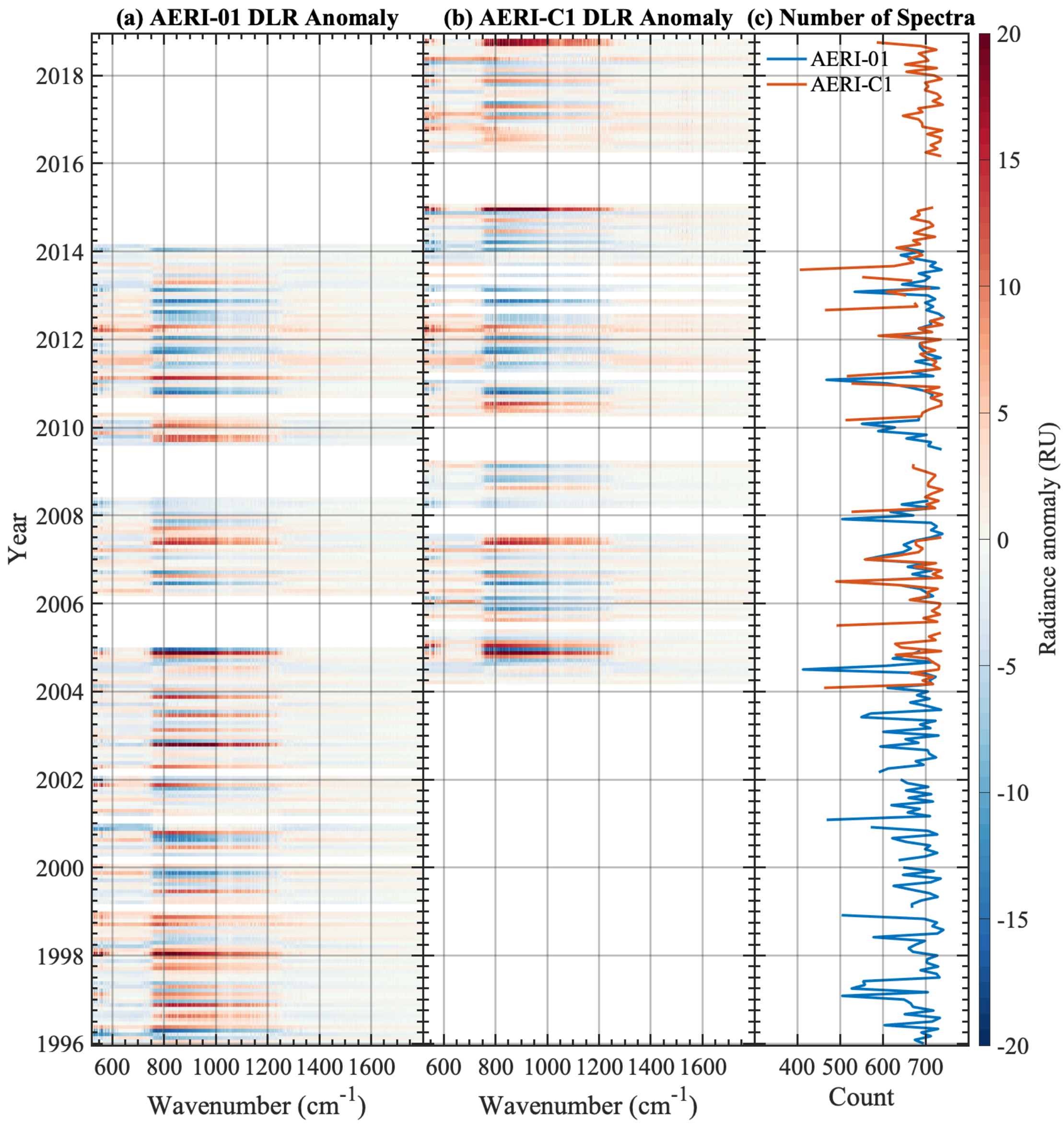

Figure 2.11: Transformed monthly anomaly of AERI-observed DLR spectra based on Equation 2.13 and hourly spectra count in each month.

In Equation 2.16, g is a function of T, ϕ, and W with the explicit expression shown in Equation 2.17.

$$g(T,\phi,W) = 12\sqrt{\frac{1+\phi}{1-\phi}}\frac{\sqrt{\sum_{t=1}^{T} {W_t}^2(t-\bar{t})^2}}{\sum_{t=1}^{T} W_t(t-\bar{t})^2} \tag{2.17}$$

Thus,

$$\sigma_{\widehat{\omega}} \quad = 12\,\sigma_N\sqrt{\frac{1+\phi}{1-\phi}}\frac{\sqrt{\sum_{t=1}^{T} {W_t}^2\left(t-\bar{t}\right)^2}}{\sum_{t=1}^{T} W_t\left(t-\bar{t}\right)^2} \tag{2.18}$$

From Equation 2.18, we conclude that the trend uncertainty is affected by the length of the available data, the natural variability in the data, the autocorrelation of the data, and the derived weights.

2.5.3 Effect of measurement error

When we consider the instrumentation errors e_t in the measurements, Equation 2.9 becomes:

$$y_t = \mu + \omega X_t + N_t + e_t, t = 1, \cdots, T \tag{2.19}$$

e_t is considered to be white noise with zero mean and common variance ${\sigma_e}^2$, $e_t \sim W(0, {\sigma_e}^2)$, and is considered independent of N_t because N_t originates from unobserved or unsuspected atmospheric factors, while e_t comes from the instrument itself.

In this case, the variance of noise comes from two parts:

$$\sigma^2 = {\sigma_N}^2 + {\sigma_e}^2 \tag{2.20}$$

Similar to the derivation in Equation 2.16, the variance of the estimated trend magnitude is:

$$
\begin{aligned}
\sigma_{\hat{\omega}}{}^2 &= \sigma_N{}^2 g^2(T,\phi,W) + \sigma_e{}^2 g^2(T,0,W) \\
&= \sigma_N{}^2 \frac{1+\phi}{1-\phi} \frac{144 \sum_{t=1}^{T} W_t{}^2 (t-\bar{t})^2}{\left[\sum_{t=1}^{T} W_t (t-\bar{t})^2\right]^2} + \sigma_e{}^2 \frac{144 \sum_{t=1}^{T} W_t{}^2 (t-\bar{t})^2}{\left[\sum_{t=1}^{T} W_t (t-\bar{t})^2\right]^2} \\
&= \left(\sigma_N{}^2 \frac{1+\phi}{1-\phi} + \sigma_e{}^2\right) \frac{144 \sum_{t=1}^{T} W_t{}^2 (t-\bar{t})^2}{\left[\sum_{t=1}^{T} W_t (t-\bar{t})^2\right]^2}
\end{aligned}
\tag{2.21}
$$

The uncertainty of the all-sky radiance trend magnitude caused by the natural variability and the measurement error are shown in Figure 2.12b.

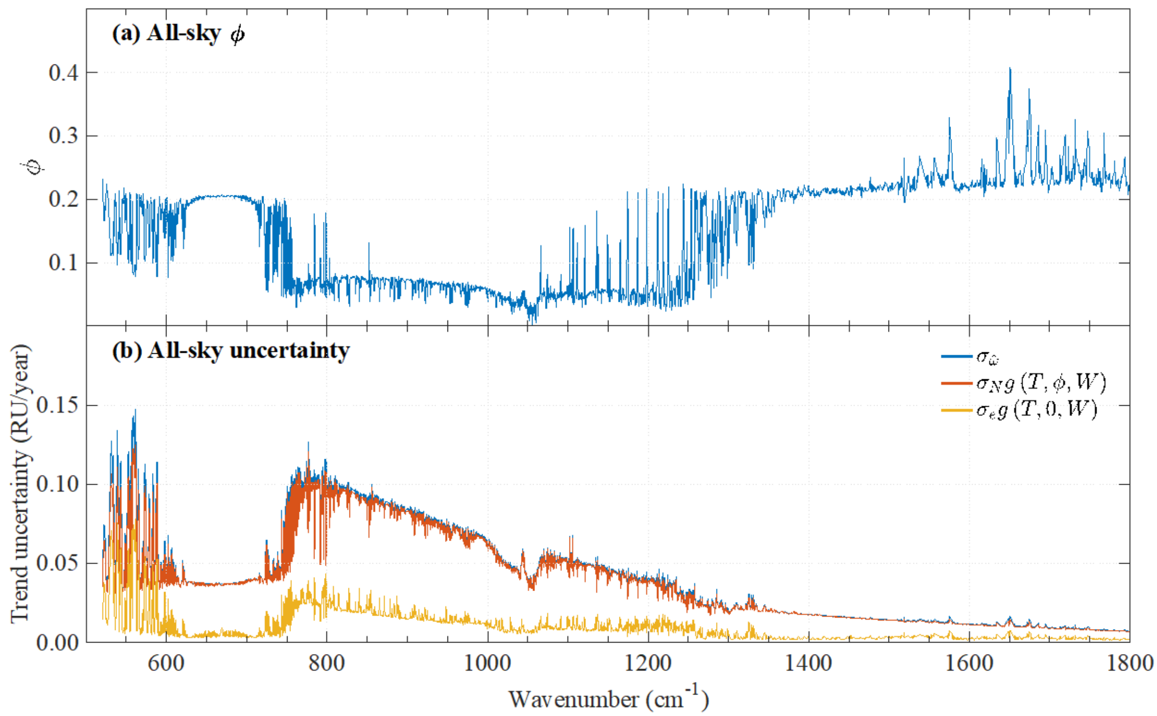

Figure 2.12: Parameters concerning the radiance trends. (a) The all-sky autocorrelation coefficient based on an AR1 process; (b) All-sky DLR trend uncertainty decomposition based on Equation 2.21. The blue line represents the total all-sky trend magnitude uncertainty, while the orange and yellow lines represent the all-sky trend magnitude uncertainty arising from natural climate variability and measurement error respectively.

2.5.4 Time to detect the trend

The trend detection ω is judged to be real or significantly different from zero at the 95% level if $|\widehat{\omega}| > 2\sigma_{\widehat{\omega}}$. $\widehat{\omega}$ is approximately normally distributed, so $z = \frac{\widehat{\omega}-\omega}{\sigma_{\widehat{\omega}}}$ follows a standard normal distribution.

$$Pr(|\widehat{\omega}| > 2\sigma_{\widehat{\omega}}) = Pr\left(z > 2 - \frac{\omega}{\sigma_{\widehat{\omega}}}\right) \tag{2.22}$$

To detect a real trend of specified magnitude $|\omega|$, with probability of 90%, requires that $2 - \frac{\omega}{\sigma_{\widehat{\omega}}} < -1.3 \Rightarrow \omega > 3.3\sigma_{\widehat{\omega}}$.

Thus, the number of years $n^{\star}$ of data required to detect the trend $\widehat{\omega}$ which is determined based on 23-year data, assuming that the trend and noise levels do not change relative to the 23-year period, is

$$n^{\star} \approx \frac{3.3\sigma_{\widehat{\omega}}}{|\widehat{\omega}|} \times 23\ years \tag{2.23}$$

We note that the T2D estimation is different from ascertaining whether the trend magnitude measured from data is significantly different from zero. Hence, although in some channels the trend magnitude is assessed to be “significant”, the estimated T2D may be longer than the record length (23 years). This is because when estimating T2D we recognize that the measured time series is one of the many possible realizations that, although governed by the same physical processes and thus of the same true trend, may not render the same trend magnitude in the data. This explains why the factor (3.3) used in the T2D estimation is different from that (2.0) used in the trend significance test.

2.6 Appendix B: Homogenization of the two AERI records

2.6.1 Comparison between the two AERIs

During the overlapping observation period, the all-sky monthly mean radiance difference between AERI-01 and AERI-C1 is shown in Figure 2.13. Since these two instruments have different sampling frequency, the AERI-C1 spectra are averaged to match the sampling of AERI-01 spectra before the comparison. From Figure 2.13a, there are noticeable discrepancies between the AERI-01 and AERI-C1 observations. Because of the different sampling frequency, the two AERIs have random errors of different amplitudes (Turner et al., 2006). However, we find that removing the random errors using the principal component analysis following Turner et al. (2006) has little impact on the discrepancies (not shown). We find that in more than 20% of the AERI channels in the spectral range from 700 to 1300 cm^{-1} and for more than 12% of the overlapping observational months, the radiance difference between two AERIs is larger than the documented absolute calibration uncertainty (Knuteson et al., 2004a).

For the AERI-C1 data stream, multiple instruments were used. All these transitions can be seen in Figure 2.13a as either subtle changes or obvious differences. First, the transition from AERI-04 to AERI-05 happened in September 2009, which caused subtle changes and is labeled by the green star in Figure 2.13a. These AERIs were among the several AERIs constructed by the University of Wisconsin-Madison for the ARM program. Next, in March 2010, the instrument changed from AERI-05 to AERI-06, which is labeled by the green triangle in Figure 2.13a. Then, the transition from AERI-06 to AERI-106 happened in March 2011, which caused more noticeable changes and is labeled by the green square in Figure 2.13a. At this point, the AERI technology was licensed to a commercial vendor, and their units are now characterized by a three-digit number. So AERI-106 is the 6th unit constructed by the vendor. AERI-106 operated until July 2013, when it was replaced with the AERI-108 which has operated at the SGP site since then. We find that the radiance differences between all of these "AERI-C1" instruments and the AERI-01 have unique spectral signatures.

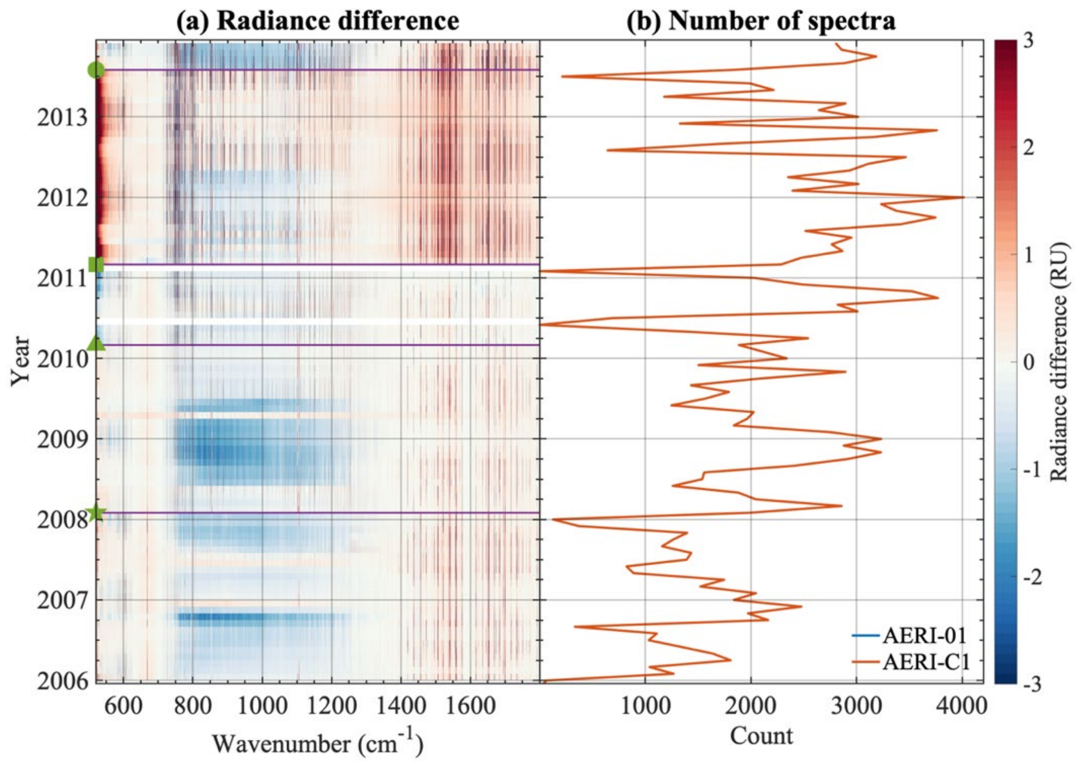

Figure 2.13: (a) The monthly mean DLR difference between AERI-C1 and AERI-01 (AERI-C1 – AERI-01). The green symbols indicate AERI-C1 instrument transitions; (b) Number of 8 min spectra for each month (the counts are identical after AERI-C1 spectra are resampled to match AERI-01).

When separating the measured spectra by different sky conditions, we find that the prominent difference between the two AERIs in the window band mainly comes from relatively clear sky conditions. Figure 2.14 shows the monthly mean radiance difference for different sky conditions in October 2006 as an example. Here the DLR at 985 cm^{-1} is used to classify the sky to be relatively clear or optically thin clouds (< 40 RU) or relatively cloudy (> 40 RU). We chose 40 RU based on the threshold that Turner and Gero (2011) used to classify cloudy sky to be thin or thick clouds scenes.

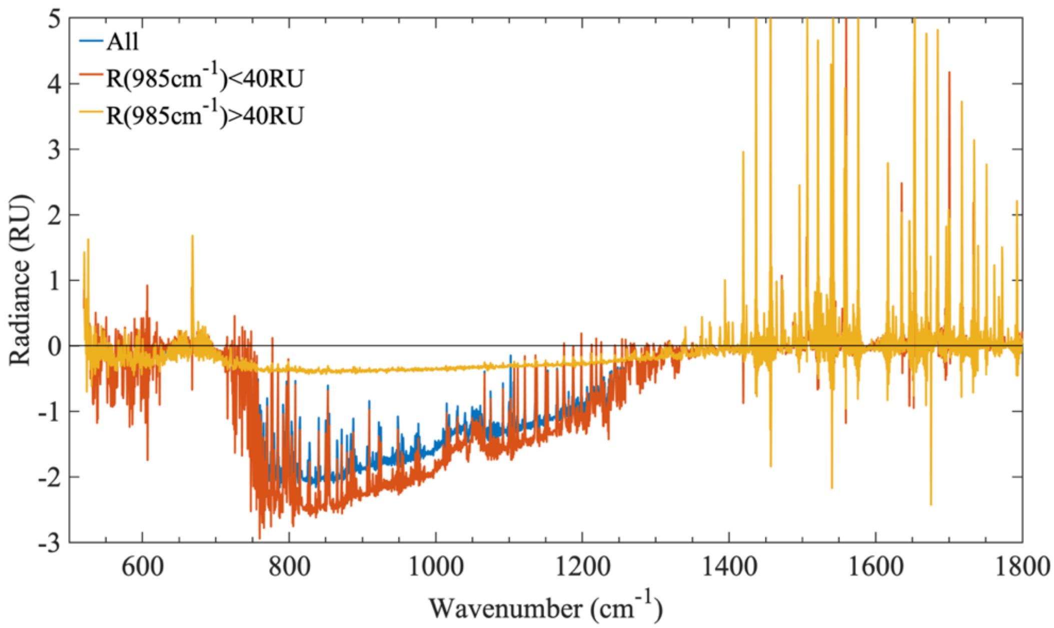

Figure 2.14: The monthly mean DLR difference between AERI-C1 and AERI-01 (AERI-C1 – AERI-01) for different sky conditions in October 2006. See text for details.

We examined various instrumental parameters recorded with AERI measurements, including calibration blackbody temperatures and instrument responsivity, but found that no instrumental parameter explains the radiance difference between the two AERIs. It is possible that an unknown obstruction was partially in the FOV of one of the AERIs (e.g., unit AERI-106), such as what was experienced with an early AERI at the SGP site (Knuteson et al., 1999).

2.6.2 Clear-sky LBLRTM simulations

Since the differences between two AERIs mainly come from relatively clear sky scenes, we use clear sky synthetic spectra simulated by the LBLRTM as a metric to distinguish their relative accuracies. Here we use the classical backpropagation gradient-descent classification algorithm mentioned in Subsection 2.2.2 to select clear-sky spectra. To ensure the case is clear, we set the algorithm threshold to be 0.8, which means the probability of the sky being clear is at least 0.8.

After matching all datasets, including radiosondes and gas concentrations at SGP mentioned in Section 2.2.3 to select atmospheric profiles, clear sky synthetic spectra are obtained during the overlapping observational period. For each month, about 70 DLR spectra are simulated on average. The LBLRTM simulation is validated based on the test in Feldman et al. (2015). We chose the same time slices selected in Feldman et al. (2015) to simulate the DLR spectrum and we can achieve similar radiative closures between observation and simulation.

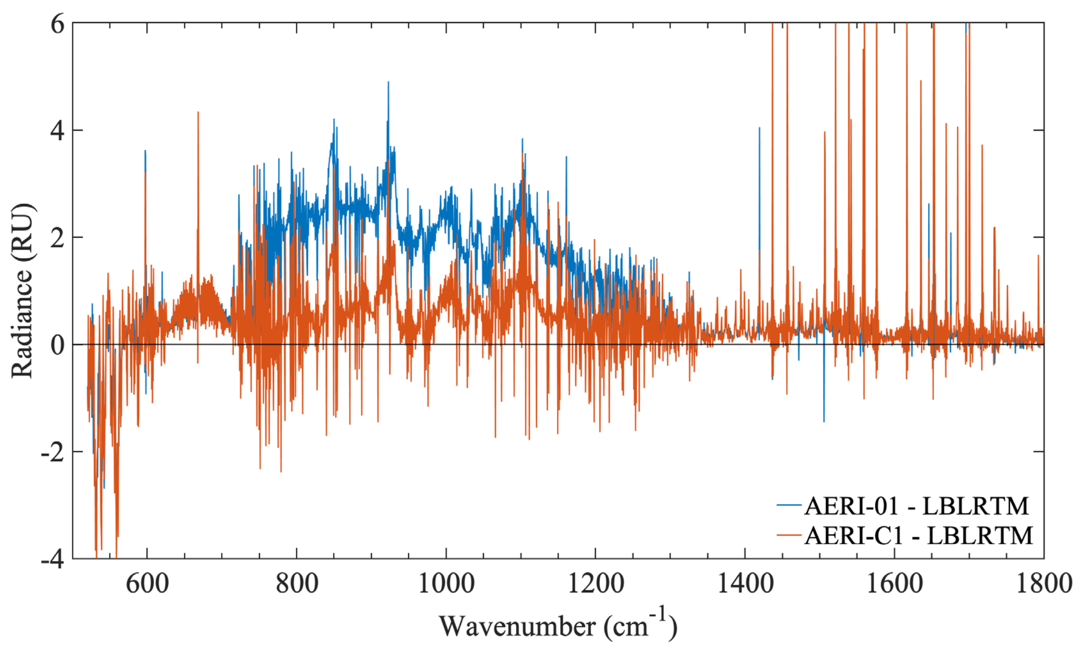

Figure 2.15: The clear-sky monthly mean DLR difference between AERI-observations and LBLRTM simulations in October 2006.

We originally used the ozone concentration profile from the Modern-Era Retrospective analysis for Research and Applications Version 2 (MERRA-2, Gelaro et al., 2017) in simulating the synthetic spectra. A relatively poorer radiance closure between AERI-observations and LBLRTM simulations was found in the ozone absorption band near 1040 cm^{-1} (not shown). By comparing the in-situ measurements at SGP (available only at limited times), we find that this is due to poor representation of the near-surface (and hence lower tropospheric) ozone concentration in the MERRA-2 dataset. To address this issue, we vertically scale the ozone profile uniformly to achieve an improved radiance closure in the ozone band as exemplified by Figure 2.15 (AERI-C1 line); however, this change to the ozone absorption region between 1040-1140 cm^{-1} has little impact on the all-sky radiance trend detected in Figure 2.5.

As demonstrated in Figure 2.15, we find that the AERI-C1 is generally in better agreement with LBLRTM simulations than AERI-01, especially in the window band. The radiance difference in each channel is used to weight the spectra of AERI-01 and AERI-C1, according to Equation 2.2, allowing us to develop an integrated record of monthly mean DLR spectra from the two instruments.

Figure 2.16 shows the comparison between LBLRTM simulated clear-sky DLR trends (blue dots) and AERI-observed clear-sky DLR trends (red dots) over the 23-year period. The clear-sky DLR trends using simulated clear-sky DLR values are similar to the clear-sky DLR trends using AERI-observations indicating the reliability of the simulated DLR long-term record.

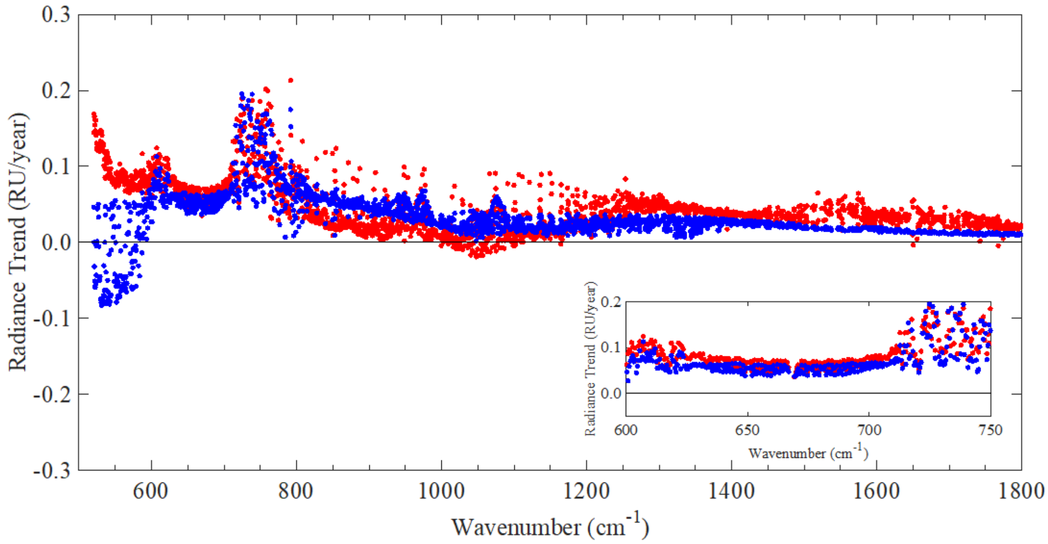

Figure 2.16: Comparison between LBLRTM simulated clear-sky DLR trends (blue dots) and AERI-observed clear-sky DLR trends (red dots) over the 23-year period. The inset shows the zoomed-in comparison in the CO_2 absorption band.

2.7 Appendix C: Comparison of the estimations of time to detect radiance trends

Leroy et al. (2008) proposed a formula (hereinafter referred to as the Leroy method) to calculate the minimum time to detect (T2D) a trend. T2D calculated using Equation 2.6 (hereinafter referred to as the Liu method) is longer than using the Leroy method.

Figure 2.17 shows the time to detect (T2D) radiance trends at 90% significance level in different AERI channels using the Liu method and the Leroy method respectively. The signal-to-noise ratio s in Equation 11 of Leroy et al. (2008) is set to be 3.3 in order to be consistent with our derivation in Section 2.5.4; the terms σ_{var} and σ_{mean} in this equation correspond to σ_N and σ_e in Equation 2.5 respectively.

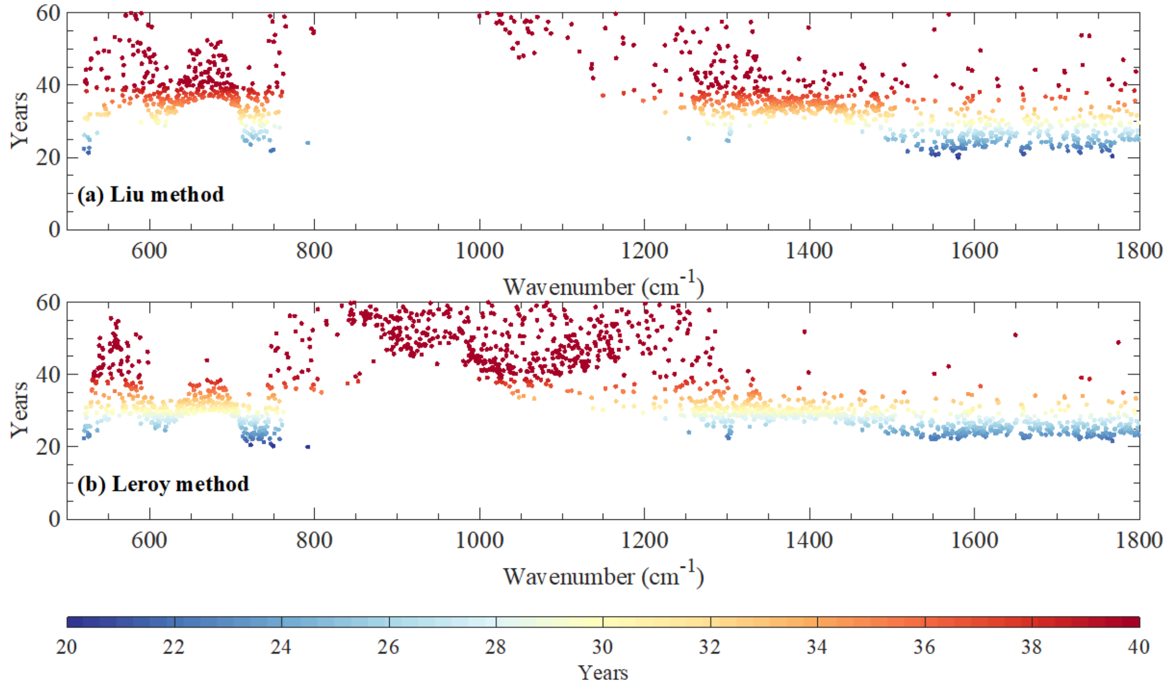

Figure 2.17: Trend detectability comparison between using (a) the Liu method and (b) the Leroy method.

The correlation coefficient between T2Ds obtained from the two methods is 0.93. T2D calculated using the Liu method is generally longer than that calculated using the Leroy method by 10 years when T2D is 40 years, and by 45 years when T2D is 100 years.

Chapter 3 RADIATIVE CLOSURE TESTS OF COLLOCATED HYPERSPECTRAL MICROWAVE AND INFRARED RADIOMETERS

Chapter 3, in full, is a reprint of the material as it appears in Liu, L., Bliankinshtein, N., Huang, Y., Gyakum, J. R., Gabriel, P. M., Xu, S., and Wolde, M. (2024). Radiative closure tests of collocated hyperspectral microwave and infrared radiometers, *Atmospheric Measurement Techniques*, 17, 2219-2233. https://doi.org/10.5194/amt-2023-215. The thesis author was the primary investigator and author of this paper.

Radiative closure tests of collocated hyperspectral microwave and infrared radiometers

Lei Liu[1], Natalia Bliankinshtein[2], Yi Huang[1], John R. Gyakum[1], Philip M. Gabriel[3], Shiqi Xu[2], Mengistu Wolde[2]

[1]Department of Atmospheric and Oceanic Sciences, McGill University, Montreal, Quebec, Canada.

[2]Flight Research Laboratory, National Research Council Canada, Ottawa, Ontario, Canada

[3]Horizon Science and Technology, Wolfville, Nova Scotia, Canada

Corresponding author: Lei Liu (lei.liu5@mail.mcgill.ca)

Abstract

Temperature and water vapor profiles are essential to climate change studies and weather forecasting. Hyperspectral instruments are of great value for retrieving temperature and water vapor profiles, enabling accurate monitoring of their changes. Successful retrievals of temperature and water vapor profiles require accuracy of hyperspectral radiometer measurements. In this study, the radiometric accuracy of an airborne hyperspectral microwave radiometer, the High Spectral Resolution Airborne Microwave Sounder (HiSRAMS), and a ground-based hyperspectral infrared radiometer, the Atmospheric Emitted Radiance Interferometer (AERI), is simultaneously assessed by performing radiative closure tests under clear-sky conditions in Ottawa, Canada. As an airborne instrument, HiSRAMS has two radiometers measuring radiance in the oxygen band (49.6-58.3 GHz) and water vapor band (175.9-184.6 GHz) for zenith-pointing and nadir-pointing observations. AERI provides ground-based, zenith-pointing radiance measurements between 520 and 1800 cm^{-1}. A systematic warm radiance bias is present in AERI observations in the window band. Upon removal of this bias, improved radiative closure was attained in the window band. The brightness temperature (BT) bias in nadir-pointing HiSRAMS observations is smaller than at the zenith. A novel but straightforward method is developed to diagnose the radiometric accuracy of the two instruments in comparison based on the relationship between radiometric bias and optical depth. Compared to AERI, HiSRAMS demonstrates similar radiometric accuracy for nadir-pointing measurements but exhibits relatively poor accuracy for zenith-pointing measurements, which requires further characterization. Future work on temperature and water vapor concentration retrievals using HiSRAMS and AERI is warranted.

3.1 Introduction

Accurate long-term measurements of the vertical distributions of temperature and water vapor are crucial for climate change analysis, climate model validation, and weather forecasting. Radiosondes provide accurate in situ temperature and water vapor profiles with high vertical resolution but are limited in spatial and temporal coverage. Remote sensing techniques have been developed to fill such data gaps (Aires et al., 2015; Blackwell et al., 2010; Delamere et al., 2010; Turner & Blumberg, 2018; Warwick et al., 2022; King et al., 1992; Han & Westwater, 1995; Westwater, 1997; Turner et al., 2000). Hyperspectral measurements, in which the vertical information of temperature and water vapor can be retrieved from different spectral channels (Smith et al., 2021), are valuable for sounding their vertical distributions (e.g., Divakarla et al., 2006; Turner & Blumberg, 2018). Spectral resolution (the number of channels within a certain spectral range) is pivotal in determining the information content in such retrievals (Rodgers, 2000).

Both hyperspectral infrared and microwave radiometers can be employed to retrieve temperature and water vapor concentration profiles. A distinct advantage of microwave radiometers in retrieving temperature and water vapor profiles is their ability to sound through clouds, allowing for all-sky retrievals. However, the existing microwave radiometers typically have no more than 100 spectral channels (Blackwell et al., 2010; Hilliard et al., 2013), which is an order of magnitude less than infrared hyperspectrometers (Aumann & Strow, 2001; Carminati et al., 2019; Knuteson et al., 2004a). Thanks to the advancement of digital polyphase fast Fourier transform (FFT) filter banks, hyperspectral microwave radiometers can now acquire a comparable number of spectral channels, which allows us to access and compare their temperature and water vapor profiling abilities as well as develop synergies between hyperspectral microwave and infrared radiometers. The High Spectral Resolution Airborne Microwave Sounder (HiSRAMS) is such a hyperspectral microwave radiometer, developed by Omnisys Instruments AB, National Research Council of Canada (NRC), and McGill University under the sponsorship of the European Space Agency (Auriacombe et al., 2022; Bliankinshtein, Liu, et al., 2023). As a prototype for possible future satellite missions, HiSRAMS' accuracy needs thorough assessment.

In this study, we focus on two hyperspectral radiometers: (1) HiSRAMS, operating in the microwave spectral range (49.6-58.3 GHz and 175.9-184.6 GHz for single-polarized observations), and (2) the Atmospheric Emitted Radiance Interferometer (AERI), operating in the infrared spectral range (520-3020 cm^{-1}). AERI is a well-tested instrument with good radiometric accuracy (Knuteson et al., 2004b), which provides a benchmark comparison for the radiometric accuracy of HiSRAMS.

HiSRAMS, a payload mounted on a wing of the NRC's Convair-580 research aircraft (Bliankinshtein et al., 2022), provides zenith-pointing (looking up) and nadir-pointing (looking down) observations or can be deployed on the ground for zenith-pointing observations. AERI is perpetually deployed on the ground for zenith-pointing observations (Knuteson et al., 2004a, 2004b). Both instruments have high spectral resolutions and mainly target the retrieval of temperature and water vapor profiles with the potential to retrieve other trace gases. When airborne, HiSRAMS can take measurements at different altitudes. Such multi-altitude measurements yield more constrains of the detailed and extensive temperature and water vapor retrievals. In comparison, AERI has been demonstrated to be capable of retrieving temperature and water vapor profiles at high vertical resolutions, especially in the boundary layer (Turner & Löhnert, 2014; Turner & Blumberg, 2018).

The radiometric accuracy of the hyperspectral measurements is vital for successful retrievals. For example, in the optimal estimation method (Rodgers, 2000), the ability of a hyperspectrometer to resolve the vertical distributions of temperature and water vapor can be measured by the degree of freedom for signals (DFS), which is dependent on the characterizations of errors in both the hyperspectral measurements and the meteorological variables. Radiative closure tests can help determine the bias in the radiometer measurements and provide clues to their origins (Barrientos-Velasco et al., 2022; Clough et al., 1994; Delamere et al., 2010; Turner, 2003). In this study, we focus on clear-sky radiative closure tests to avoid uncertainties due to the poor representation of clouds. Two primary objectives of this work include (1) collecting collocated AERI and HiSRAMS radiance measurements under clear-sky conditions and (2) performing radiative closure tests for both radiometers and comparing their radiometric accuracy.

3.2 Data and method

3.2.1 Datasets

Three clear-sky field campaigns (FC2021, FC2022, and FC2023) were carried out in Ottawa, Canada (latitude: 45.32° N, longitude: 75.66° W), to collect hyperspectral measurements and to perform radiative closure tests of the AERI stationed on the ground and the HiSRAMS mounted on the NRC's Convair-580 research aircraft (details listed in Table 3.1).

Table 3.1: Summary of the three field campaigns.

Field Campaign	Date	Radiosonde	HiSRAMS	AERI
FC2021	29 October 2021	14:21:57 - 15:59:32 UTC PWV: 0.69 cm	Ground-based measurements, pre-refurbishment, dual- and single-polarized (14:22:00 - 15:59:00 UTC)	Continuous ground-based measurements, every ~20 s
FC2022	9 December 2022	18:57:33 - 20:08:47 UTC PWV: 0.37 cm	Ground-based measurements, after-refurbishment, dual- and single-polarized (18:45:37 - 20:10:34 UTC)	
FC2023	11 February 2023	14:22:53-15:26:22 UTC PWV: 0.32 cm	Flight measurements at different altitudes, ground-based measurements before taking off (13:45:45 - 13:46:28 UTC) and after landing (16:35:24 UTC), single-polarized	

Radiosonde measurements were collected (one for each campaign), together with the HiSRAMS (Figure 3.1a, Figure 3.1b) and AERI measurements (Figure 3.1c). Ground-based zenith-pointing HiSRAMS measurements were archived in all three field campaigns. In the first two field campaigns, HiSRAMS collected longer ground-based records. In the final field campaign, HiSRAMS was mounted on the NRC's Convair-580 research aircraft to gather ground-based zenith-pointing measurements before take-off and after landing, including airborne measurements at different flight altitudes. In all three field campaigns, AERI provided continuous ground-based zenith-pointing measurements.

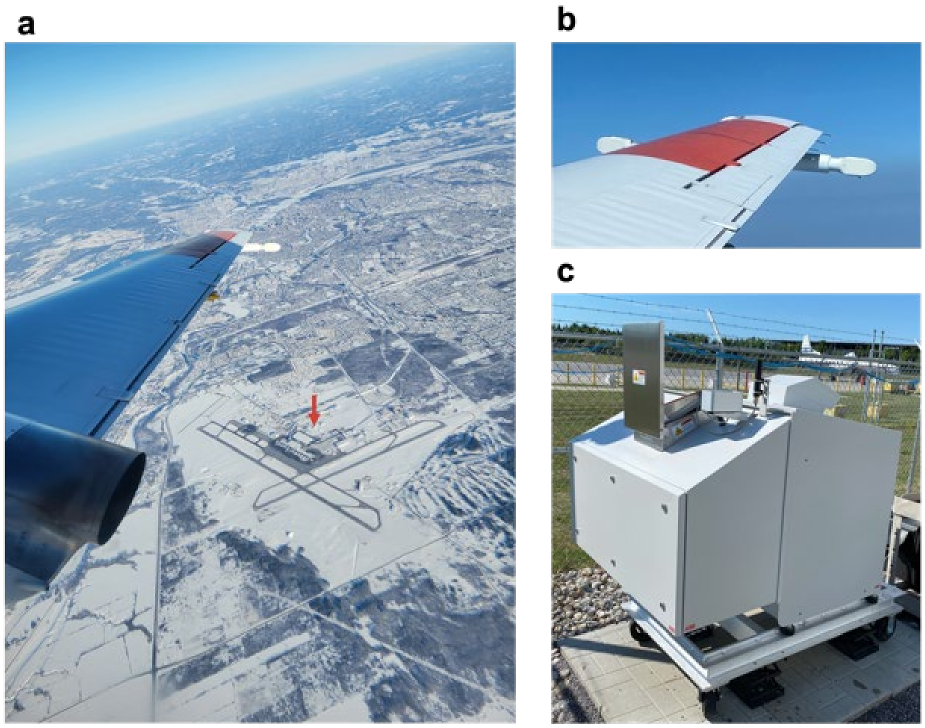

Figure 3.1: (a, b) HiSRAMS mounted on the wing tip of the NRC's Convair-580 research aircraft for zenith-pointing and nadir-pointing measurements during the flights. The arrow in panel (a) indicates the location of AERI. (c) AERI on the ground with the hatch open, taking zenith-pointing measurements.

3.2.1.1 Radiosonde temperature and water vapor profiles

The radiosonde used in this study was an iMet-4 from InterMet. We considered both repeatability and reproducibility errors in temperature and relative humidity to determine the total radiosonde uncertainty, following the procedure outlined in Blumberg et al. (2017).

Repeatability errors indicate random errors, measuring 0.2 K for temperature and 5% for relative humidity. Meanwhile, reproducibility errors represent systematic errors, measuring 0.3 K above and 0.75 K below 100 hPa for temperature and 3% and 5% for relative humidity at temperatures above 0 °C and between -40 and 0 °C, respectively. All the specified statistical uncertainties were at the 95% confidence level (see https://www.intermetsystems.com/products/imet-4-radiosonde/, last access: 25 September 2023). The temperature and water vapor profiles obtained from in situ radiosonde observations are considered representative of "true" atmospheric thermodynamic states (see Figure 3.2). These profiles serve as inputs to radiative transfer models for testing the radiative closure. However, since radiosondes can drift, their measurements may not always accurately represent zenith profiles. Table 3.1 lists precipitable water vapor (PWV) converted from radiosonde water vapor measurements in each field campaign. The small fluctuations in the temperature and water vapor vertical profiles have a negligible effect on AERI- and HiSRAMS-detected radiances (not shown).

In the boundary layer, temperature inversions with different inversion intensity and inversion depth were present in all three field campaigns (see the inset in Figure 3.2a), e.g., the two temperature inversions around 0.4 and 1.2 km in FC2021, the temperature inversion around 0.5 km in FC2022, and the temperature inversion around 0.8 km in FC2023. Drier layers associated with the temperature inversions were also observed in all three field campaigns (Figure 3.2b). Based on the temperature, dew point temperature, and water vapor profiles, the cause of the temperature inversions was subsidence. The sources and features (such as the fine vertical structure) of the temperature and water vapor anomalies exhibited in these profiles are beyond the scope of this paper but warrant future analyses.

Hourly-mean atmospheric state profiles from the fifth-generation European Centre for Medium-Range Weather Forecasts atmospheric reanalysis dataset, ERA5 (Hersbach et al., 2020), at 8×8 grid boxes containing the trajectory of each radiosonde (Figure 3.2c), were also included for analysis of the spatial variability of temperature and water vapor concentrations. Generally, the ERA5 hourly profiles agree well with radiosonde measurements, except that they do not resolve the aforementioned dry layers, likely due to their limited vertical resolution. Considering this, we mainly use radiosonde-observed temperature and water vapor profiles for the radiative closure analyses.

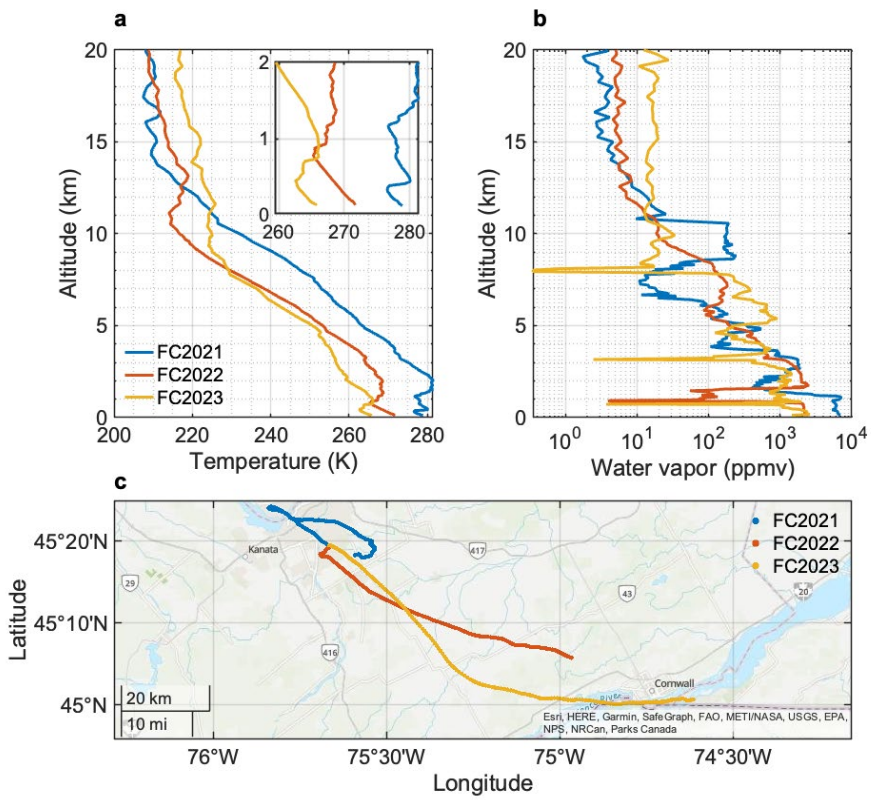

Figure 3.2: Radiosonde in situ measurements of (a) temperature and (b) water vapor concentration profiles in the three field campaigns, together with (c) radiosonde trajectories.

A higher vertical resolution is applied in the boundary layer compared to the upper troposphere and stratosphere because the AERI ground measurements are most sensitive to the lowermost layers. To avoid interpolating radiosonde measurements, the original temperature and relative humidity profiles are updated every 5 s until the balloon reaches 3 km, then every 15 s until it reaches 10 km, and finally every 60 s until the balloon reaches 20 km. Atmospheric conditions above 50 hPa (inclusive) from ERA5 are added to the top of the radiosonde measurements to form a hybrid full profile. Temperature and water vapor concentration at over 200 levels are provided in inputs to the radiative transfer models.

3.2.1.2 AERI spectra

AERI measures downwelling longwave radiance (DLR) emitted from the atmosphere from 520 to 3020 cm^{-1}, with a field of view (FOV) of 2.6°, a spectral resolution of 0.5 cm^{-1}, and a temporal resolution of 20 s (Knuteson et al., 2004a, 2004b). The units of radiance observed by AERI are the radiance units (RUs), representing 1 mW $(m^2\ sr\ cm^{-1})^{-1}$. In each 20 s observation cycle, aside from taking sky-view measurements, AERI also stares at two blackbodies, an ambient blackbody at the temperature of the surrounding air and a hot blackbody at a fixed temperature of 60 °C to radiometrically calibrate the measured DLR. In this study, the focus is on the AERI Channel 1 observations from 520 to 1800 cm^{-1}.

Given AERI is most sensitive to atmospheric conditions in the boundary layer (Turner & Blumberg, 2018), an accurate representation of near-surface temperature and water vapor concentration profiles is essential for analyzing the radiometric accuracy of AERI. Each balloon launch exceeds 1 h, during which the thermodynamic conditions may change considerably. Consequently, the original AERI-observed spectra, with a ~20 s sampling frequency, are averaged over the period from 2 min before to 8 min after the balloon launch to provide temporal sampling consistency between AERI observations (shown in Figure 3.3) and radiosonde profiles.

The radiance in the CO_2 absorption band centered at 667 cm^{-1} and the water vapor absorption band between 1400 and 1800 cm^{-1} indicates the radiating temperatures of the near-surface atmosphere. The radiance differences shown in Figure 3.3 correspond to the different air temperatures during the three field campaigns. The generally low radiance in the window band (800-1200 cm^{-1}) confirms a clear-sky condition during the three field campaigns. The radiance differences here indicate different PWV values. The radiance differences in the water vapor absorption band between 520 and 600 cm^{-1} also indicate the different PWV: the low PWV value of 0.32 cm in FC2023 led to very low radiance values in this spectrum.

In summary, the differences between the AERI spectra from the three field campaigns are qualitatively consistent with the differences in air temperature and water vapor concentrations.

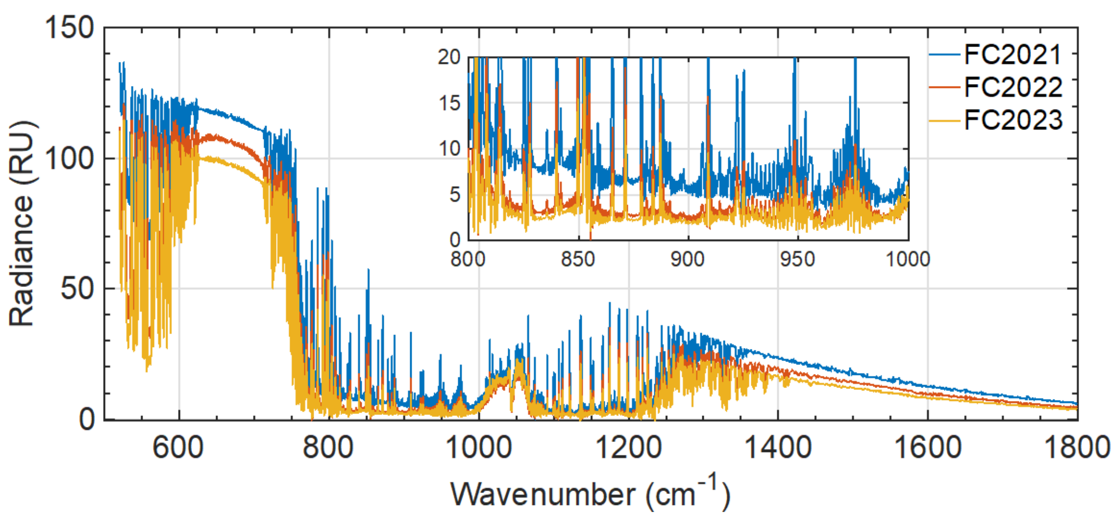

Figure 3.3: AERI-observed spectra. The spectra are averaged over a period from 2 min before to 8 min after the time of the balloon launch. (RU: radiance unit; 1 RU = 1 mW $[m^2 \text{ sr cm}^{-1}]^{-1}$)

3.2.1.3 HiSRAMS spectra

HiSRAMS consists of two radiometers, one targeting an oxygen absorption band and the other a water vapor absorption band. HiSRAMS can measure either single-polarized radiance over 49.6-58.3 GHz in the oxygen band and 175.9-184.6 GHz in the water vapor band or dual-polarized radiance over 52.4-57.2 GHz in the oxygen absorption band and 178.8-183.5 GHz in the water vapor band. Although dual-polarized measurements are valuable for characterizing radiance over water surfaces, this study focuses on single-polarized observations because the nadir-pointing measurements from FC2023 were mostly over land.

With its FFT filter banks, HiSRAMS achieves a spectral resolution as high as 305 kHz (Auriacombe et al., 2022). To reduce noise in brightness temperature (BT) measurements, the data were averaged to a 6.1 MHz resolution; i.e., the radiance was resampled every 20 original HiSRAMS channels. Each HiSRAMS radiometer is equipped with two FFT spectrometers: FFT0 and FFT1. In the case of single-polarization observations, both FFT spectrometers share an overlapping frequency range. For dual-polarization observations, the two FFT spectrometers have identical spectral ranges. HiSRAMS-observed spectra are calibrated regularly using measurements of a hot calibration load maintained at 80 °C as well as an ambient calibration load.

Ground-based zenith-pointing HiSRAMS observations of single-polarized spectra are averaged over the entire observation period shown in Figure 3.4. As with AERI measurements, differences between HiSRAMS spectra in the oxygen and water vapor absorption bands reflect the temperature and water vapor variations in the three clear-sky field campaigns. In the opaque frequency range of about 56 GHz in the oxygen band, the effective emitting layer lies close to the surface, resulting in the observed BT representing the near-surface temperature. Greater water vapor concentration results in a higher BT in the water vapor band.

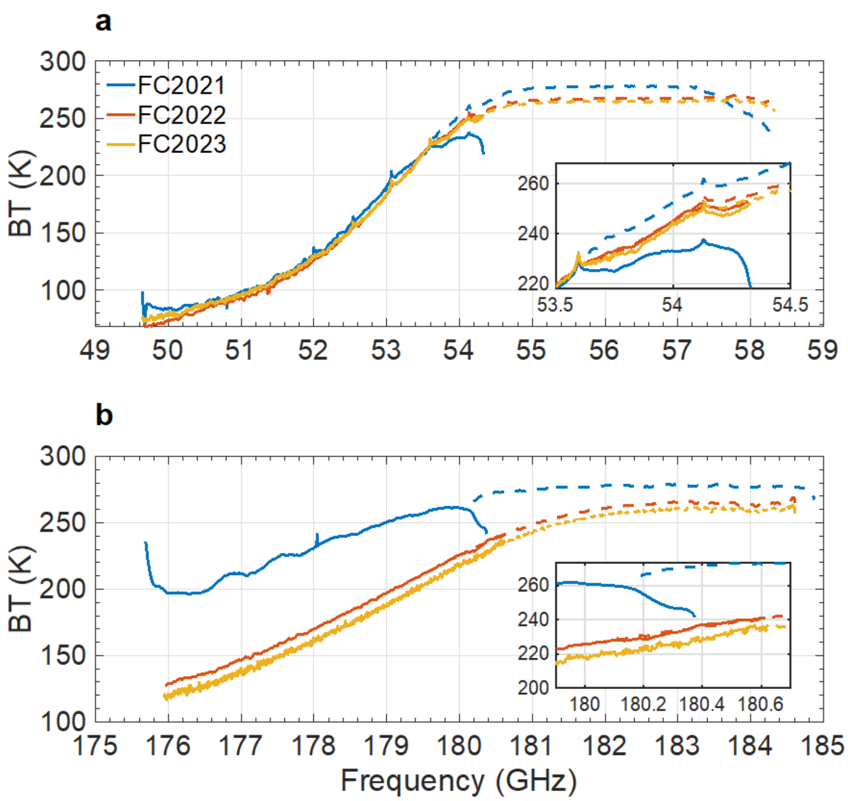

Figure 3.4: HiSRAMS-observed ground-based zenith-pointing spectra in the (a) oxygen band and (b) water vapor band. Solid and dashed lines show the observed spectra from the two overlapping spectrometers, FFT0 and FFT1, respectively.

In Figure 3.4, the observed spectra from the two FFT spectrometers are shown in solid lines (FFT0) and dashed lines (FFT1), respectively. In FC2021, unphysical signals at the edge of the spectral range were detected, herein referred to as a “roll-off” issue. This issue occurred in both FFT spectrometers, showing an overestimation of the radiance at the lower end of the frequency range and an underestimation at the higher end. Hence, discrepancies between the two spectrometers were identified within the overlapping frequency ranges in the oxygen and water vapor absorption bands (see the blue lines in the insets in Figure 3.4). One cause of the roll-off issue was attributed to incomplete image rejection in channels symmetric about the local oscillator frequency (Xu et al., 2023). After a refurbishment in the summer of 2022 to improve HiSRAMS' image rejection behavior and to better characterize the image response, the discrepancies between the two FFT spectrometers were significantly reduced.

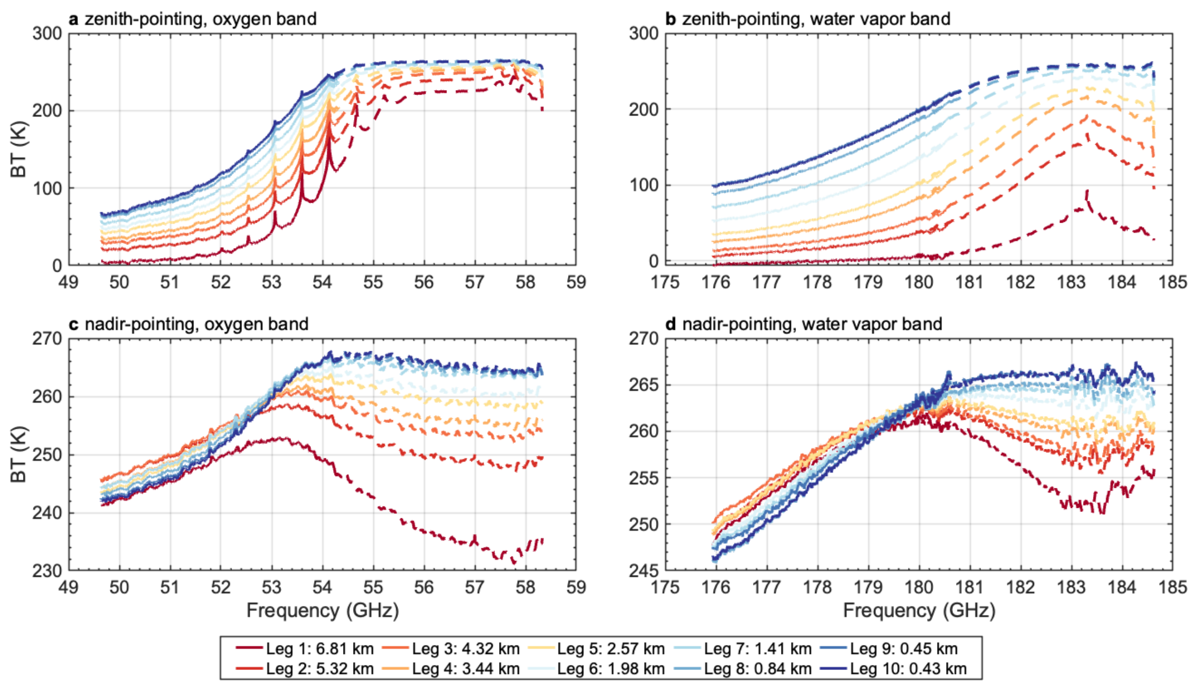

Figure 3.5: HiSRAMS-observed spectra during FC2023 flights at different altitudes. Solid lines are for FFT0 measurements and dashed lines are for FFT1 measurements. (a, b) Zenith-pointing and (c, d) nadir-pointing spectra in the oxygen and the water vapor band, respectively.

The HiSRAMS flight measurements taken during FC2023 are shown in Figure 3.5. Observations in both zenith and nadir directions were made over 10 straight-and-level flight legs on 11 February 2023, with altitudes ranging from 429 m to 6.8 km. After the HiSRAMS refurbishment, the observed spectra in the overlapping frequency range agreed well between the two FFT spectrometers in both the oxygen and water vapor absorption bands, at all flight altitudes.

In zenith-pointing spectra, the BT decreases with observation altitude in both the oxygen and water vapor bands (Figure 3.5a, Figure 3.5b) because of the corresponding overall decrease in temperature (and water vapor), resulting in lower emitting temperatures with increasing altitudes. In contrast, with nadir-pointing spectra in the strong absorption frequency range, e.g., 54-58 GHz in the oxygen band and 181-184 GHz in the water vapor band, the BT decreases with altitude because the emitting layer goes higher according to the $\tau = 1$ law; i.e., the altitude corresponding to $\tau = 1$ is where the weighting function peaks (Huang & Bani Shahabadi, 2014), resulting in a lower emitting temperature, while in the weak absorption frequency range, e.g., 49.5-52 GHz in the oxygen band and 176-179 GHz in the water vapor band, the BT increases overall with altitude as a result of competing contributions from the surface and from atmospheric emissions (Figure 3.5c, Figure 3.5d).

3.2.2 Forward model

In radiative closure tests, the radiometric accuracy of a radiometer is verified by comparing its measurements to synthetic spectra simulated by a radiative transfer model. The input of the temperature and water vapor concentration profiles to the radiative transfer model is taken from radiosonde measurements, as described above.

3.2.2.1 AERI forward model

We use the Line-by-Line Radiative Transfer Model Version 12.9 (LBLRTM v12.9, Clough et al., 2005) as the forward model for AERI synthetic spectra simulation. LBLRTM-computed monochromatic radiance spectra were convolved with the AERI scan function, enabling comparisons with AERI-measured spectra. Carbon dioxide concentrations (413.84, 418.75, and 419.72 ppmv), sourced from the global and monthly averaged marine surface values of the Global Monitoring Laboratory of the National Oceanic and Atmospheric Administration (Lan et al., version 2023-06), remain constant across all the vertical levels. Ozone and methane concentration profiles were taken from the ERA5 reanalysis dataset and the Copernicus Atmosphere Monitoring Service (CAMS) global atmospheric composition forecasts dataset (Inness et al., 2019), respectively. No CFC11 and CFC12 were prescribed in the synthetic spectra calculations. We undertook a comparison between the most recent version of LBLRTM, v12.16, and the version we chose, v12.9. The primary distinction arises within the far-infrared spectral range, where AERI observations exhibit a relatively large measurement uncertainty, attributed to inadequate calibration at the spectral detector's edge (see a detailed description in Section 3.5.1).

3.2.2.2 HiSRAMS forward model

The HiSRAMS forward model (Bliankinshtein et al., 2019) consists of two major components, the Rosenkranz gas absorption parameterization (Rosenkranz, 2017) and an efficient plane-parallel radiative solver that excludes multiple scattering but accounts for surface polarization. A sea surface emissivity model is used as an example boundary condition for nadir-pointing measurements. The forward model was validated against the Monochromatic Radiative Transfer Model, MonoRTM (Clough et al., 2005), and the Atmospheric Radiative Transfer Simulator, ARTS (Eriksson et al., 2011). To avoid uncertainty with regard to the surface contribution in the closure tests, nadir-pointing measurements taken at the lowest flight altitude (429 m) were employed as the boundary condition (i.e., elevating the surface to this altitude). The nadir-pointing measurement taken by HiSRAMS at 429 m already includes the contribution from the surface (i.e., the product of the surface emissivity and the blackbody emission at the effective skin temperature plus the reflected atmospheric downwelling radiation) as well as the impact of the atmosphere below 429 m. The boundary emissions propagating upwards, along with emissions from the atmosphere, constitute simulated measurements at higher flight legs.

3.2.3 Radiative closure diagnosis

In this study, the radiance or BT bias is defined as the instrument-measured radiance or BT minus the forward model-simulated radiance or BT, which provides a metric for evaluating the radiance closure:

$$\Delta R_{\upsilon} = R_{\upsilon,instrument-measured} - R_{\upsilon,model-simulated}, \qquad \text{where } R_{\upsilon} = Radiance\ or\ BT \quad (3.1)$$

The bias uncertainty derives from the instrument measurement uncertainty and model simulation uncertainty:

$$\sigma_{\Delta R_{\upsilon}} = \sqrt{\sigma_{R_{\upsilon,instrument-measured}}{}^{2} + \sigma_{R_{\upsilon,model-simulated}}{}^{2}}, \quad \text{where } R_{\upsilon} = Radiance\ or\ BT \quad (3.2)$$

The instrument measurement uncertainty for AERI is 1% of ambient blackbody radiance (3-σ), which is its absolute radiometric calibration accuracy (Knuteson et al., 2004a). For HiSRAMS measurements, if multiple individual measurements are averaged, the standard deviation of any individual measurements during the whole observational period is considered to be the uncertainty of the HiSRAMS-averaged measurements, which is applied to HiSRAMS ground measurements in FC2021 and FC2022 and flight measurements in FC2023. If only the individual observed spectrum is available, i.e., FC2023 HiSRAMS ground measurements, its uncertainty is determined by taking into account the radiometric noise characterized by the noise-equivalent differential temperature, calibration load imperfections, detector nonlinearity error, and instrument drift (Bliankinshtein, Gabriel, et al., 2023). Both the forward model uncertainty and the uncertainties associated with the input variables contribute to the total uncertainty in model simulations. Input uncertainties include radiosonde (instrumental) measurement errors and those arising from the spatial variability of the input profiles due to radiosonde drift. Both uncertainties are combined in quadrature similar to Equation 3.2. We used the ERA5 hourly-mean profile within the 8×8 grid box rectangular region, including the balloon trajectory (Figure 3.2c), to represent the spatial variability of the temperature and relative humidity profiles.

Randomly generated noise, accounting for both random errors, including radiosonde repeatability errors and the radiosonde drifting errors derived from ERA5 spatial variability in temperature and relative humidity, was added to the radiosonde profiles for each case. In total, 1000 profiles were created with this random noise. Subsequently, a single randomly determined radiosonde reproducibility error was added to each generated profile. Using radiative Jacobians, we determined the radiance or BT difference between using the original radiosonde profiles and using the randomly generated profiles as inputs. The standard deviation of the radiance or BT simulation from the 1000 generated profiles was utilized to represent the 1-σ model-simulated uncertainty. In all uncertainty analyses in the following discussion, the σ level is set to 3 standard deviations (99.7% confidence level).

3.3 Results

3.3.1 AERI

The DLR observed by AERI is most strongly influenced by the near-surface atmospheric thermodynamic state. Quality control of the AERI spectra was performed following Liu et al. (2022). For example, strong CO_2 and water vapor absorption channels subject to calibration errors were excluded in this analysis following the optical depth screening procedure of Liu et al. (2022).

Figure 3.6 exhibits the AERI radiative closure test results. Overall, the uncertainty in the DLR bias for AERI mainly derives from LBLRTM simulation uncertainties in the temperature-sensitive bands. In the window band, both measurement uncertainty and LBLRTM simulation uncertainty contribute to the total uncertainty.

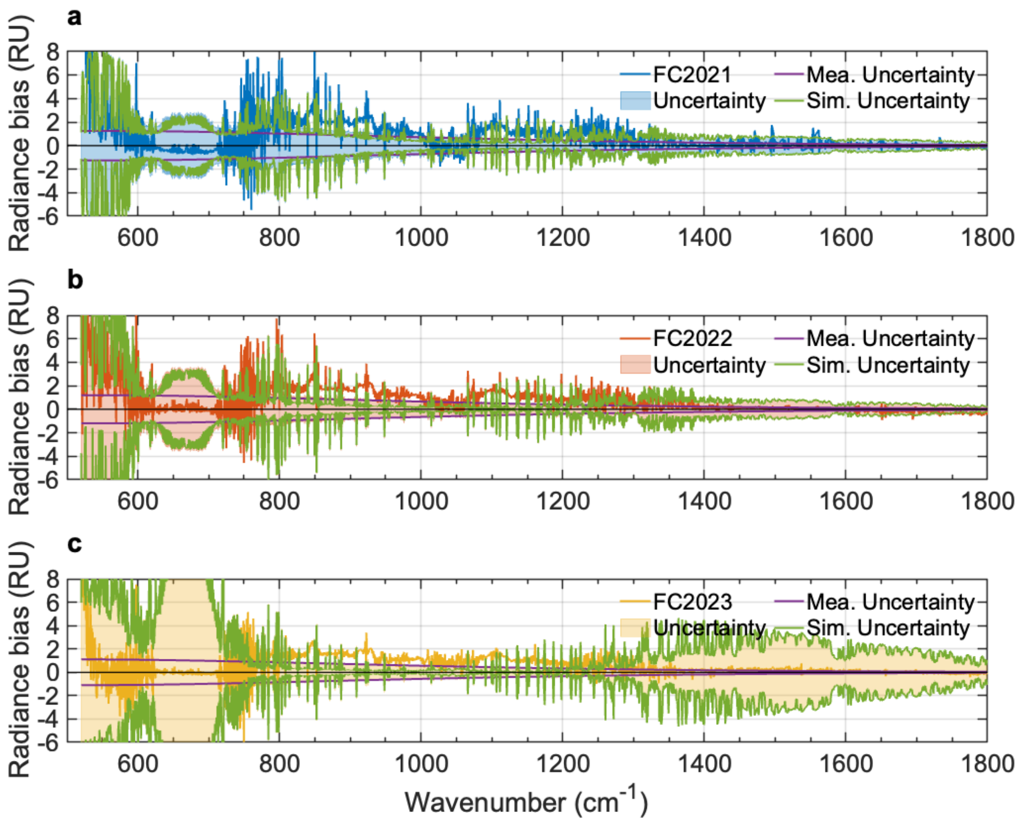

Figure 3.6: AERI radiative closure test results. Each panel represents one field campaign. The blue line in panel (a), the orange line in panel (b), and the yellow line in panel (c) represent the DLR bias between 10 min averaged AERI-observed and LBLRTM-simulated spectra. The purple lines and the green lines represent the AERI measurement uncertainty and LBLRTM simulation uncertainty, respectively. The shadings represent the total DLR bias uncertainty.

Good agreement between 10 min averaged AERI-observed spectra and LBLRTM-simulated spectra was observed in the CO_2 absorption band centered around 667 cm^{-1} and the water vapor absorption band of 1400-1800 cm^{-1}, controlled primarily by atmospheric temperature, indicating excellent closure between the radiance measurements of AERI and the temperature profiles collected by radiosondes.

Over the three field campaigns, a persistent and stable positive DLR bias in the window band was detected, with the mean biases from the three campaigns (blue line in Figure 3.7) far exceeding their standard deviation (orange line in Figure 3.7). Across many channels in the window band, the sigma level exceeds 4, indicating a more than 99.99 % likelihood that the bias mean will exceed the bias standard deviation for these three field campaigns. Moreover, the DLR bias in the window band in each of the field campaigns is larger than the DLR bias uncertainty (Figure 3.6). Because of the low BT in the window band, even a small radiance bias leads to a relatively large BT bias (Figure 3.7b). In this band, the radiance is primarily controlled by water vapor, aerosols, and clouds (Hansell et al., 2008; Seo et al., 2022). Through sensitivity tests (not shown), the bias was unlikely to be explainable by possible errors in the radiosonde water vapor measurements: over 150% of the original water vapor concentration in all the vertical layers would be needed to remove this bias (not shown). The presence of optically thin aerosols or clouds with an optical depth of ~0.06 at the altitude with a higher relative humidity may explain the magnitude of this bias. However, the almost constant values of this bias across all three field campaigns make this hypothesis less likely.

It is interesting to note that historical AERI data measured elsewhere have also exhibited relatively large biases in the window band under clear-sky conditions (Liu et al., 2022; Delamere et al., 2010). A FOV obstruction could introduce a positive radiance bias in the window band due to radiance leakage from the obstructive element having an emitting temperature higher than the scene temperature in the window band under clear-sky conditions (Turner, 2003). Based on a sensitivity test, the portion of obstructed FOVs needed to explain this warm bias in the window band is around 2% (not shown). Since all three field campaigns targeted cold and dry clear-sky atmospheric conditions whose calibration extrapolation process introduces larger uncertainties, it is also possible that calibration bias, e.g., the nonlinearity-induced inaccuracy, accounts for the radiance bias in the window band. Lower radiance in the window band draws the extrapolation further away from the blackbodies' emitted radiance, resulting in a larger calibration bias. However, whether the calibration process could lead to a consistent positive DLR bias in the window band is unknown.

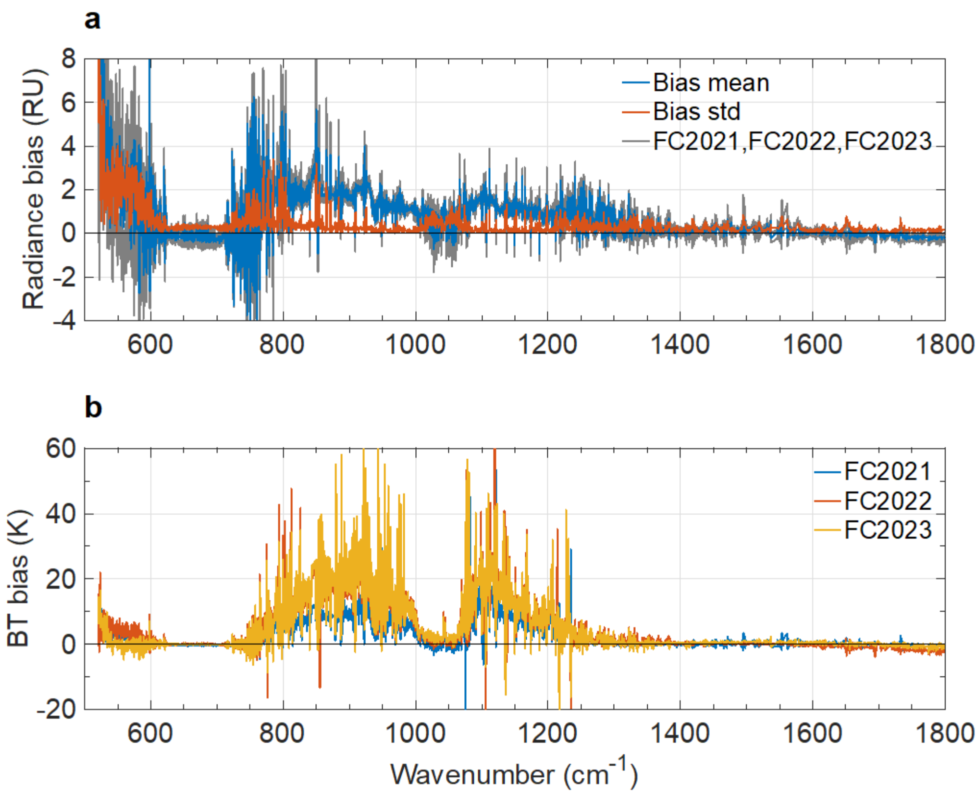

Figure 3.7: AERI radiative closure test results. (a) DLR bias. The grey lines show the DLR difference between 10 min averaged AERI-observed spectra and the LBLRTM-simulated synthetic spectra in the three campaigns. The blue line and the orange line represent the mean and standard deviation, respectively, of the DLR differences. (b) BT bias.

As a result, a systematic, consistent warm radiance bias in the window band for AERI clear-sky observations is present and removable for future retrieval analysis by subtracting the bias mean in channels whose radiance bias means (blue line in Figure 3.7a) are larger than their radiance bias standard deviation (orange line in Figure 3.7a). This correction is referred to as the AERI warm bias correction.

3.3.2 HiSRAMS

Radiative closure tests were performed on both the ground-based zenith-pointing measurements and the flight measurements of HiSRAMS. In light of the roll-off error in the FC2021 measurements previously noted, the following discussions focus on the results of FC2022 and FC2023, which show a better closure in both the oxygen and water vapor absorption band at the frequency edges of each FFT spectrometer after the HiSRAMS refurbishment (Figure 3.8). The radiative closure results for ground measurements in FC2022 and FC2023 as well as flight measurements in FC2023 are shown in Figure 3.9 and Figure 3.10, respectively. The two methods mentioned in Section 3.2.3 to determine the uncertainty of HiSRAMS ground measurements result in similar measurement uncertainties (purple lines in Figure 3.9), except for the significant measurement uncertainty at the edge of FFT1 for both the oxygen and water vapor band in FC2022, whose source is the remaining roll-off issue. This indicates that the frequency range with large measurement uncertainty, computed from the standard deviations of individual spectra, should be discarded in future retrieval analysis.

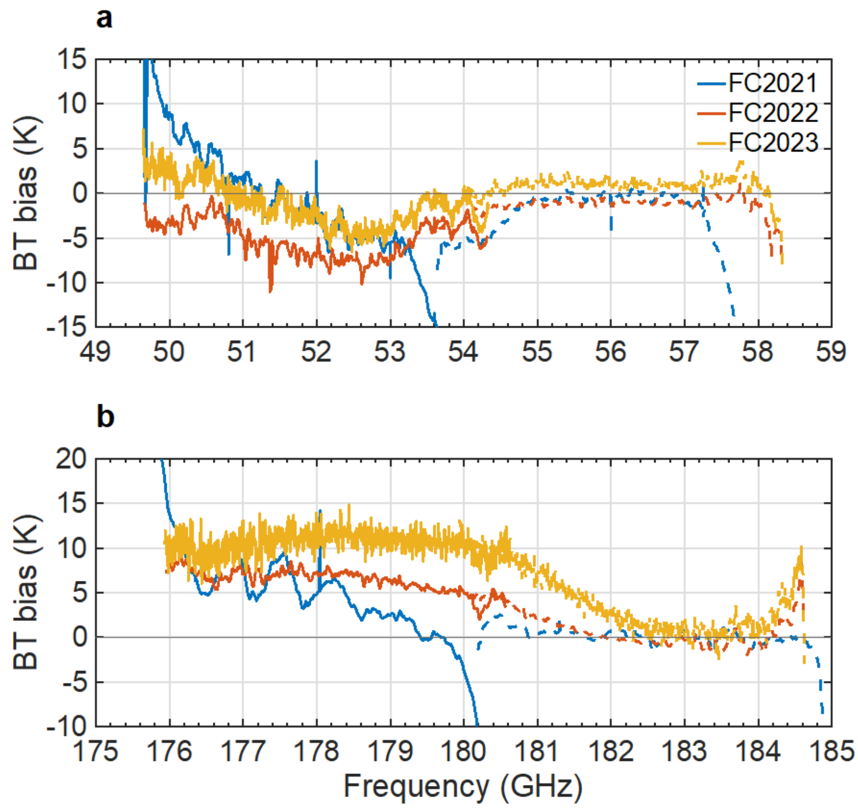

Figure 3.8: HiSRAMS-observed ground-based zenith-pointing spectral BT bias for the (a) oxygen band and (b) water vapor band. Solid and dashed lines show the observed spectra from FFT0 and FFT1, respectively.

The primary contribution to the radiative closure uncertainty in the weak absorption frequency range (50-54 GHz) of the zenith-pointing oxygen band radiometer is the measurement uncertainty. However, in the strong absorption frequency range (55-58 GHz), the simulation uncertainty could be similar to or larger than the measurement uncertainty, depending on the uncertainties in the vertical temperature profiles. The zenith-pointing BT bias in the strong absorption frequency range (55-58 GHz) is relatively small, falling within the radiative closure uncertainty (Figure 3.9a and Figure 3.9c). However, in the weak absorption channels (50-54 GHz), a notable BT bias occurs which exceeds the 3-σ BT bias uncertainty. In FC2022 and

FC2023, the BT bias for both ground and flight zenith-pointing measurements in the oxygen band has similar spectral shapes and magnitudes (except for leg-1 FC2023 flight measurements; these suffer from a large calibration bias discussed later), suggesting a systematic bias, which may come from the calibration process. The zenith-pointing BT biases in the oxygen band, excluding the leg-1 FC2023 flight measurements, exhibit a mean BT bias larger than the standard deviation of the BT biases (Figure 3.11), supporting the hypothesis that the bias may be systematic.

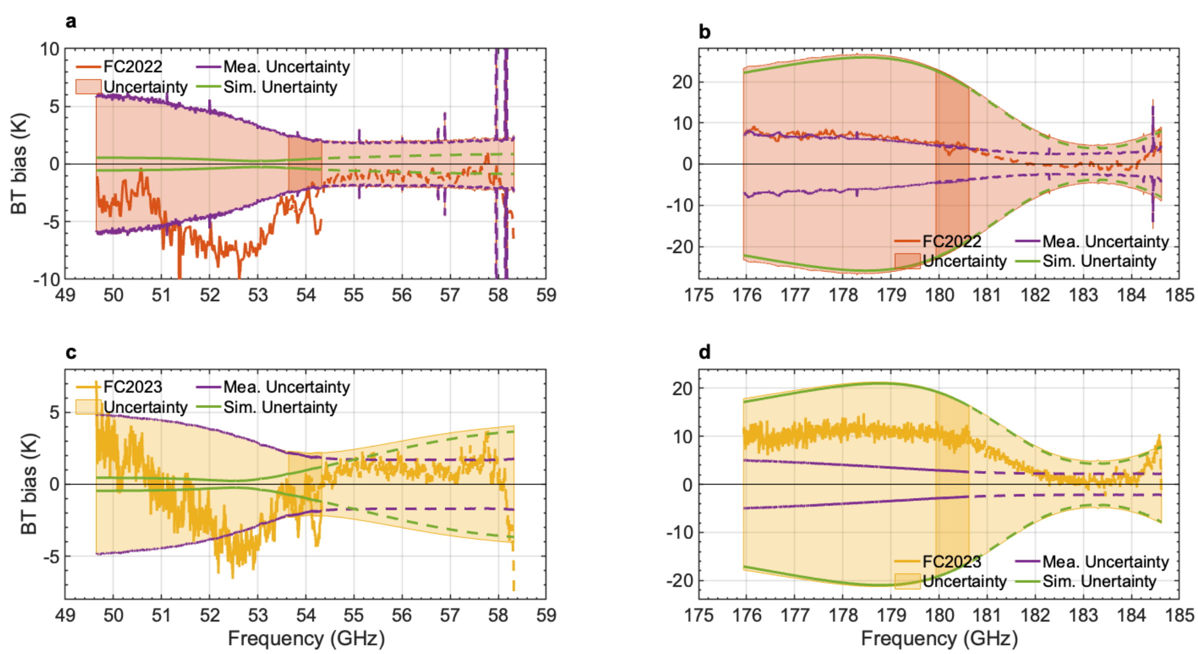

Figure 3.9: The ground-based zenith-pointing HiSRAMS radiative closure test results for the (a, c) oxygen band and (b, d) water vapor band. Orange lines in panels (a) and (b) and yellow lines in panels (c) and (d) represent the BT bias. In each panel, the shading represents the total uncertainty of the BT bias, while the purple and green lines represent the measurement uncertainty and simulation uncertainty, respectively.

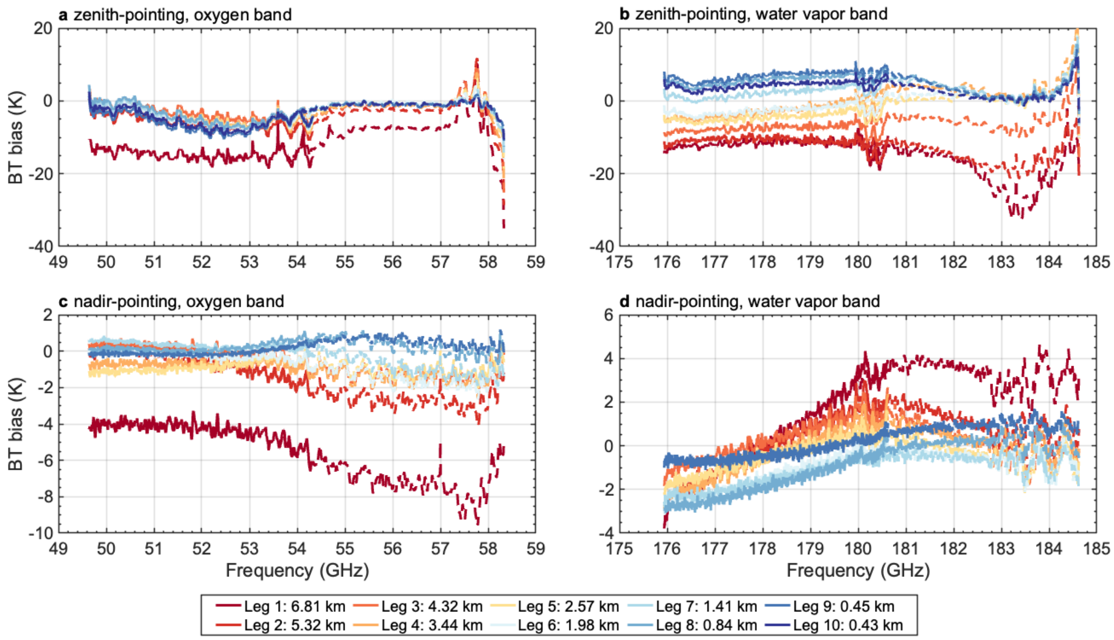

Figure 3.10: BT bias for FC2023 flight measurements at different observational altitudes. (a, b) Zenith-pointing BT bias in the oxygen and water vapor bands, respectively. (c, d) Nadir-pointing BT bias in the oxygen and water vapor bands, respectively.

Compared to the oxygen band radiometer's zenith-pointing BT bias uncertainty, simulation uncertainty primarily contributes to the radiative closure uncertainties in the water vapor band radiometer's zenith-pointing BT bias. A relatively smaller BT bias was present in the strong water vapor absorption band (182-184 GHz) in zenith-pointing ground measurements (Figure 3.9b and Figure 3.9d). There is a positive BT bias for both FC2022 and FC2023, with different magnitudes, in the weak absorption band at 176-180 GHz (Figure 3.9b and Figure 3.9d). This bias is within the 3-σ BT bias uncertainty. Measurements in different flight legs in FC2023 also show different BT biases in the water vapor absorption band (Figure 3.10b). Flight legs at lower altitudes tend to have positive BT biases; those in higher-altitude legs tend to have negative BT biases, which suggests that these biases may be environment-dependent. The correlation coefficients between the environmental temperature from radiosonde temperature measurements and the channel-averaged BT biases for FFT0 and FFT1 in the water vapor band are 0.90 and 0.87, respectively (Figure 3.12), suggesting that the source of the HiSRAMS bias in the water vapor absorption band is related to the calibration processes.

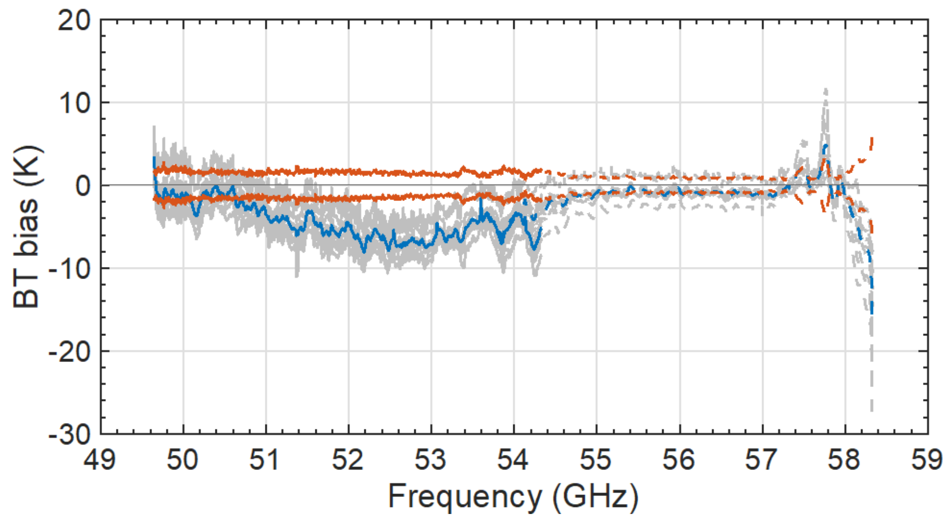

Figure 3.11: HiSRAMS radiative closure results for the zenith-pointing oxygen band measurements from FC2022 and FC2023 ground measurements as well as FC2023 flight measurements. The grey lines represent individual BT biases for different conditions. The blue and orange lines represent the mean BT bias and the standard deviation of the BT biases, respectively.

A more accurate radiative closure was achieved for nadir-pointing HiSRAMS flight measurements (Figure 3.10c, Figure 3.10d) compared to the zenith-pointing HiSRAMS flight measurements (Figure 3.10a, Figure 3.10b). BT biases within 3 K were observed for nadir-pointing HiSRAMS measurements at all observational altitudes below 5.32 km.

Flight leg 1 (6.81 km) exhibits relatively poor radiative closure for all observational conditions and spectral ranges, which is an absolute outlier from the radiative closure for other flight legs. The HiSRAMS calibration process is sensitive to the environmental temperature; validation of the HiSRAMS calibration was performed in a well-controlled laboratory environment. However, the difference in environmental temperature during the flight measurements may introduce a larger bias into HiSRAMS measurements (Bliankinshtein, Gabriel, et al., 2023).

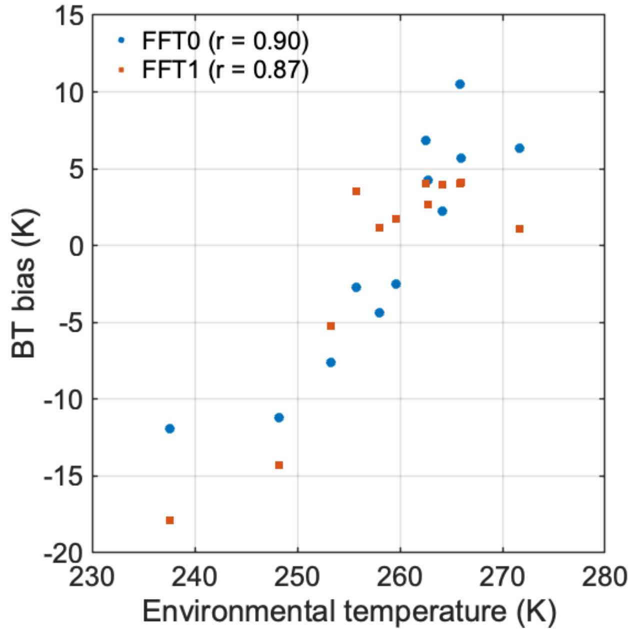

Figure 3.12: Scatter plot between HiSRAMS zenith-pointing averaged BT biases in the water vapor band (FFT0 and FFT1) and environmental temperature from radiosonde measurements. r represents the correlation coefficients.

Because the zenith-pointing BT in the water vapor absorption band is highly sensitive to variations in water vapor vertical profiles, the uncertainty in the water vapor input results in the relatively large BT bias shown in Figure 3.9b, Figure 3.9d, and Figure 3.10b. This strong sensitivity could be beneficial to water vapor concentration retrieval if the accuracy of the HiSRAMS zenith-pointing measurements under different environmental conditions can be ensured; this requires more HiSRAMS ground-based and flight measurements.

3.3.3 Comparison of HiSRAMS and AERI radiative accuracy

As an established hyperspectrometer, AERI can be used to evaluate the accuracy of the HiSRAMS experimental radiometers. The BT biases in both AERI and HiSRAMS measurements are organized with respect to the total column optical depth for the channels dominated by either CO_2 or water vapor absorptions for AERI (see detailed AERI channel selection in Section 3.5.2) and all the channels for HiSRAMS (Figure 3.13). In the original AERI measurements, the BT bias decreases overall with optical depth. The BT bias has a broader spread when the optical depth is low (Figure 3.13a); this may arise from the slight wavenumber mismatch between AERI observations and LBLRTM simulations. After the warm bias correction, a more accurate radiative closure of AERI is achieved (Figure 3.13b) with a lower BT bias and a standard deviation for both the CO_2 and water vapor channels.

Nadir-pointing HiSRAMS measurements display consistent radiometric characteristics across various optical depth ranges. The mean BT bias for nadir-pointing HiSRAMS measurements is relatively small, and the spread of the BT bias at different optical depths is minimal (Figure 3.13c, Figure 3.13d). In contrast, the zenith-pointing HiSRAMS BT bias does not exhibit a straightforward relationship with optical depth. Within the oxygen band, where optical depth is relatively large, the BT bias is close to zero, showing good radiometric accuracy (Figure 3.13e). However, at other optical depth ranges within the oxygen band and across the entire optical depth range in the water vapor band, the BT biases are substantial, with a significant standard deviation. It is important to note that, in nadir-pointing measurements, the elevated surface setting may mitigate the BT biases between the measurement and the simulation. This is because the surface contribution in the simulation is derived from the measurement.

Figure 3.14 compares the radiometric accuracy of AERI and HiSRAMS. The results for the mean BT bias and the standard deviation of the BT biases at different optical depth ranges are shown. The optical depth here refers to the total column optical depth along the entire light path. Considering the corrected AERI radiometric accuracy to be the benchmark, the nadir-pointing HiSRAMS measurements (yellow and purple dots and shadings in Figure 3.14) agree well with the corrected AERI measurements (orange dots and shading in Figure 3.14). The zenith-pointing HiSRAMS measurements (green and black dots and shadings) clearly diverge from the corrected AERI measurements, indicating poorer radiometric accuracy. When comparing the radiometric accuracy of AERI and HiSRAMS in zenith-pointing measurements, the viewing geometry of the two instruments is identical, ensuring a fair comparison. However, when comparing the radiometric accuracy between AERI zenith-pointing measurements and HiSRAMS nadir-pointing measurements, it is necessary to consider their different viewing geometries, as this could also affect the radiometric accuracy.

In conclusion, nadir-pointing HiSRAMS measurements in the oxygen and water vapor bands have a similar radiometric accuracy to the AERI benchmark. However, poor radiometric accuracy has been observed in zenith-pointing HiSRAMS measurements in the oxygen and water vapor bands, indicating the necessity of improving HiSRAMS's zenith-pointing radiometric accuracy calibration.

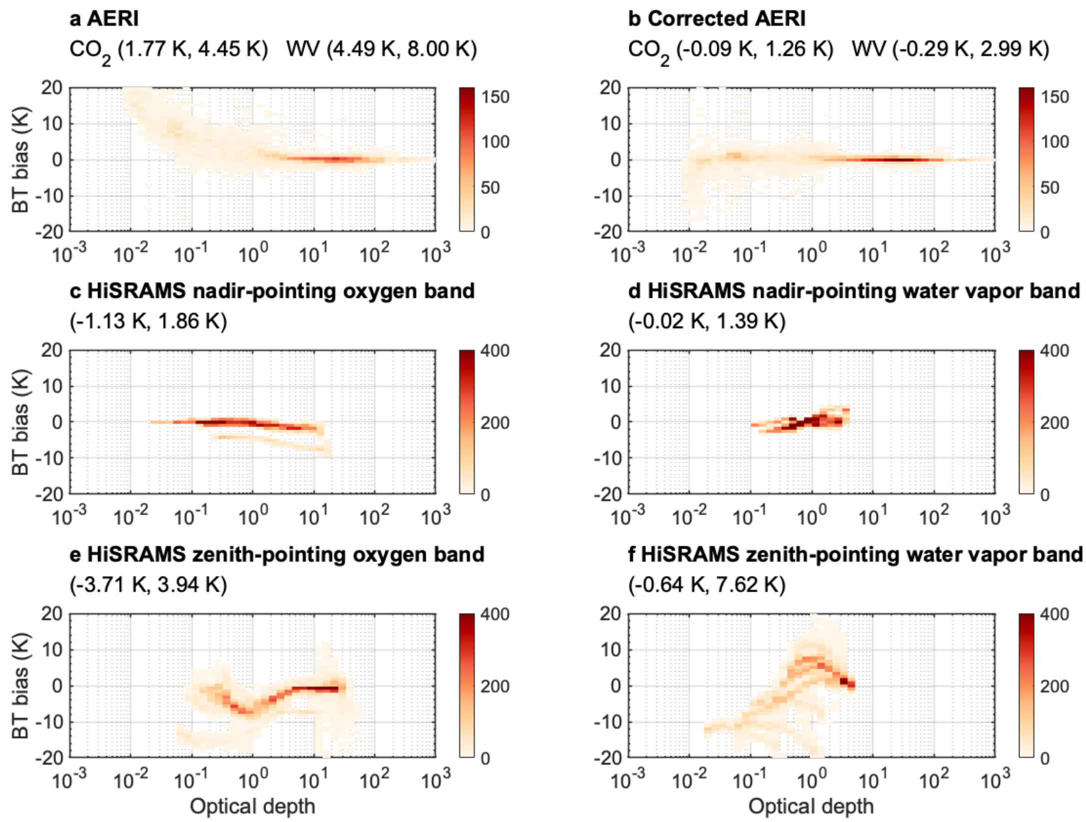

Figure 3.13: BT biases with respect to optical depth at different channels for (a) AERI measurements, (b) corrected AERI measurements, (c) nadir-pointing HiSRAMS oxygen band measurements, (d) nadir-pointing HiSRAMS water vapor band measurements, (e) zenith-pointing HiSRAMS oxygen band measurements, and (f) zenith-pointing HiSRAMS water vapor measurements. The color represents the number of channels. The numbers in the parentheses represent the mean and standard deviation of the BT biases, respectively. For AERI measurements, only channels dominated by either carbon dioxide or water vapor absorptions are included.

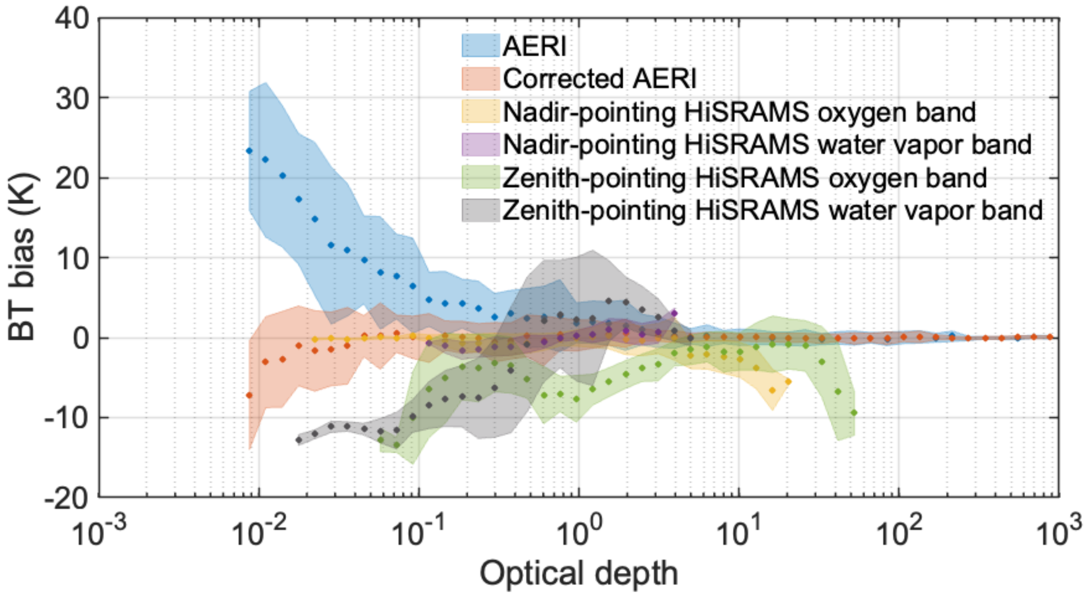

Figure 3.14: Mean (dots) and standard deviation (shadings) of BT biases with respect to optical depth at different channels for AERI observations, corrected AERI observations, nadir-pointing HiSRAMS observations, and zenith-pointing HiSRAMS observations. For AERI measurements, only channels dominated by either carbon dioxide or water vapor absorptions are included.

3.4 Conclusions and discussions

Vertical temperature and water vapor concentration profiles are essential for climate and weather studies. Hyperspectral radiometers have been shown to be useful in retrieving high temporal and spatial resolution profiles of temperature and water vapor concentration. Advancements in millimeter-wave technologies have made possible the development of hyperspectral microwave radiometers exhibiting thousands of channels. HiSRAMS, designed and developed by an international team, is an instance of such a development. The radiometric accuracy of this experimental instrument was evaluated under clear-sky conditions, employing collocated clear-sky AERI and HiSRAMS spectral measurements collected in Ottawa, Canada, together with the radiosonde measurements of temperature and water vapor concentration profiles. Determining the radiometric accuracy of the two HiSRAMS hyperspectral radiometers is a prerequisite for temperature and water vapor concentration retrievals.

Three field campaigns were conducted to evaluate the radiometric accuracy of AERI and HiSRAMS. The radiance bias in the temperature-sensitive bands in AERI observations is relatively small, indicating a good accuracy of the temperature inputs from radiosonde measurements. A persistent warm bias in the window band was present in AERI measurements, which may be due to the FOV obstruction or calibration processes; this can be corrected. Upon implementing the warm bias correction in AERI measurements, a more accurate radiometric closure was achieved in the window band. HiSRAMS nadir-pointing spectra from flight measurements exhibit a smaller BT bias compared to zenith-pointing spectra from both ground and flight measurements. Zenith-pointing HiSRAMS water vapor band measurements are sensitive to changes in water vapor concentration, underscoring the importance of accurate HiSRAMS measurements for water vapor concentration retrievals. It is essential to note that the sample size for this study was limited to three field campaigns, each accompanied by one radiosonde launch. The two instruments, HiSRAMS and AERI, are planned to be deployed in additional field campaigns and calibration experiments in the future, which will validate the closure assessment concluded here.

A novel but straightforward method was developed to test the radiometric accuracy of the instruments based on the relationship between radiative closure bias and total column optical depth. The radiometric accuracy of HiSRAMS was compared against the well-tested instrument AERI. Based on the BT bias in different optical depth ranges, nadir-pointing HiSRAMS measurements exhibit a radiometric accuracy comparable to AERI. However, poorer radiometric accuracy was observed in the zenith-pointing HiSRAMS measurements. To fully assess the source of this measurement bias, improved calibration and field campaigns are required.

The objective of designing and developing HiSRAMS is to test the retrieval performance of temperature and water vapor concentration from hyperspectral microwave observations under clear- and cloudy-sky conditions. This study focuses on the radiometric accuracy of HiSRAMS and AERI under clear-sky conditions as a first step. Future work will include comparisons of temperature and water vapor retrieval performance between hyperspectral infrared and microwave radiometers under clear-sky conditions, assessing the synergy of HiSRAMS and AERI observations for temperature and water vapor retrieval under clear-sky conditions and validating the all-sky radiometric accuracy of HiSRAMS as well as all-sky temperature, water vapor, and cloud retrievals based on HiSRAMS.

3.5 Supplement of "Radiative closure tests of collocated hyperspectral microwave and infrared radiometers"

3.5.1: The impact of the LBLRTM versions

The most recent release of LBLRTM, v12.16, became available in December, 2022. We compared the radiative closure difference for AERI measurements between utilizing v12.9 and v12.16 (Figure 3.15). The primary discrepancy arises in the far-infrared spectral range. Within the spectral range exhibiting notable radiance disparities between the two LBLRTM versions, the radiance differences between simulations and actual observations are already significant due to relatively insufficient calibration at the spectral detector's edge. We began simulating the AERI-observed DLR in 2018. To ensure consistency with our previous work, we decided to utilize version 12.9 in this study.

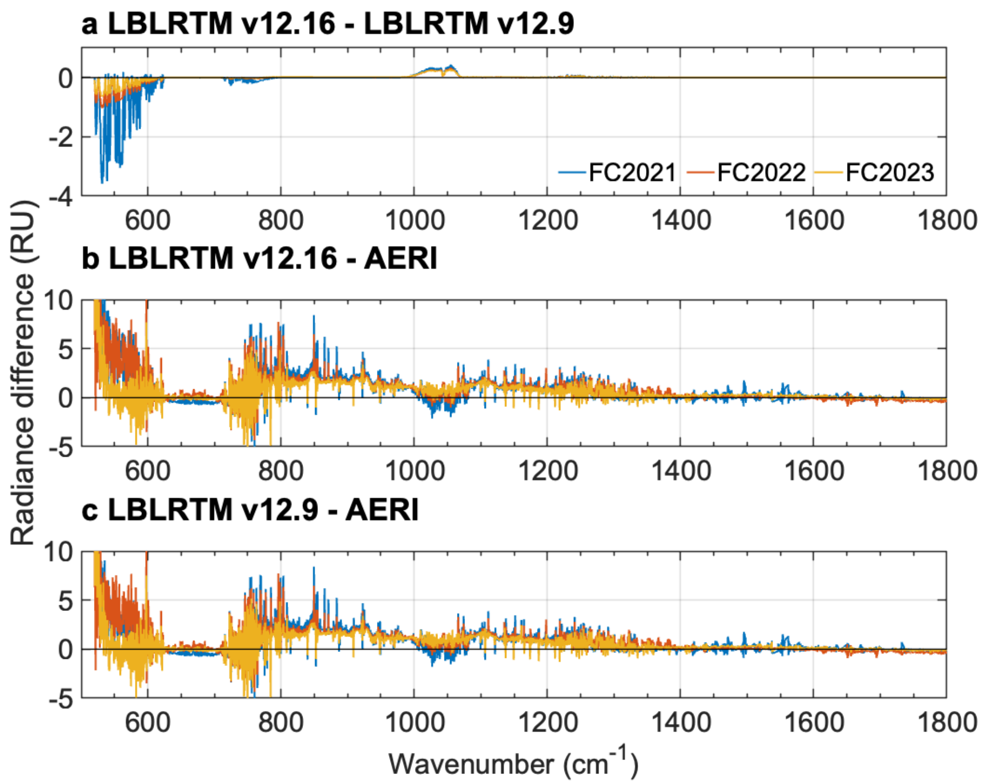

Figure 3.15: (a) DLR difference between LBLRTM simulations using version 12.16 and version 12.9. (b) DLR difference between LBLRTM v12.16 simulations and AERI observations. (c) DLR difference between LBLRTM v12.9 simulations and AERI observations.

3.5.2: The AERI channel selections

Different greenhouse gases exhibit distinct absorption features at various AERI channels. Using FC2023 data, we computed the total column optical depth contributed by different greenhouse gases (CO_2, H_2O, O_3, CH_4, N_2O, and CFCs) at each AERI channel. Subsequently, each AERI channel is labeled based on the greenhouse gas that contributes the most to the total column optical depth (Figure 3.16).

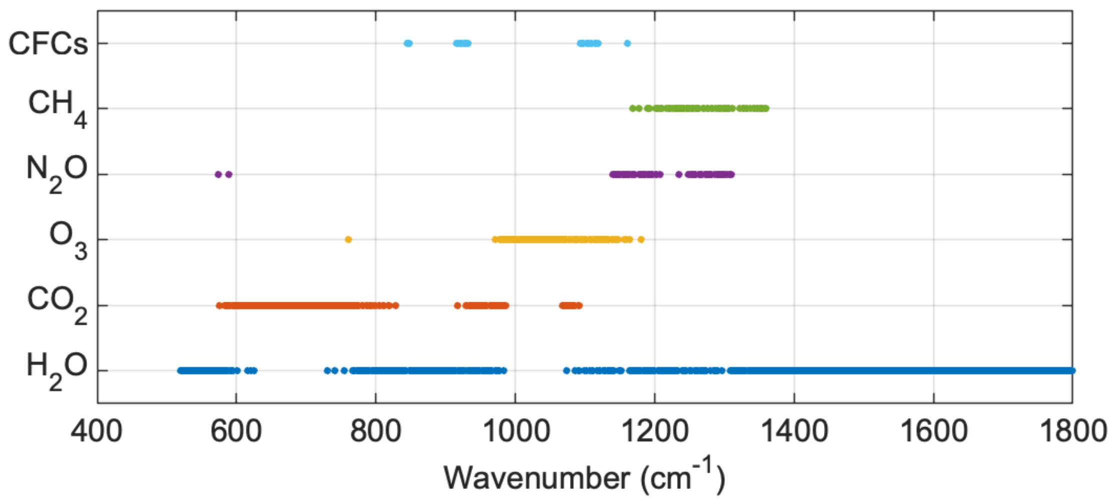

Figure 3.16: AERI channel labels. Each AERI channel is labeled according to the greenhouse gas that contributes the most to the total column optical depth.

Chapter 4 COMPARATIVE EXPERIMENTAL VALIDATION OF MICROWAVE HYPERSPECTRAL ATMOSPHERIC SOUNDINGS IN CLEAR-SKY CONDITIONS

Chapter 4 is a manuscript under review in *Atmospheric Measurement Techniques*. It is a complete reprint of the material as it appears in Liu, L., Bliankinshtein, N., Huang, Y., Gyakum, J. R., Gabriel, P. M., Xu, S., and Wolde, M.: Comparative experimental validation of microwave hyperspectral atmospheric soundings in clear-sky conditions, EGUsphere [preprint], https://doi.org/10.5194/egusphere-2024-1045, in review, 2024. The thesis author was the primary investigator and author of this paper.

Comparative experimental validation of microwave hyperspectral atmospheric soundings in clear-sky conditions

Lei Liu[1], Natalia Bliankinshtein[2], Yi Huang[1], John R. Gyakum[1], Philip M. Gabriel[3], Shiqi Xu[2], Mengistu Wolde[2]

[1]Department of Atmospheric and Oceanic Sciences, McGill University, Montreal, Quebec, Canada

[2]Flight Research Laboratory, National Research Council Canada, Ottawa, Ontario, Canada

[3]Horizon Science and Technology, Wolfville, Nova Scotia, Canada

Corresponding author: Lei Liu (lei.liu5@mail.mcgill.ca)

Abstract

Accurate observations of atmospheric temperature and water vapor profiles are essential for weather forecasting and climate change detection. Hyperspectral radiance measurements afford a useful means to retrieve these thermodynamic variable fields, by harnessing the rich information contained in the electromagnetic wave spectrum of the atmospheric radiation. Compared to infrared radiometry, microwave radiometry holds the ability to penetrate clouds and potentially achieve an all-sky thermodynamic retrieval. Recent technological advancements have enabled the development of a hyperspectral microwave radiometer, the High Spectral Resolution Airborne Microwave Sounder (HiSRAMS), which we employ in this study to retrieve the atmospheric temperature and water vapor profiles under the clear-sky condition, in comparison with an infrared hyperspectrometer, the Atmospheric Emitted Radiance Interferometer (AERI). HiSRAMS and AERI measurements under different viewing geometries have been acquired and compared for atmospheric retrieval. When both instruments are placed on the ground to acquire zenith-pointing measurements, the infrared hyperspectral measurements exhibit higher information content and greater vertical resolution for temperature and water vapor retrievals than the microwave hyperspectral measurements. A synergistic fusion of HiSRAMS and AERI measurements from the air and ground, respectively, is tested. This "sandwich" sounding of the atmosphere takes advantage of the complementary information contents of the two instruments and is found to notably improve retrieval accuracy.

4.1 Introduction

Temperature and water vapor concentration vertical profiles are fundamental thermodynamic variable fields and play a crucial role in diverse meteorological applications, ranging from extreme weather forecasting to long-term climate change detection (Guo et al., 2020; Langland & Baker, 2004; Laroche & Sarrazin, 2010; Thorne et al., 2011; Wang et al., 2016). Multiple methods are employed to measure these profiles, including direct, in situ measurements through radiosondes and aircrafts (Bliankinshtein, Liu, et al., 2023; Durre et al., 2006; Petzold et al., 2015; Zhou et al., 2021), indirect, remote sensing measurements obtained from spectrally resolved radiance (Aires et al., 2015; Loveless, 2021; Turner & Blumberg, 2018; Susskind et al., 2003; Susskind et al., 2010; Pougatchev et al., 2009), and data assimilation (Gelaro et al., 2017; Hersbach et al., 2020).

Direct measurements offer precise temperature and water vapor concentration profiles but have limited spatial and temporal coverage, in contrast to indirect, remote sensing (spectral) measurements, essential for regional and global weather and climate analyses. In these measurements, the temperature and water vapor information is typically encoded in the atmospheric radiance spectra. An algorithm is required to retrieve this information from atmospheric emission, absorption, or scattering features of the atmosphere across various frequency ranges. Hyperspectral measurements are particularly useful in this application because the high spectral resolution translates to richer information content. Several hyperspectral measurement methods were undertaken for atmospheric temperature and water vapor soundings; these can be categorized in terms of deployment platform (e.g., ground-based, airborne, or spaceborne) or frequency range (infrared, microwave, or other radiometers).

Clouds cover more than half of the Earth's surface (Stubenrauch et al., 2010), wielding a significant impact on hyperspectral temperature and water vapor retrievals, primarily due to their masking effect (McNally & Watts, 2003). In the infrared spectral range, clouds tend to be optically thick, effectively obscuring the atmosphere and preventing the retrieval of the target (atmospheric temperature and water vapor) behind the cloud layer. In contrast, microwave signals penetrate clouds, enabling the retrieval of temperature and water vapor profiles of the entire atmospheric column and a true all-sky sounding of the atmosphere.

For this reason, microwave radiometers have been a subject of active studies for decades (Aires et al., 2015; Blackwell et al., 2010; Hilliard et al., 2013; Smith et al., 2021). In the past, microwave radiometers typically had several or, in rare cases, dozens of channels, limiting the vertical resolution of temperature and water vapor retrievals. However, recent advancements in microwave Fast Fourier Transfer (FFT) filter techniques have led to the development of very high spectral resolution microwave radiometers, offering similar numbers (thousands) of channels to infrared hyperspectral radiometers and the potential for an information content boost. In this study, we deploy an airborne hyperspectral microwave spectrometer, the High Spectral Resolution Airborne Microwave Sounder (HiSRAMS), developed by an international team (Auriacombe et al., 2022; Bliankinshtein, Liu, et al., 2023). HiSRAMS is equipped with two radiometers and operates in the microwave spectral ranges covering two absorption bands of oxygen and water vapor respectively. It can be configured to measure single-polarized or dual-polarized radiance. As an airborne instrument, it can provide both zenith-pointing (looking up) and nadir-pointing (looking down) measurements (Bliankinshtein, Liu, et al., 2023).

A ground-based infrared radiometer, the Atmospheric Emitted Radiance Interferometer (AERI), was also utilized in this study to compare with HiSRAMS in terms of temperature and water vapor concentration retrieval performance. AERI is a well-tested infrared interferometer, which measures downwelling radiance emitted from the atmosphere between 520 and 3200 cm^{-1} with a spectral resolution of 0.5 cm^{-1} (Knuteson et al., 2004a, 2004b). AERI has been used to retrieve temperature and water vapor vertical profiles using the Optimal Estimation method with acceptable accuracy, particularly for near-surface profiles (Feltz et al., 1998, 2003; Turner & Blumberg, 2018; Turner et al., 2000; Turner & Löhnert, 2014).

While the primary advantage of microwave radiometers lies in their ability to retrieve in cloudy-sky conditions, this study focuses initially on clear-sky retrievals. The study has two main objectives: 1) to test the abilities of HiSRAMS and AERI to retrieve temperature and water vapor profiles while they are both placed on the ground taking zenith measurements, which provides identical conditions for assessing the two hyperspectral instruments in terms of their retrieval performance; 2) to test a synergistic retrieval combining AERI's ground-based zenith measurements with HiSRAMS' airborne nadir measurements, which allows the exploration of the complementary information from the two instruments operating in different spectral ranges and observing from different viewing geometries.

4.2 Field campaigns

Two field campaigns were conducted to retrieve vertical profiles of temperature and water vapor concentration profiles using AERI and HiSRAMS. The first campaign, denoted as FC2022, took place on December 9, 2022; the second campaign, FC2023, on February 11, 2023. During both campaigns, AERI and HiSRAMS measurements were collected alongside radiosonde data. FC2022 was a ground-based campaign, with AERI and HiSRAMS solely acquiring zenith-pointing measurements from the ground. In contrast, FC2023 included ground measurements of HiSRAMS and AERI and flight measurements of HiSRAMS at various observational altitudes. A thorough description of the field campaigns, particularly the radiative closure analysis of AERI and HiSRAMS measurements, can be found in Liu et al. (2023). This study focuses on the FC2023 campaign, during which the highest observational altitude of HiSRAMS reached 6.8 km, which allows us to validate the temperature and water vapor concentration retrievals within the troposphere against the measurements of radiosonde and aircraft. The HiSRAMS measurements used in this study are single-polarized measurements.

4.3 Retrieval algorithms

Our retrieval algorithms, employing HiSRAMS and AERI data, are based on the optimal estimation method (Loveless, 2021; Rodgers, 2000; Turner & Blumberg, 2018). These instruments measure the radiance, $\boldsymbol{y}$, received by their respective detectors. A forward model, $\boldsymbol{F}$, is utilized to simulate the radiance $\boldsymbol{F}(\boldsymbol{x})$ under the atmospheric state conditions, $\boldsymbol{x}$, shown in Equation 4.1. The AERI forward model we adopt is the Line-by-Line Radiative Transfer Model Version 12.9 (LBLRTM) and the HiSRAMS forward model has been developed and validated by Bliankinshtein et al. (2019). More details of the forward models can be found in Liu et al. (2023). In this study, the state vector $\boldsymbol{x}$ encapsulates vertical profiles of temperature and water vapor concentration. $\boldsymbol{\varepsilon}$ represents the error including both the measurement error and the forward model error.

$$\boldsymbol{y} = \boldsymbol{F}(\boldsymbol{x}) + \boldsymbol{\varepsilon} \tag{4.1}$$

Linearizing the relationship between $\boldsymbol{x}$ and $\boldsymbol{y}$ at a reference state $\boldsymbol{x_0}$:

$$\boldsymbol{y} = \boldsymbol{F}(\boldsymbol{x_0}) + \frac{\partial \boldsymbol{F}(\boldsymbol{x})}{\partial \boldsymbol{x}}(\boldsymbol{x} - \boldsymbol{x_0}) + \boldsymbol{\varepsilon} = \boldsymbol{F}(\boldsymbol{x_0}) + \boldsymbol{K}(\boldsymbol{x} - \boldsymbol{x_0}) + \boldsymbol{\varepsilon} \tag{4.2}$$

Here $\boldsymbol{K} = \frac{\partial \boldsymbol{F}(\boldsymbol{x})}{\partial \boldsymbol{x}}$ is the Jacobian matrix, representing the sensitivity of the forward model to the state vector. $\boldsymbol{K_{AERI}}$ and $\boldsymbol{K_{HiSRAMS}}$ are obtained by the analytical Jacobian method using their respective forward models. This linearization is a good approximation for the temperature values under question. However, for water vapor, we find that linearization works better for the logarithm of the water vapor concentration (Huang & Bani Shahabadi, 2014). Thus, $\boldsymbol{x_T} = \boldsymbol{T}$ and

$\boldsymbol{x_q} = \boldsymbol{log(q)}$, where $\boldsymbol{T}$ represents atmospheric temperature in units of K and $\boldsymbol{q}$ represents atmospheric water vapor in units of ppmv.

The objective of the retrieval is to infer $\boldsymbol{x}$ from $\boldsymbol{y}$. To address the nonunique correspondence between the atmospheric state conditions and the radiance, the Optimal Estimation method minimizes the cost function $\boldsymbol{J}$ or optimizes *a posteriori*. Applying the Levenberg-Marquardt iteration method and using a multiplier $\boldsymbol{\gamma}$ to stabilize the iteration processes by assigning varying weights between the measurement and the *a priori* (Rodgers, 2000), the state vector at iteration step $\boldsymbol{j+1}$, $\boldsymbol{x_{j+1}}$, is determined by Equation 4.3. The maximum step number is arbitrarily set to be 20. For all the retrieval cases in this study, the state vector converges before the maximum iteration step.

$$\boldsymbol{x_{j+1}} = \boldsymbol{x_j} + \left[\boldsymbol{K_j}^{\boldsymbol{T}}\boldsymbol{S_e}^{-\boldsymbol{1}}\boldsymbol{K_j} + (\boldsymbol{1}+\boldsymbol{\gamma})\boldsymbol{S_a}^{-\boldsymbol{1}}\right]^{-\boldsymbol{1}}\left\{\boldsymbol{K_j}^{\boldsymbol{T}}\boldsymbol{S_e}^{-\boldsymbol{1}}\left[\boldsymbol{y} - \boldsymbol{F}(\boldsymbol{x_j})\right] - \boldsymbol{S_a}^{-\boldsymbol{1}}(\boldsymbol{x_j} - \boldsymbol{x_a})\right\} \quad (4.3)$$

Here, $\boldsymbol{S_e}$ and $\boldsymbol{S_a}$ are the measurement and *a priori* error covariance matrix, representing the covariance of the measurement error at different observational channels and of the state vectors at different vertical levels, respectively. The diagonal elements of $\boldsymbol{S_e}$ and $\boldsymbol{S_a}$ are the variance of the errors and the off-diagonal elements are the inter-channel or inter-layer covariance of the errors. Considering that the covariance of the AERI measurement errors are relatively small (Turner & Blumberg, 2018), the off-diagonal elements of $\boldsymbol{S_{e,AERI}}$ are set to be 0. The square root of the diagonal components of $\boldsymbol{S_{e,AERI}}$ and $\boldsymbol{S_{e,HiSRAMS}}$ are shown in Figure 4.15. AERI radiance has a relatively smaller measurement uncertainty in the window band (800 – 1200 cm^{-1}), although it translates to large brightness temperature uncertainty because the radiance signal in this band is typically small, especially in the clear-sky condition.

The *a priori* dataset consists of the hourly-mean temperature and water vapor concentration profiles from the fifth generation European Centre for Medium-Range Weather

Forecasts atmospheric reanalysis dataset, ERA5 (Hersbach et al., 2020). The hourly-mean profiles in Februaries from 1944 to 2022 at 9 grid boxes centered around the Ottawa International Airport (latitude: 45.32°, longitude: -75.66°) were collected to capture the temporal and spatial variability of the atmospheric state variables. The vertical coordinate we adopted in this study is altitude. Thus, both ERA5 hourly-mean surface level and pressure level (37 levels) data are utilized to form the *a priori* dataset, which has 38 vertical levels in total (shown in Figure 4.16). The thickness of the layers is 1.26 km on average, with the lowermost few layers being centered at 0.13, 0.24, 0.44, 0.64, 0.85, 1.07, 1.29, and 1.51 km, respectively. The reason that we did not use higher vertical resolution for the *a priori* is that the vertical resolution of the retrieval is already limited by the Jacobian matrix and the measurement error covariance matrix (details in the following analysis). The covariance matrix $\boldsymbol{S_a}$ used in this study is shown in Figure 4.17 and the correlation matrix $\boldsymbol{C_a}$, which represents the correlation coefficient in the *a priori* dataset, is shown in Figure 4.18. The first guess of the state vector, $\boldsymbol{x_1}$, is the mean profile of all the hourly-mean profiles in the *a priori* dataset.

Ideally, the Jacobian matrix should be updated at every iteration step. However, the calculation of the Jacobian matrix is the most computationally expensive step in the retrieval. Owing to the relatively smaller change of the atmospheric state vectors after iteration step 2, which results in a relatively smaller change of the Jacobian matrix, we set the AERI Jacobian matrix for all the following iteration steps to that from step 2, $\boldsymbol{K_{AERI,2}}$. The calculation of the $\boldsymbol{K_{HiSRAMS}}$ is fast so it is updated in every iteration step. The AERI analytical Jacobian in high spectral resolution was obtained first and then it was convolved with the AERI scan function to match AERI channels. The product of the Jacobians and the standard deviation of the state variables at selected levels for AERI and HiSRAMS are illustrated in Figure 4.19, Figure 4.20, and Figure 4.21.

In Equation 4.3, we use a regularization parameter, $\boldsymbol{\gamma}$, to weigh the measurement and *a priori* according to their error magnitudes. It is set to be a large value at the first step, decreasing with iterations until the convergence criterion (described below) is met. A set of sensitivity tests was performed to find the appropriate initial value of $\boldsymbol{\gamma}$ and how it should change with iterations. The final setting of the initial value of $\boldsymbol{\gamma}$ is 10000. For each iteration, if the cost function $\boldsymbol{J}$ shown in Equation 4.4 is increasing, $\boldsymbol{\gamma}$ is increased by 10 times and the state vector is updated based on the new $\boldsymbol{\gamma}$ until $\boldsymbol{J}$ is smaller than that for the previous step. While $\boldsymbol{J}$ is decreasing and $\boldsymbol{\gamma}$ is larger than 1, $\boldsymbol{\gamma}$ is decreased by 10 times for the next iteration step.

$$\boldsymbol{J} = \left(\boldsymbol{x_j} - \boldsymbol{x_a}\right)^{\boldsymbol{T}} \boldsymbol{S_a}^{-1}\left(\boldsymbol{x_j} - \boldsymbol{x_a}\right) + \left[\boldsymbol{y} - \boldsymbol{F}\left(\boldsymbol{x_j}\right)\right]^{\boldsymbol{T}} \boldsymbol{S_e}^{-\boldsymbol{1}}\left[\boldsymbol{y} - \boldsymbol{F}\left(\boldsymbol{x_j}\right)\right] \tag{4.4}$$

The information content of the retrievals finds common usage in assessing the retrievability of the atmospheric state variables. The averaging kernel matrix, $\boldsymbol{A}$, defined as the derivative of the estimated state vectors to the true state vectors, can be derived based on $\boldsymbol{K}$, $\boldsymbol{S_e}$ and $\boldsymbol{S_a}$, shown in Equation 4.5. The Degrees of Freedom for Signal (DFS), which is the trace of the averaging kernel matrix, are adopted to quantify the information content of the retrievals (Equation 4.6). A higher value of DFS means that more information content can be retrieved. The DFS for each retrieved vertical level tells us how many pieces of independent information we can get for this specific level. Ideally, for each vertical level, the DFS equals to 1. Yet due to various limiting factors, including the measurement errors and the covariance between different levels, the DFS is normally below 1.

$$\boldsymbol{A} = \left(\boldsymbol{K_j}^{\boldsymbol{T}} \boldsymbol{S_e}^{-1} \boldsymbol{K_j} + \boldsymbol{S_a}^{-1}\right)^{-1} \boldsymbol{K_j}^{\boldsymbol{T}} \boldsymbol{S_e}^{-1} \boldsymbol{K_j} \tag{4.5}$$

$$\boldsymbol{DFS} = \boldsymbol{trace}(\boldsymbol{A}) \tag{4.6}$$

Another relevant measure of the retrieval performance is the retrieval uncertainty. The posterior error covariance matrix, $\boldsymbol{S}$, is defined in Equation 4.7. The square root of the diagonal elements of $\boldsymbol{S}$ provides the $\boldsymbol{1\sigma}$ uncertainty in the retrieved atmospheric state variables. Both $\boldsymbol{A}$ and $\boldsymbol{S}$ are iterated over the steps and are impacted by the value of $\boldsymbol{\gamma}$. In order to have fair comparison between different retrieval cases, the final values of $\boldsymbol{A}$ and $\boldsymbol{S}$ are determined when $\boldsymbol{\gamma}$ is 0.

$$\boldsymbol{S} = \left(\boldsymbol{K_j}^{\boldsymbol{T}}\boldsymbol{S_e}^{-\boldsymbol{1}}\boldsymbol{K_j} + \boldsymbol{S_a}^{-\boldsymbol{1}}\right)^{-\boldsymbol{1}} \tag{4.7}$$

For all these matrices, the dimensions are only based on the dimension of the vertical level ($\boldsymbol{n_{level}}$) and the dimension of the instrumental channels ($\boldsymbol{n_{AERI}}$ and $\boldsymbol{n_{HiSRAMS}}$). In this study, we retrieve temperature and water vapor vertical profiles simultaneously. Thus, $\boldsymbol{x}$ equals to $\begin{bmatrix}\boldsymbol{x_T}\\ \boldsymbol{x_q}\end{bmatrix}$ with a dimension of $\boldsymbol{38} \times \boldsymbol{2} = \boldsymbol{76}$. Because HiSRAMS is an airborne instrument, the light path of the HiSRAMS may be limited by the observational altitude when pointing directly downward (nadir-pointing). Thus, $\boldsymbol{n_{level}}$ varies for different case studies (detailed in the following sections). In order to test the full potential of AERI and HiSRAMS to retrieve temperature and water vapor concentration profiles, all the instrumental channels are kept, resulting $\boldsymbol{n_{AERI}} = \boldsymbol{2490}$ and $\boldsymbol{n_{HiSRAMS}} = \boldsymbol{2850}$ (including the measurements of both spectrometers of HiSRAMS).

The retrieval is considered to be converged when the convergence criteria, shown in Equation 4.8 are met:

$$\boldsymbol{d_{x,j}}^{\boldsymbol{2}} = \left(\boldsymbol{x_j} - \boldsymbol{x_{j+1}}\right)^{\boldsymbol{T}}\left(\boldsymbol{K_j}^{\boldsymbol{T}}\boldsymbol{S_e}^{-\boldsymbol{1}}\boldsymbol{K_j} + \boldsymbol{S_a}^{-\boldsymbol{1}}\right)\left(\boldsymbol{x_j} - \boldsymbol{x_{j+1}}\right) < \mathbf{min}\left\{\boldsymbol{d_{threshold}}^{\boldsymbol{2}}, \frac{\boldsymbol{n_{level}}}{\boldsymbol{20}}\right\} \tag{4.8}$$

Where $\boldsymbol{d_{x,j}}^{\mathbf{2}}$ represents the change of uncertainty in state vector space. The threshold of this parameter, $\boldsymbol{d_{threshold}}^{\mathbf{2}}$, is determined when the temperature change between two iteration steps equals 0.5 K ($\boldsymbol{\Delta x_T = 0.5\ K}$), the water vapor concentration change between two iteration steps equals a 10 % change in water vapor concentration [$\boldsymbol{\Delta x_q = \log(1.1)}$]. These values represent the expected accuracy of the variables. Note that $\boldsymbol{d_{threshold}}^{\mathbf{2}}$ varies with each iteration due to updates in the Jacobian matrix.

To assess the sensitivity of the measurements while accounting for the state vector variability and the measurement uncertainty together, we derived a metric, the Signal-to-Noise Ratio (SNR) as defined in Equation 4.9, where $\boldsymbol{\sigma(x)}$ represents the standard deviation of the state vector in the *a priori* dataset. Based on their SNR values, we can have a fair comparison between different measurements, i.e., AERI and HiSRAMS in this study.

$$\boldsymbol{SNR} = \frac{\boldsymbol{K\sigma(x)}}{\sqrt{\boldsymbol{S_{e,diag}}}} \tag{4.9}$$

In this study, we obtained temperature and water vapor retrievals based on single instruments (AERI or HiSRAMS) and joint instruments (AERI and HiSRAMS), respectively. Regardless of the retrieval cases, the dimensions of $\boldsymbol{S_a}$, $\boldsymbol{S}$, and $\boldsymbol{A}$ are all $\boldsymbol{n_{level}} \times \boldsymbol{n_{level}}$. $\boldsymbol{S_a}$, $\boldsymbol{S}$, and $\boldsymbol{A}$ all have a similar matrix structure: the upper-left sub-matrix and the lower-right sub-matrix are for temperature and water vapor respectively. As a result, we can separate the information of temperature and water vapor. When retrieving the temperature and water vapor vertical profiles using either AERI or HiSRAMS alone, the dimension of $\boldsymbol{S_e}$ and $\boldsymbol{K}$ are $\boldsymbol{n_{instrument}} \times \boldsymbol{n_{instrument}}$ and $\boldsymbol{n_{instrument}} \times \boldsymbol{n_{level}}$, respectively, where ‘instrument’ refers to either AERI or HiSRAMS. For joint retrieval:

$$\boldsymbol{y}_{joint} = \begin{bmatrix} \boldsymbol{y}_{AERI} \\ \boldsymbol{y}_{HiSRAMS} \end{bmatrix} \tag{4.10}$$

$$\boldsymbol{S}_{e,joint} = \begin{bmatrix} \boldsymbol{S}_{e,AERI} & \boldsymbol{0} \\ \boldsymbol{0} & \boldsymbol{S}_{e,\,HiSRAMS} \end{bmatrix} \tag{4.11}$$

$$\boldsymbol{K}_{joint} = \begin{bmatrix} \boldsymbol{K}_{AERI} \\ \boldsymbol{K}_{HiSRAMS} \end{bmatrix} \tag{4.12}$$

The dimensions of $\boldsymbol{y}_{joint}$, $\boldsymbol{S}_{e,joint}$, and $\boldsymbol{K}_{joint}$ are $(\boldsymbol{n}_{AERI} + \boldsymbol{n}_{HiSRAMS}) \times \boldsymbol{1}$, $(\boldsymbol{n}_{AERI} + \boldsymbol{n}_{HiSRAMS}) \times (\boldsymbol{n}_{AERI} + \boldsymbol{n}_{HiSRAMS})$, and $(\boldsymbol{n}_{AERI} + \boldsymbol{n}_{HiSRAMS}) \times \boldsymbol{n}_{level}$ respectively.

4.4 Ground-based HiSRAMS and AERI retrievals

Ground measurements of AERI and HiSRAMS were obtained in campaign FC2023. Simultaneous temperature and water vapor retrievals were performed for single instruments (AERI or HiSRAMS) to compare their retrieval performance. For ground-based retrievals, the number of the vertical levels is 38. Thus, n_{level} is 76.

4.4.1 Temperature retrieval

The total DFS corresponding to temperature retrievals across the entire atmospheric column are quantified to be 9.52 and 5.27 for AERI and HiSRAMS, respectively. Notably, AERI exhibits a higher information content in temperature when compared to HiSRAMS. To further elucidate the distribution of information content, the Cumulative Degrees of Freedom for Signal (CDFS) for temperature, defined as the vertical summation of DFS values from the surface up to the target altitude, is shown in Figure 4.1a. The results indicate a greater concentration of information content in the lowermost atmospheric layers for both AERI and HiSRAMS. Furthermore, most of the information content in temperature resides within the tropospheric region, specifically below 8 km, exhibiting DFS values of 6.14 and 3.41 for AERI and HiSRAMS, respectively.

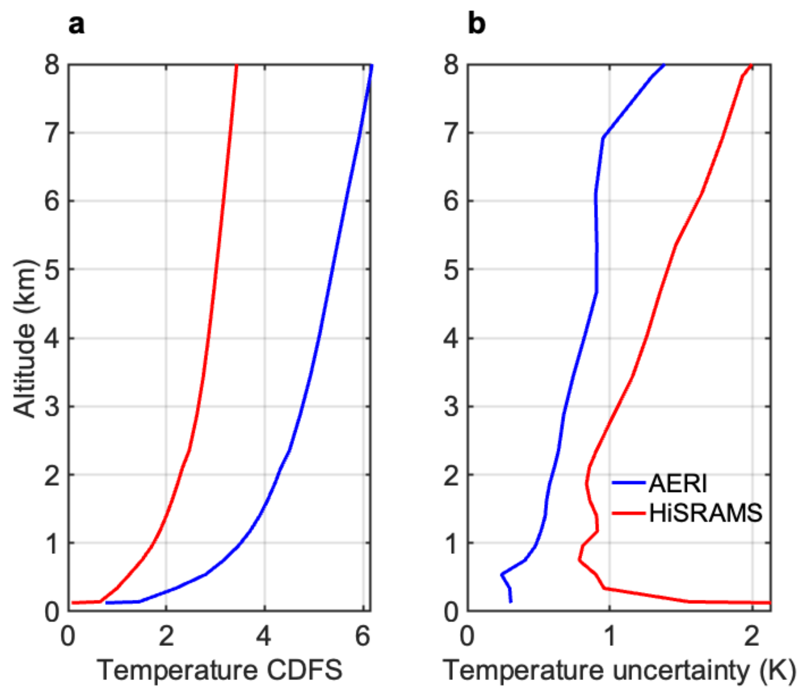

Figure 4.1: Information content and retrieval uncertainty in temperature based on single ground measurements. (a) Cumulative Degrees of Freedom of Signal (CDFS) for temperature. (b) Uncertainty in the retrieved temperature.

The uncertainty associated with temperature retrievals varies between AERI and HiSRAMS. In AERI retrieval, the temperature uncertainty demonstrates an overall increase with altitude. In contrast, the temperature uncertainty in HiSRAMS retrieval decreases with altitude within the few initial levels near the surface. The interplay between the *a priori* uncertainty and the measurement uncertainty, the two terms in Equation 4.7 that determine the posterior error covariance matrix, govern the retrieval accuracy. Within the troposphere, the *a priori* uncertainty typically decreases with altitude, thereby contributing to the overall reduction in retrieval uncertainty. The sensitivity of AERI measurements to temperature tends to decrease with altitude (Figure 4.19), leading to an increase in retrieval uncertainty with height (Figure 4.1a). At higher altitudes, this measurement uncertainty exceeds the *a priori* uncertainty. However, in the case of

HiSRAMS measurements, the sensitivity to temperature does not show a monotonic decrease with altitude across certain channels, as shown in Figure 4.20a and Figure 4.20b. This particular behavior results in maximum retrieval uncertainty within the lowermost atmospheric layers (Figure 4.1b). It is pertinent to note that the behavior of the sensitivity of the HiSRAMS measurements discussed above is influenced by variations in the thickness of vertical layers.

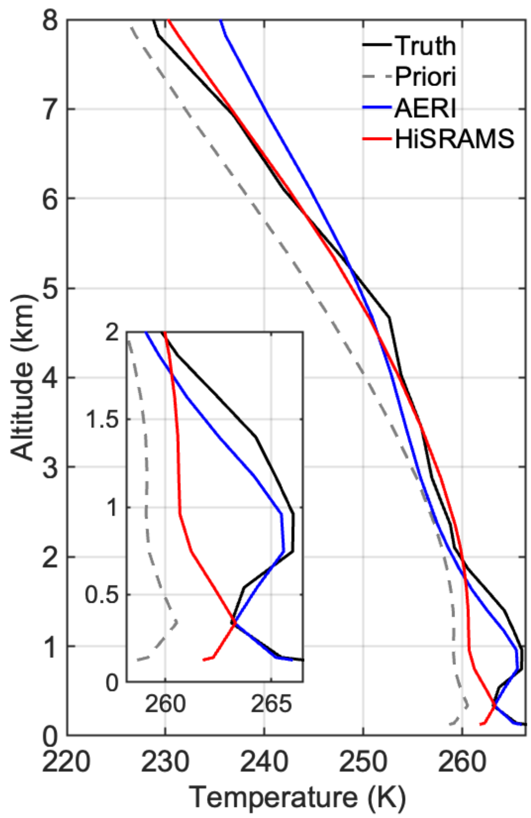

Figure 4.2: Comparison between retrieved temperature profiles based on AERI or HiSRAMS ground measurement and the truth from radiosonde measurements.

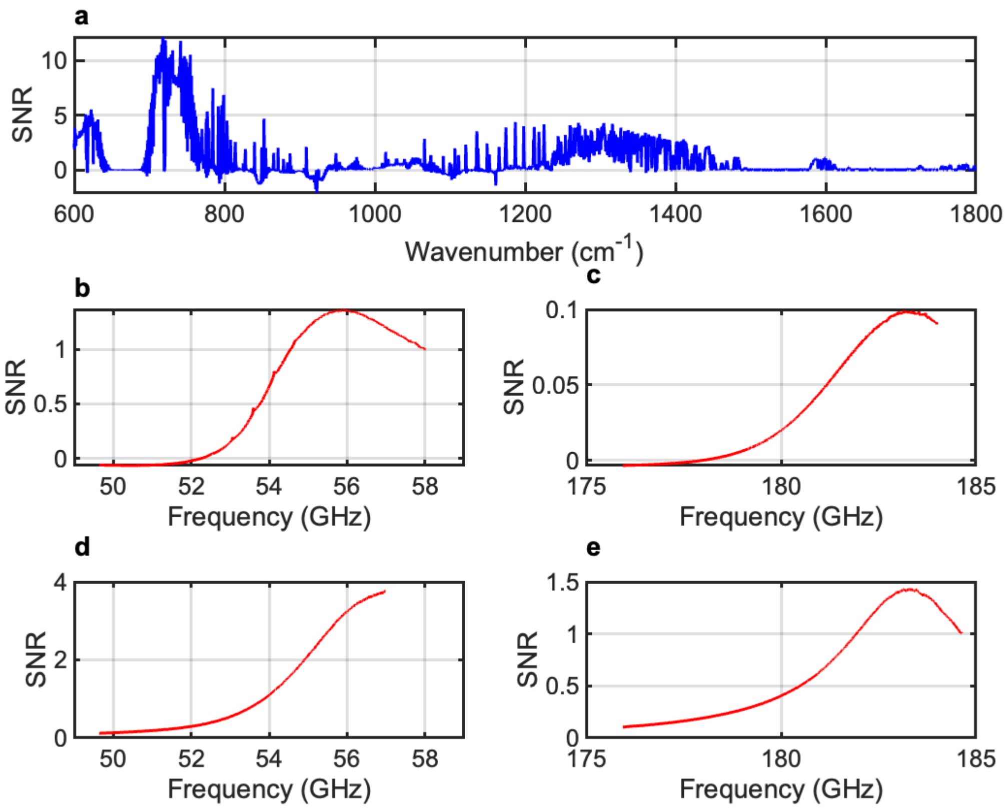

Figure 4.3: Signal-to-Noise Ratio (SNR) for temperature. (a) SNR for AERI zenith-pointing measurements at 0.75 km (level 5). (b) SNR for HiSRAMS zenith-pointing measurements in the oxygen band at 0.75 km (level 5). (c) SNR for HiSRAMS zenith-pointing measurements in the water vapor band at 0.75 km (level 5). (d) SNR for HiSRAMS nadir-pointing measurements in the oxygen band at 6.1 km (level 18). (e) SNR for HiSRAMS nadir-pointing measurements in the water vapor band at 6.1 km (level 18). Units: 1.

The validation of retrieved temperature profiles is based on ground-truth data from radiosonde measurements, represented by the black line in Figure 4.2. A temperature inversion at ~550 m, with a depth of approximately 400 m, presented a valuable test to assess the resolvability of such signals in temperature retrieval. The subset displayed in Figure 4.2 specifically focuses on the profiles below 2 km. The *a priori* profile shows a near-surface temperature inversion (grey dashed line in Figure 4.2), which is different from the truth observed by the radiosonde. The AERI-retrieved temperature profile (blue line in Figure 4.2) effectively captures the sub-kilometer temperature inversion in the layer of 300-700 m together with an accurate representation of the near-surface temperatures below 300 m. In contrast, HiSRAMS cannot capture the detailed vertical temperature structures below 2 km. The shape of the HiSRAMS-retrieved temperature profile (red line in Figure 4.2) closely mirrors that of the *a priori* profile. This discrepancy in the near-surface temperature feature retrievability between the two instruments can be attributed to AERI's higher SNR for temperature near the surface when compared to HiSRAMS, as demonstrated in Figure 4.3a, Figure 4.3b, and Figure 4.3c. In the upper troposphere, both AERI- and HiSRAMS-retrieved temperature profiles align well with the truth data. However, it is noted that AERI exhibits a more pronounced temperature retrieval bias above 6 km.

In summary, in this clear-sky ground-deployment case, it is evident that AERI outperforms HiSRAMS in terms of the retrievability of temperature profiles, showcasing superior performance across key metrics, including information content, retrieval uncertainty, and retrieval accuracy.

4.4.2 Water vapor retrieval

The retrieval of atmospheric water vapor concentration using AERI and HiSRAMS ground measurements provides valuable insights. AERI records a total DFS of 4.22, whereas HiSRAMS reports 3.03, indicating that the two instruments offer comparable information regarding water vapor. However, at an altitude of 8 km, AERI reaches its maximum CDFS, while the CDFS for HiSRAMS continues to increase with altitude, suggesting that, despite its lower total water vapor DFS compared to AERI, HiSRAMS captures water vapor information over a broader vertical range.

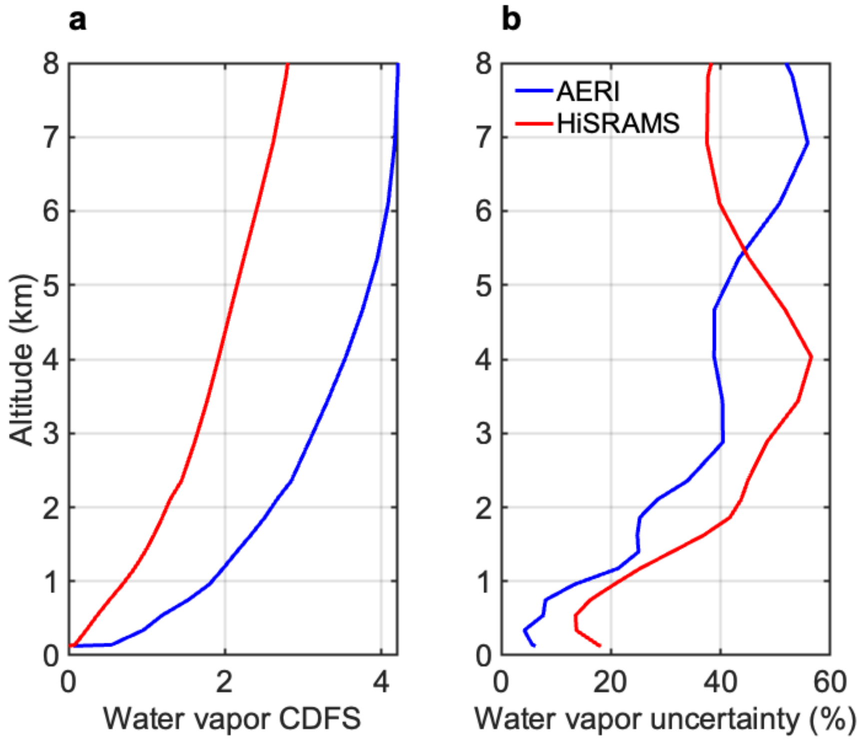

Figure 4.4: Information content and uncertainty in water vapor retrieval from single ground-based measurements: (a) Cumulative Degrees of Freedom of Signal (CDFS) for water vapor, (b) Uncertainty in retrieved water vapor concentration.

Moreover, the uncertainty associated with retrieved water vapor concentration from AERI increases with altitude. In contrast, the uncertainty in HiSRAMS-retrieved water vapor concentration reaches a maximum of approximately 4 km. Notably, at altitudes below 5.5 km, AERI-retrieved water vapor exhibits lower uncertainties compared to HiSRAMS-retrieved water vapor, while the converse is observed at altitudes above 5.5 km.

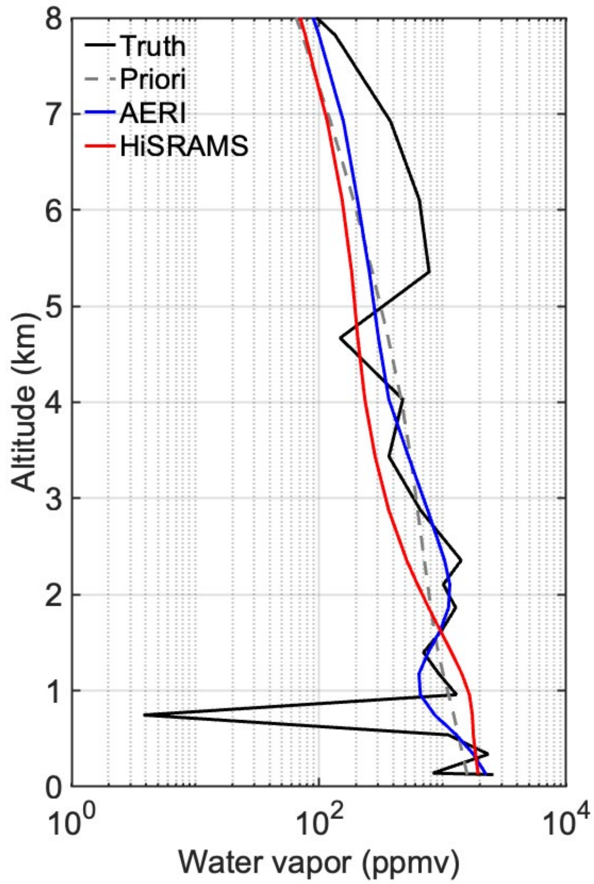

Figure 4.5: Comparing retrieved water vapor concentration profiles from ground-based AERI and HiSRAMS measurements with radiosonde-derived truth.

The water vapor concentration derived from radiosonde measurements (black line in Figure 4.5) reveals local minima and maxima, particularly a distinctive dry layer at approximately 750 m, with a depth of ~400 m. However, neither AERI nor HiSRAMS can fully capture this fine-scale, half-kilometer deep dry anomaly near the surface. The water vapor concentration profile retrieved by AERI (blue line in Figure 4.5) exhibits a closer alignment with the radiosonde-derived truth, in contrast to the profile retrieved by HiSRAMS (red line in Figure 4.5). Furthermore, the AERI-retrieved water vapor concentration profile suggests the presence of a moist anomaly at an altitude of about 2 km, which is consistent with the radiosonde measurements. This finding, along with the resolvability of the temperature inversion shown above, encourages further investigation of the instruments' capacity to capture fine-scale thermodynamic variability in the lower atmosphere.

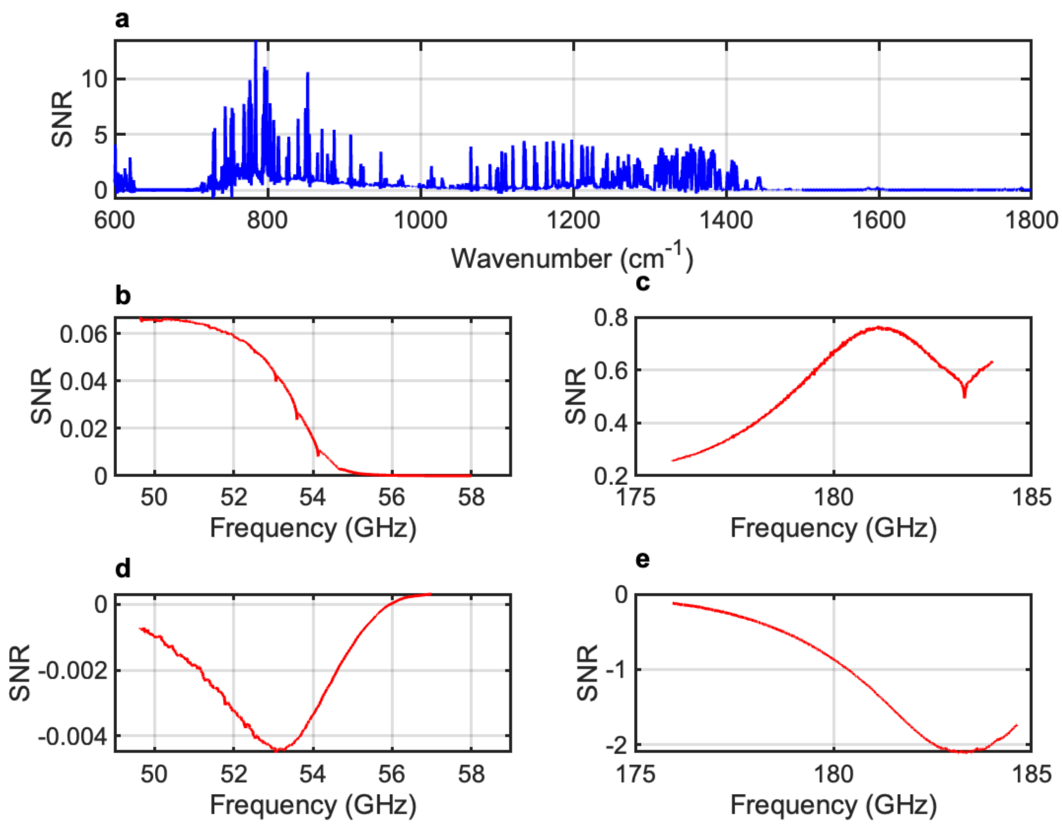

Figure 4.6: Same as Figure 4.4 but for water vapor. Unit: 1. The presence of negative SNR values results from negative values in $\boldsymbol{K}$.

Generally, AERI outperforms HiSRAMS in water vapor retrieval, primarily due to the greater number of AERI channels with relatively higher SNR, as evident in Figure 4.6a, Figure 4.6b, and Figure 4.6c. The higher SNR in AERI measurements makes it more feasible to retrieve precise water vapor concentrations, particularly under challenging atmospheric conditions. However, both AERI and HiSRAMS exhibit lower water vapor retrievability than temperature retrievability, particularly in terms of information content and the ability to resolve confined sub-kilometer features.

4.4.3 Sub-kilometer feature resolvability

Fortunately, in this specific case, both the temperature and water vapor vertical profiles exhibited sub-kilometer features, offering a valuable opportunity to assess the vertical resolvability of temperature and water vapor utilizing ground-based AERI and HiSRAMS measurements. A temperature inversion, with an altitude of approximately 550 m and a depth of 400 m, and a sudden dry layer at around 750 m with a depth of 400 m, were clearly discernible.

To understand the performance of the two instruments, we employ the averaging kernel matrix to determine the vertical resolution of the retrieved profiles. Each row in the matrix defines the averaging kernel for a specific level within the retrieved profile. Each row of an ideal $\boldsymbol{A}$ would look like a delta-function, indicating that the retrieved quantity at the vertical level exclusively represents the condition at that particular vertical location, i.e., exhibiting the highest attainable vertical resolution. However, due to correlations between different atmospheric layers, the vertical resolution of the retrieved profiles is constrained. Typically, each row of $\boldsymbol{A}$ reaches its peak at the retrieval level; this indicates that the bulk of information at that particular level is derived from that level, although smaller but non-negligible contributions are obtained from neighboring levels. Hence, we use the full width at half maximum (FWHM) of every row of $\boldsymbol{A}$ to quantify and represent the vertical resolution of the retrieval.

To demonstrate the concept, we show the rows of $\boldsymbol{A}$ corresponding to altitudes of 550 m and 750 m, where the sub-kilometer temperature and water vapor concentration features are situated. For example, the blue line in Figure 4.7a shows the row of $\boldsymbol{A}$ for AERI temperature retrieval at an altitude of 550 m. This row of $\boldsymbol{A}$ peaks at the selected altitude, decreasing rapidly on either side of the peak. AERI temperature retrieval at 550 m displays a FWHM of approximately 403 m, indicating its vertical resolution. In contrast, HiSRAMS temperature retrieval at the same altitude offers a coarser vertical resolution of 869 m. The temperature inversion depth, roughly 400 m, closely aligns with AERI's vertical resolution but is shallower than that of HiSRAMS. This difference elucidates why the AERI retrieval has the capability of resolving the temperature inversion, while the HiSRAMS retrieval cannot.

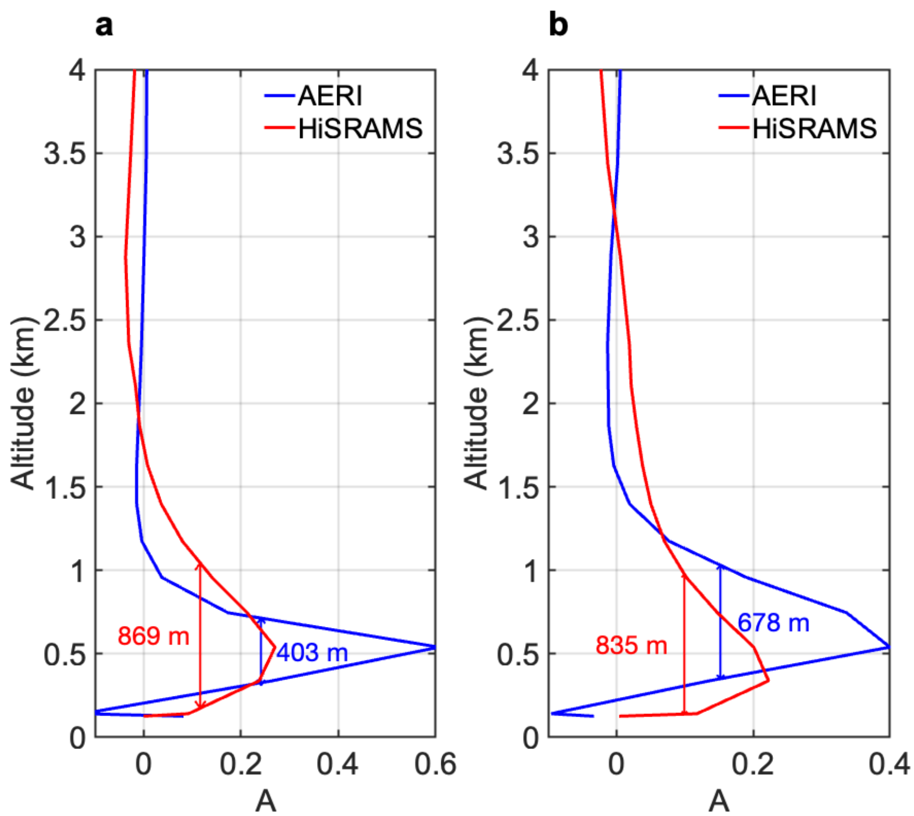

Figure 4.7: Comparing vertical resolution of retrieved (a) temperature and (b) water vapor concentration profiles from ground-based AERI (blue lines) and HiSRAMS (red lines) measurements. This figure displays the averaging kernel matrix row for a vertical level at 550 m for temperature and 750 m for water vapor concentration.

The vertical resolutions of the retrieved water vapor concentrations by AERI and HiSRAMS at 750 m are 678 m and 835 m, respectively. It is evident that neither of the rows in the averaging kernels of AERI nor HiSRAMS exhibit peaks at the target altitude, indicating a stronger correlation in water vapor concentrations between adjacent atmospheric layers. In general, AERI demonstrates higher water vapor vertical resolvability compared to HiSRAMS. However, the vertical resolutions for water vapor concentration at 750 m, as achieved by both AERI and HiSRAMS, exceed the depth of the thin dry layer, rendering them incapable of resolving this layer near the surface.

4.4.4 Retrieval bias and uncertainty comparison

The 3σ retrieval uncertainties (dashed lines in Figure 4.8), obtained from the posterior matrix (Equation 4.7), are compared with the retrieval bias (solid lines in Figure 4.8), which quantifies the difference between the retrieved profile and the truth derived from radiosonde measurements. In general, both the retrieval bias in temperature and water vapor concentration falls within the 3σ retrieval uncertainties, with exceptions at altitudes where fine vertical features exist.

The DFS of temperature and water vapor concentration in the troposphere is similar to previous AERI retrieval and multichannel microwave radiometer retrieval studies (Blumberg et al., 2015; Loveless et al., 2022; Turner & Löhnert, 2021). Blumberg et al. (2015) conducted a comparison of retrieval performance between AERI and a 14-channel ground-based microwave radiometer in clear-sky conditions. Even with a significantly greater number of channels in HiSRAMS compared to the 14-channel radiometer, this study shows comparable retrieval performance between the two microwave radiometers. This implies that, for ground-based retrievals, an increased number of channels in the microwave spectral range may not necessarily improve the retrievals of clear-sky temperature and water vapor concentration.

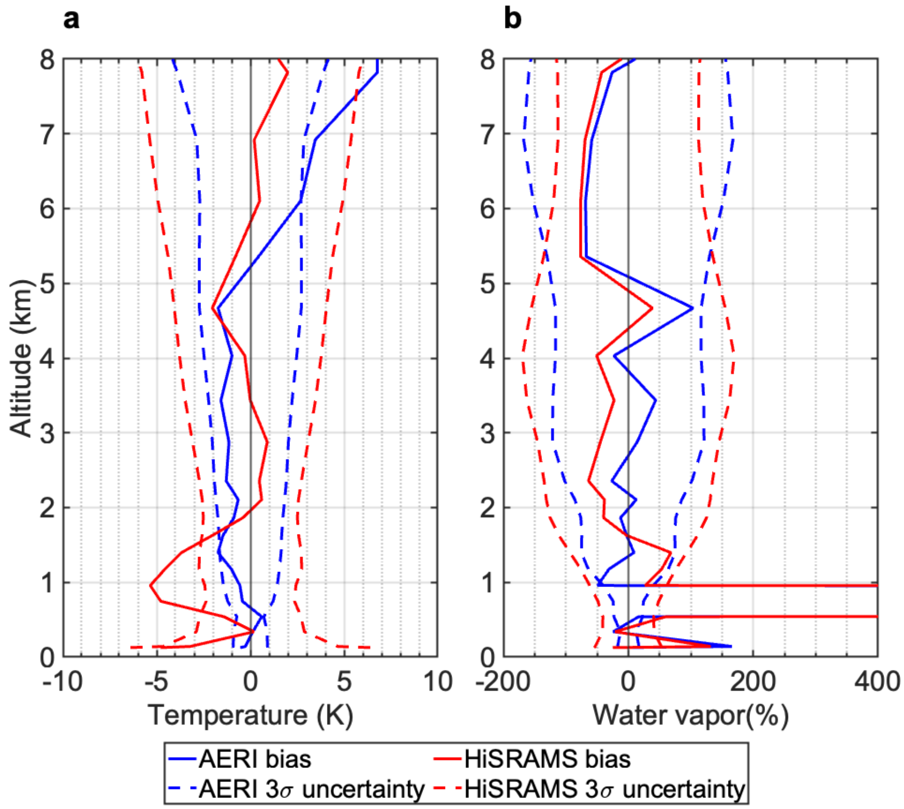

Figure 4.8: Comparison of retrieval bias and uncertainty in ground-based retrievals for (a) temperature and (b) water vapor.

In summary, when retrieving temperature and water vapor concentration profiles from hyperspectral ground measurements under clear-sky conditions, infrared instruments exhibit better performance compared to microwave instruments in terms of information content, retrieval uncertainty, vertical feature resolvability, and retrieval biases. However, it is worth noting that hyperspectral microwave instruments demonstrate less temperature bias and lower water vapor concentration uncertainty in the upper troposphere.

4.5 Joint airborne HiSRAMS and ground-based AERI retrievals

As an airborne instrument, HiSRAMS was used to collect radiance measurements at various altitudes during the FC2023 campaign. To investigate the potential advantages of combining these airborne HiSRAMS measurements with ground-based AERI measurements, we conducted joint retrievals in comparison to independent retrievals. We refer the measurements obtained from this unique setting as “sandwich” measurements. Throughout FC2023, we gathered HiSRAMS nadir-pointing measurements during ten flight legs, covering altitudes from near the surface up to 6.8 km. We specifically selected measurements obtained at 6.8 km for our joint retrievals, as the measurements at this altitude captured a substantial portion of the troposphere viewed by both instruments.

In this section, we compare joint retrievals, which combine the AERI zenith-pointing measurements on the ground and the HiSRAMS nadir-pointing measurements at 6.8 km to retrieve temperature and water vapor concentration vertical profiles, with single retrievals based on either the AERI zenith-pointing measurements on the ground or the HiSRAMS nadir-pointing measurements at 6.8 km alone. In the case of joint retrieval and AERI-only retrieval, n_{level} is set at 76, as ground-based measurements are incorporated into both retrievals. To avoid uncertainties due to land surface emissivity, we adopt an elevated “surface” boundary condition at altitude of 429 m for the HiSRAMS nadir-pointing forward model (Liu et al., 2023). Consequently, for HiSRAMS nadir-pointing retrievals alone, n_{level} is set at 30, considering that there are only 15 levels between 429 m and 6.8 km in the vertical configuration used for these retrievals. Previous work by Liu et al. (2023) has identified biases in nadir-pointing HiSRAMS flight measurements. To ensure the reliability of our retrieval results, we have corrected the HiSRAMS nadir-pointing measurements used in this study, following the method outlined in Section 4.7.

4.5.1 Temperature retrievals

Joint retrieval enhances the temperature information content. The total temperature DFS for the joint retrieval stands at 10.96, surpassing the values obtained in individual retrievals (9.52 for AERI-only retrieval and 3.20 for HiSRAMS-only retrieval). A field campaign carried out by the UK Met Office Airborne Research Interferometer Evaluation System (ARIES) demonstrated a DFS between 4 and 5 for temperature retrievals using airborne nadir-pointing infrared hyperspectral observations between 690 and 775 cm^{-1} at similar observational height to HiSRAMS (Allen et al., 2014). This DFS value is higher than that of HiSRAMS retrieval.

Figure 4.9a shows the detailed DFS values for specific altitude levels. In the case of the HiSRAMS-only nadir-pointing retrieval, the DFS increases with altitude (red line in Figure 4.9a). This increase is attributed to the HiSRAMS measurements acquired at 6.8 km, making it more responsive to atmospheric conditions near the instrument. Similarly, for the AERI-only zenith-pointing retrieval, the DFS decreases with altitude (blue line in Figure 4.9a). Notably, the DFS for the joint retrieval (green line in Figure 4.9a) exceeds that of either individually, signifying the increased information content, particularly in the upper troposphere, where AERI's capabilities are limited.

Joint retrieval not only enhances the information content but also diminishes retrieval uncertainty. The temperature uncertainty in AERI or HiSRAMS single-instrument retrievals increases and decreases with altitude respectively. By combining both sets of measurements, the overall uncertainty in temperature diminishes, compared to that in either of the individual retrievals. Consequently, temperature uncertainties below 6 km consistently remain within 1 K.

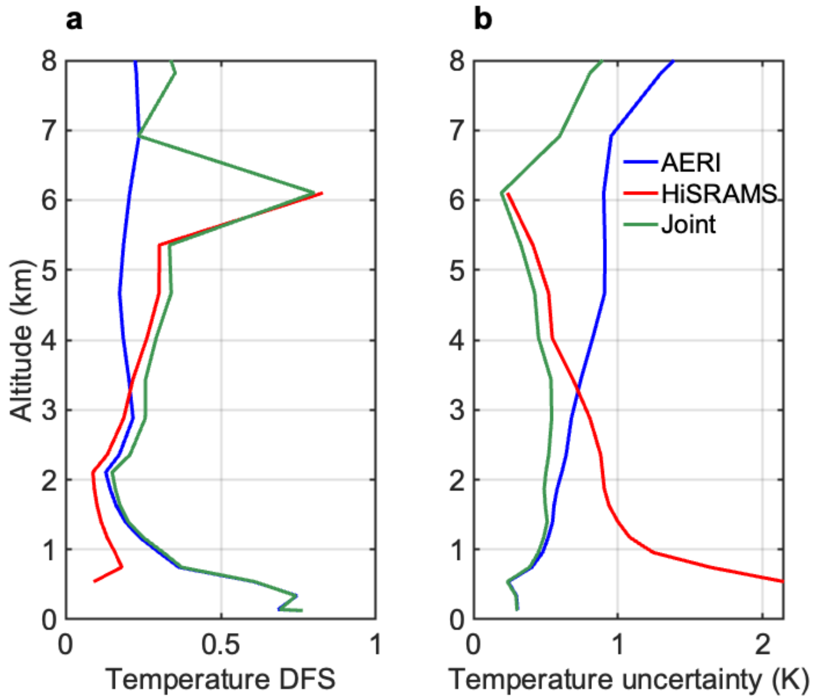

Figure 4.9: Comparison of information content and temperature retrieval uncertainty between joint airborne HiSRAMS and ground-based AERI retrievals versus single-instrument retrievals from either airborne HiSRAMS or ground-based AERI. (a) Temperature Degrees of Freedom for Signal (DFS). (b) Uncertainty in retrieved temperature.

Figure 4.10a shows the temperature profiles retrieved from actual measurements. As with the ground-based HiSRAMS retrieval results, the HiSRAMS-only nadir-pointing retrieval (red line in Figure 4.10a) remains incapable of resolving the fine vertical temperature features near the surface. This limitation arises from a lower SNR (not shown), compared to the zenith-pointing HiSRAMS measurements, in regions where a temperature inversion is present. The smaller SNR results from the measurements being further away from the fine vertical feature. The change in observation locations identifies why the temperature profile retrieved from HiSRAMS-only airborne measurements around 6 km closely approximates the actual values, corroborated by the relatively higher SNR shown in Figure 4.3d.

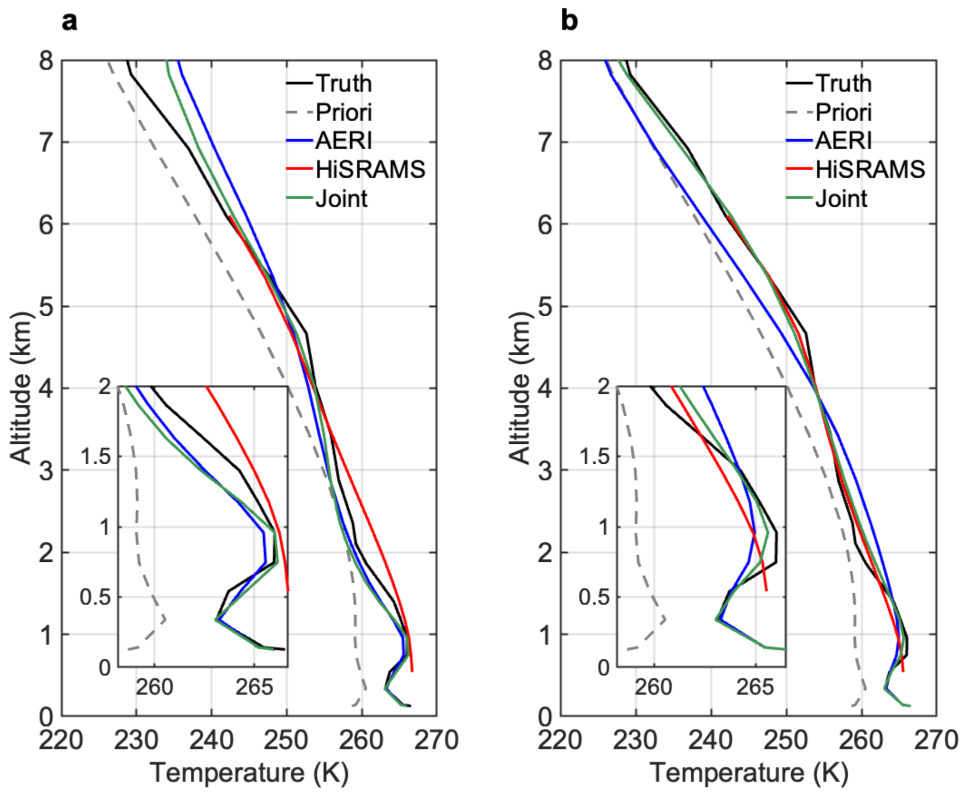

Figure 4.10: Retrieved temperature profiles for joint retrieval (combining AERI zenith-pointing measurements on the ground and HiSRAMS nadir-pointing measurements at 6.8 km) and single-instrument retrievals (utilizing either AERI zenith-pointing measurements on the ground or HiSRAMS nadir-pointing measurements at 6.8 km). (a) Retrieved temperature profiles based on actual measurements. (b) Retrieved temperature profiles based on synthetic measurements.

As discussed in the previous section on ground-based retrieval, the AERI-only retrieval successfully resolves temperature inversions near the surface but exhibits a larger temperature bias in the upper troposphere. Joint retrieval combines the strengths of the two instruments by resolving the fine vertical features near the surface and yielding a reduced temperature bias in the upper troposphere compared to the AERI-only retrieval. Note that a temperature bias still exists above 6 km, even in the case of joint retrieval.

Liu et al. (2023) identified a significant brightness temperature bias in HiSRAMS airborne measurements concerning the brightness temperature truth derived from the HiSRAMS forward model, which utilized radiosonde measurements as inputs. This bias may arise from inaccuracies in either the HiSRAMS measurements or the brightness temperature truth due to imprecise atmospheric state inputs. To assess the limits of the joint retrieval concept, we further conducted joint and single-instrument retrievals based on synthetic measurements. Specifically, radiosonde-derived temperature and water vapor profiles served as inputs for AERI and HiSRAMS forward models to generate synthetic spectra with added random noises appropriate to the measurement uncertainty to emulate the measurements in the retrieval algorithm.

The AERI retrieval based on the synthetic measurement exhibited good resolvability of the temperature inversion near the surface but displayed a larger bias in upper tropospheric temperature (blue line in Figure 4.10b). Simultaneously, the synthetic HiSRAMS retrieval accurately captured temperature profiles well below the observational altitude but could not resolve the near-surface temperature inversion feature (red line in Figure 4.10b). In contrast, the joint synthetic retrieval not only captured the near-surface temperature inversion feature but also effectively constrained the temperature profile both above and below the observational altitude (green line in Figure 4.10b). This underscores the complementary information in the two instruments and a substantial potential of joint retrieval between AERI and HiSRAMS.

4.5.2 Water vapor retrievals

Joint retrieval increases the information content in water vapor concentration. The total water vapor DFS for joint retrieval is 5.82, exceeding that of the water vapor DFS values for either AERI- or HiSRAMS-only retrievals, which are 4.22 and 3.11, respectively. The water vapor DFS for specific levels, illustrated in Figure 4.11a, clearly indicates the enhanced water vapor information content achieved through joint retrieval. Joint retrieval in water vapor particularly excels at the HiSRAMS observation altitude and near-surface, primarily contributed by HiSRAMS and AERI, respectively. Allen et al. (2014) reported a DFS of approximately 3 for the ARIES airborne system at an observational height of 7.4 km with 10 vertical levels, comparable to the HiSRAMS retrieval result. Similarly, higher information content was detected closer to the observational height.

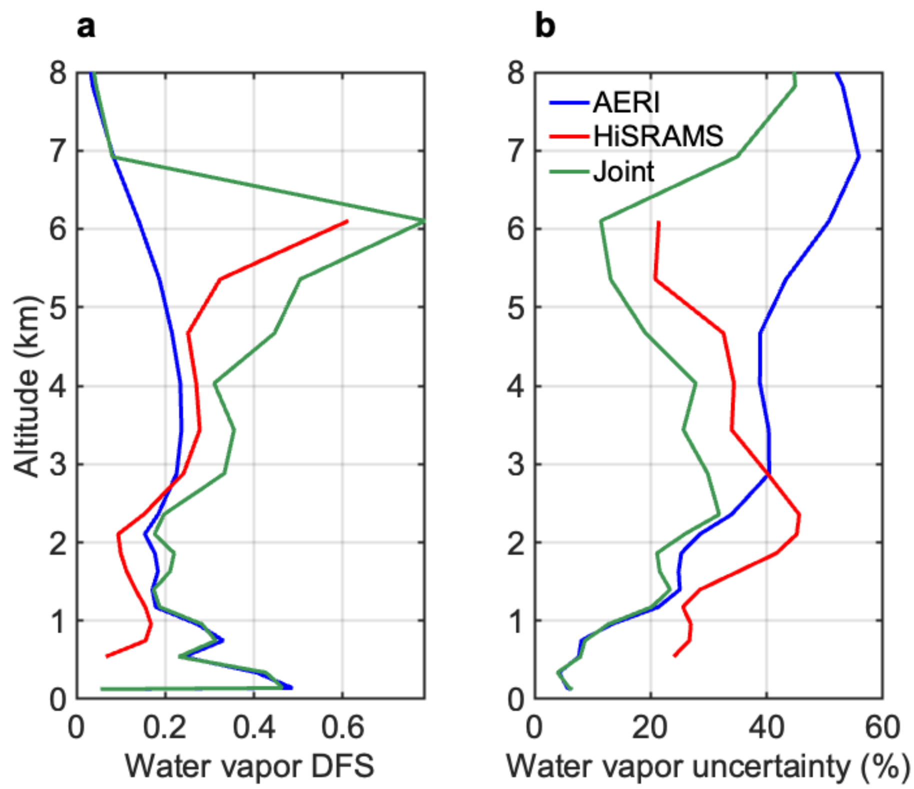

Figure 4.11: Comparison of information content and uncertainty in water vapor retrievals between joint airborne HiSRAMS and ground-based AERI retrievals and single-instrument retrievals from either airborne HiSRAMS or ground-based AERI. (a) Water vapor Degrees of Freedom for Signal (DFS). (b) Uncertainty in retrieved water vapor concentration.

Joint retrievals reduce uncertainties in the retrieved water vapor concentration. As with joint temperature retrievals, uncertainties in retrieved water vapor concentrations from AERI-only measurements generally decrease with altitude. Notably, uncertainties in retrieved water vapor concentration profiles from HiSRAMS-only measurements exhibit a distinct peak around 2 km. Water vapor concentration profiles computed from joint retrievals are characterized by reduced uncertainties at all levels, including those above the HiSRAMS observational altitude.

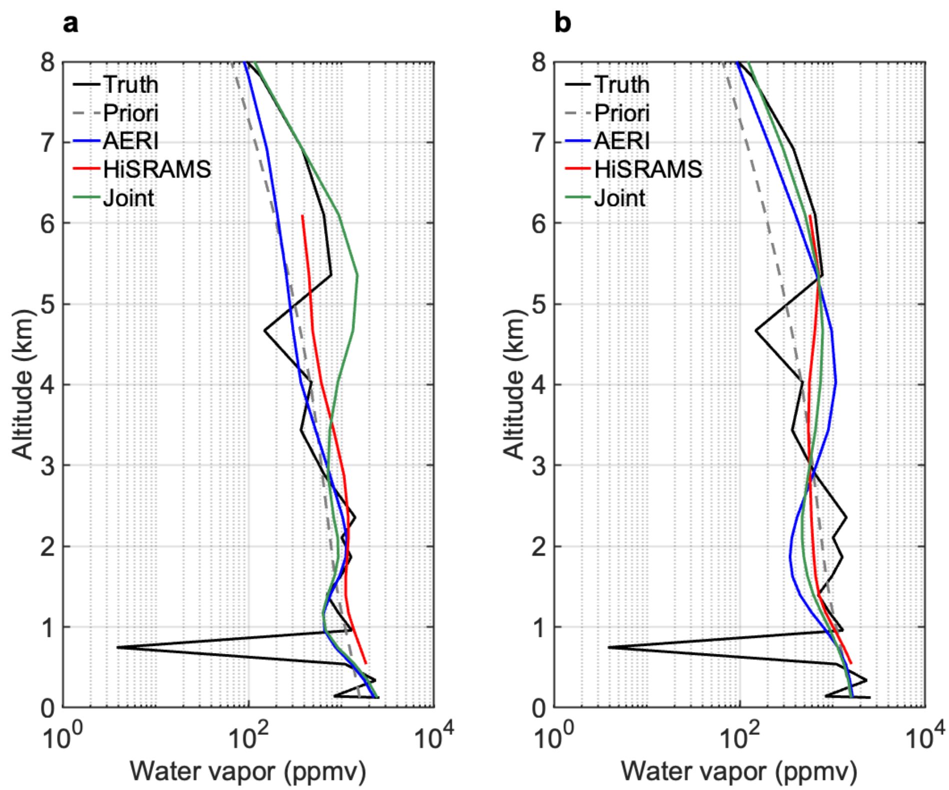

Figure 4.12: Retrieved water vapor concentration profiles for joint retrieval (combining both AERI zenith-pointing measurements on the ground and HiSRAMS nadir-pointing measurements at 6.8 km) and single-instrument retrievals (utilizing either AERI zenith-pointing measurements on the ground or HiSRAMS nadir-pointing measurements at 6.8 km). (a) Retrieved water vapor profiles based on actual measurements. (b) Retrieved water vapor profiles based on synthetic measurements.

Water vapor concentration profiles retrieved from actual measurements are presented in Figure 4.12a. While a HiSRAMS-only retrieval constrains water vapor concentration near the observation altitude due to some channels with the absolute value of SNR larger than 1 (Figure 4.6e), its retrieval capability diminishes further away from it. Joint retrieval in water vapor concentration combines the strengths of both AERI- and HiSRAMS-only retrievals. Nevertheless, constrained by vertical resolution limitations, even joint retrieval falls short of fully capturing fine vertical water vapor features, such as thin dry layers around 750 m and 4.6 km.

The synthetic retrieval results in Figure 4.12b do not exhibit significant improvement in terms of retrieved water vapor concentration bias and the resolution of fine vertical features. This suggests that the accuracy in water vapor retrieval is not severely limited by the accuracy of radiance measurements.

4.5.3 Retrieval bias and uncertainty comparison

Generally, the retrieval bias is within the 3σ retrieval uncertainties for HiSRAMS nadir-pointing flight measurements single-instrument retrieval and joint retrieval (Figure 4.13). Significant retrieval biases exist at altitudes with fine vertical features. The temperature and water vapor retrieval uncertainties decrease with distances away from the observational heights in single instrument retrievals. Joint retrieval shows a bow-shaped posterior uncertainty, signaling its benefits in reducing the retrieval uncertainty. The retrieval bias reported here was analyzed from only one case study, which affords limited error statistics.

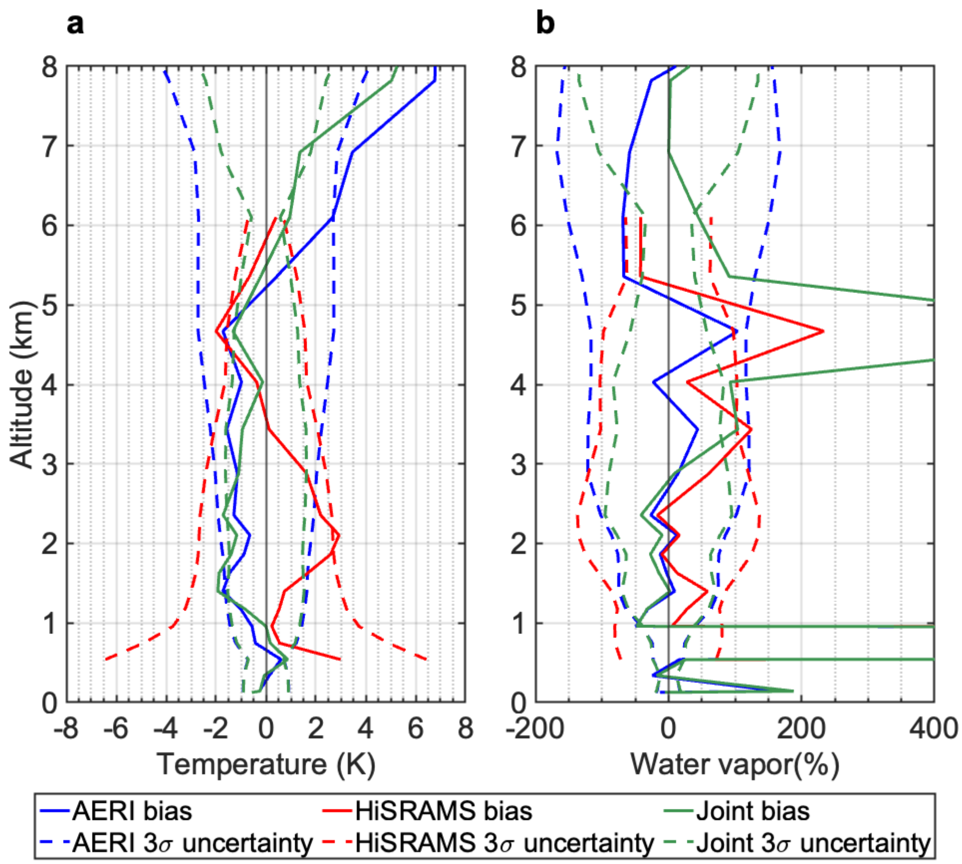

Figure 4.13: Comparison of retrieval bias and uncertainty in joint retrievals: (a) Temperature, (b) Water vapor.

In summary, the synergistic integration of radiative measurements at varying observational altitudes enhances the retrieval performance of thermodynamic variables, with a notable impact on temperature. Previous studies have demonstrated similar improvements, such as the synergy achieved through hyperspectral infrared instruments at different altitudes (e.g., Bani Shahabadi & Huang, 2014; Loveless et al., 2022; Zhao et al., 2022). This study highlights the potential of synergistic retrievals, specifically emphasizing the advantages achieved by combining hyperspectral infrared and microwave radiometers across different altitudes, which may be especially useful for intensive observation campaigns.

4.6 Conclusions and discussion

Hyperspectral radiance measurements afford an advantageous means to monitor the vertical distributions of temperature and water vapor concentration. Leveraging advancements in polyphase spectrometers, a hyperspectral microwave radiometer, featuring a large number of spectral channels comparable to hyperspectral infrared radiometers has been developed. In this study, measurements from an airborne hyperspectral microwave radiometer, HiSRAMS, and a ground-based hyperspectral infrared radiometer, AERI, were acquired on February 11, 2023, to test their retrievals of temperature and water vapor vertical profiles.

We first evaluated the retrieval performance of ground-based AERI measurements against ground-based HiSRAMS measurements. Concerning retrieval uncertainty and information content, AERI demonstrates superior retrieval performance for both temperature and water vapor concentrations compared to HiSRAMS, except in the water vapor retrieval at higher altitudes above 5.5 km. Both AERI and HiSRAMS retrievals exhibit a higher information content for temperature than for water vapor concentrations. The high vertical retrieval resolution of AERI enables the resolution of fine temperature inversion features near the surface, a capability not shared by HiSRAMS temperature retrieval. On the other hand, neither AERI nor HiSRAMS can resolve fine vertical features of water vapor, such as the thin dry layers found near the surface, due to the coarse vertical retrieval resolution of their retrievals. While AERI captures the overall water vapor profile effectively, HiSRAMS demonstrates reduced retrieval performance in this application. These results suggest that, for ground-based measurements, an increase in the number of channels of microwave radiometers does not necessarily make them comparable to infrared hyperspectral radiometers.

We also experimented with a joint retrieval approach involving ground-based zenith-pointing AERI measurements and airborne nadir-pointing HiSRAMS measurements, which we find enhances the performance of temperature and water vapor concentration retrievals compared to single instrument retrievals. Joint retrieval exhibits increased information content and reduced retrieval uncertainty for temperature and water vapor concentrations across all retrieval levels. Ground-based AERI measurements contribute to the resolution of near-surface temperature features, while airborne HiSRAMS measurements exhibit a lower retrieval bias in temperature near the observational altitude (6.8 km). Combining measurements from both instruments yields retrieved temperature profile that captures fine vertical features near the surface while mitigating bias in temperature at the upper troposphere near the HiSRAMS observational altitude. By comparison, the improvement in accuracy in the water vapor concentration retrieval is limited in joint retrieval.

This study is subject to certain limitations. Using the entire spectrum of channels for both instruments in conducting temperature and water vapor retrievals ensures maximum information content employed in the retrievals but is also subject to larger errors and possible interference in certain channels, which can be minimized or eliminated via a channel selection approach in future work. Additionally, the retrieval comparison in this study relies on limited samples from a single campaign, thus bounding the usefulness of the error statistics and comprehensiveness of this assessment. This issue, also relegated to future work, can be addressed with more field observations.

In conclusion, this study utilizes infrared and microwave hyperspectral radiometers to retrieve clear-sky temperature and water vapor concentration profiles under various observational conditions. The retrieval comparison between HiSRAMS and AERI ground-based measurements reveals that infrared hyperspectral observations provide a higher information content and greater vertical resolution for temperature and water vapor retrievals than microwave hyperspectral observations. However, employing zenith-pointing AERI measurements and nadir-pointing HiSRAMS measurements at high altitudes, forming a “sandwich” configuration, not only enhances information content but also reduces retrieval uncertainty and bias in temperature and water vapor concentrations. Integrating ground-based infrared and airborne microwave hyperspectrometers proves advantageous for sounding temperature and water vapor profiles. To thoroughly assess and explore the potential of hyperspectral microwave radiometers in retrieving thermodynamic profiles, further case studies addressing both clear-sky and cloudy-sky temperature and water vapor retrievals are warranted.

4.7 Appendix A: Bias correction for HiSRAMS nadir-pointing measurements at 6.8km

Nadir-pointing HiSRAMS measurements exhibit some brightness temperature biases (Liu et al., 2023), which need to be removed for accurate physical retrieval applications. Given that our focus is solely on nadir-pointing measurements during a specific leg, and we obtain true temperature and water vapor concentration profiles from radiosonde measurements, the brightness temperature bias can be identified based on the differences between HiSRAMS measurements and forward model simulations (blue lines in Figure 4.14).

We partitioned the entire spectrum into distinct spectral ranges, each defined by specific bias features. Within each spectral range, we determined the brightness temperature bias either as a constant or through the application of a linear regression method, as illustrated by the red lines in Figure 4.14. Subsequently, the biases represented by the red lines were systematically removed for all retrieval cases utilizing nadir-pointing HiSRAMS measurements at 6.8 km.

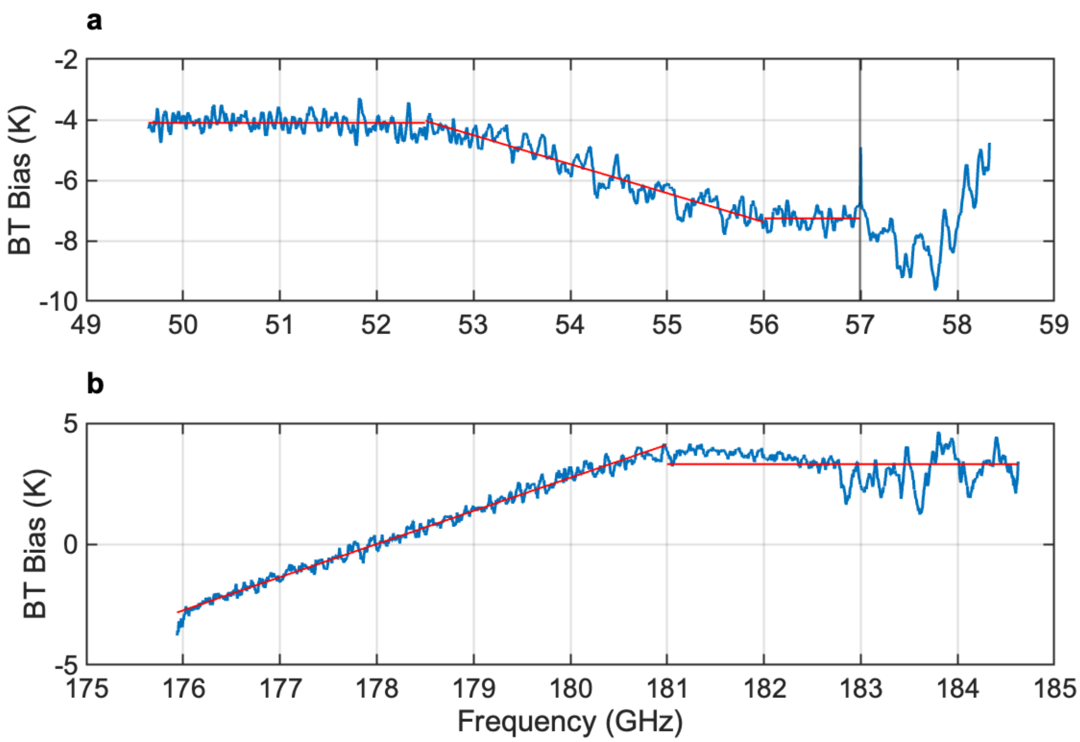

Figure 4.14: Correction of nadir-pointing HiSRAMS measurements bias in (a) oxygen band and (b) water vapor band. The blue lines represent the brightness temperature bias determined by the difference between measurements and forward model simulations (refer to Liu et al., 2023 for detailed methodology). The red lines represent the determined bias.

4.8 Supplement of "Comparative experimental validation of microwave hyperspectral atmospheric soundings in clear-sky conditions"

This supplemental document presents the vertical level adopted and main matrices used in this study, including $\boldsymbol{S_e}$, $\boldsymbol{S_a}$, and $\boldsymbol{K}$ at selected levels.

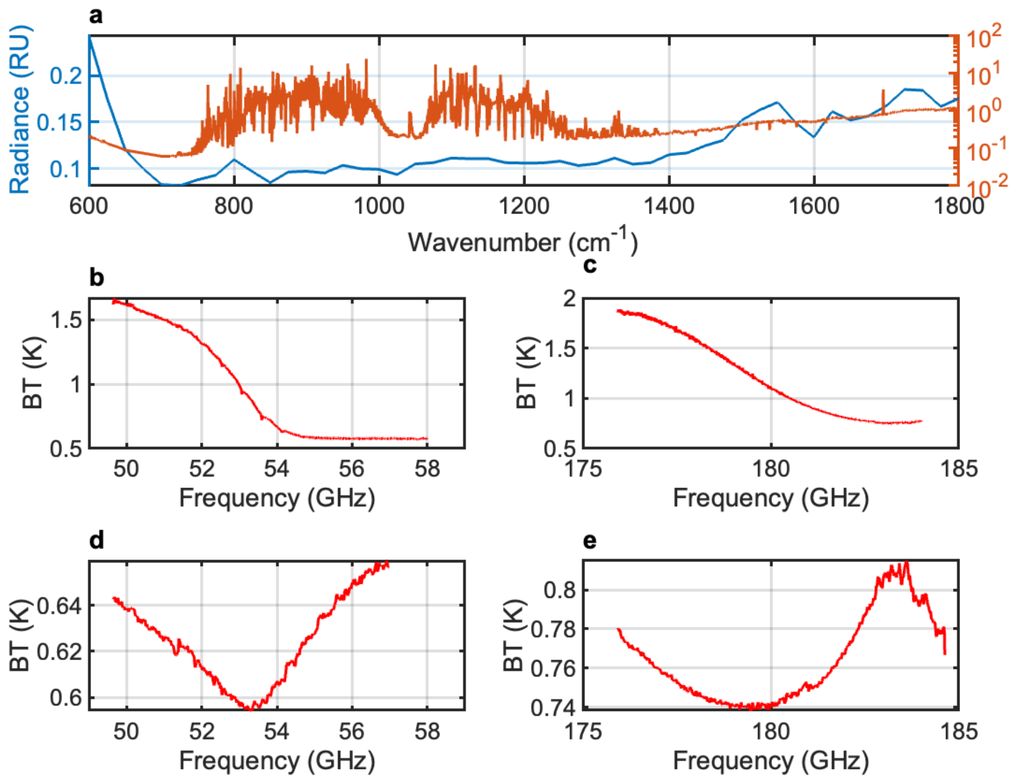

Figure 4.15: The square root of the diagonal components of $\boldsymbol{S_e}$ for AERI measurements (a), HiSRAMS nadir-pointing measurements at 6.8 km in the oxygen band (b) and in the water vapor band (c), and HiSRAMS zenith-pointing measurements at the surface in the oxygen band (d) and in the water vapor band (e).

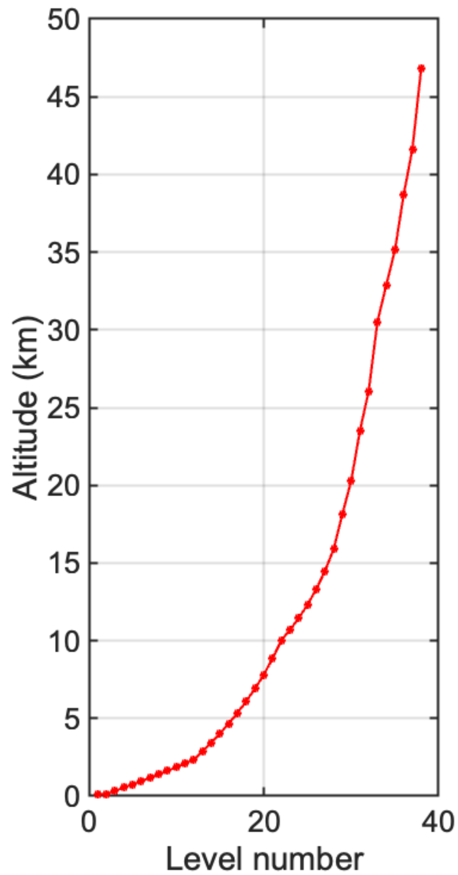

Figure 4.16: The vertical levels adopted in this study for all the retrievals. We utilize altitude coordinates for the retrievals, determined by averaging the geopotential heights from the *a priori* dataset.

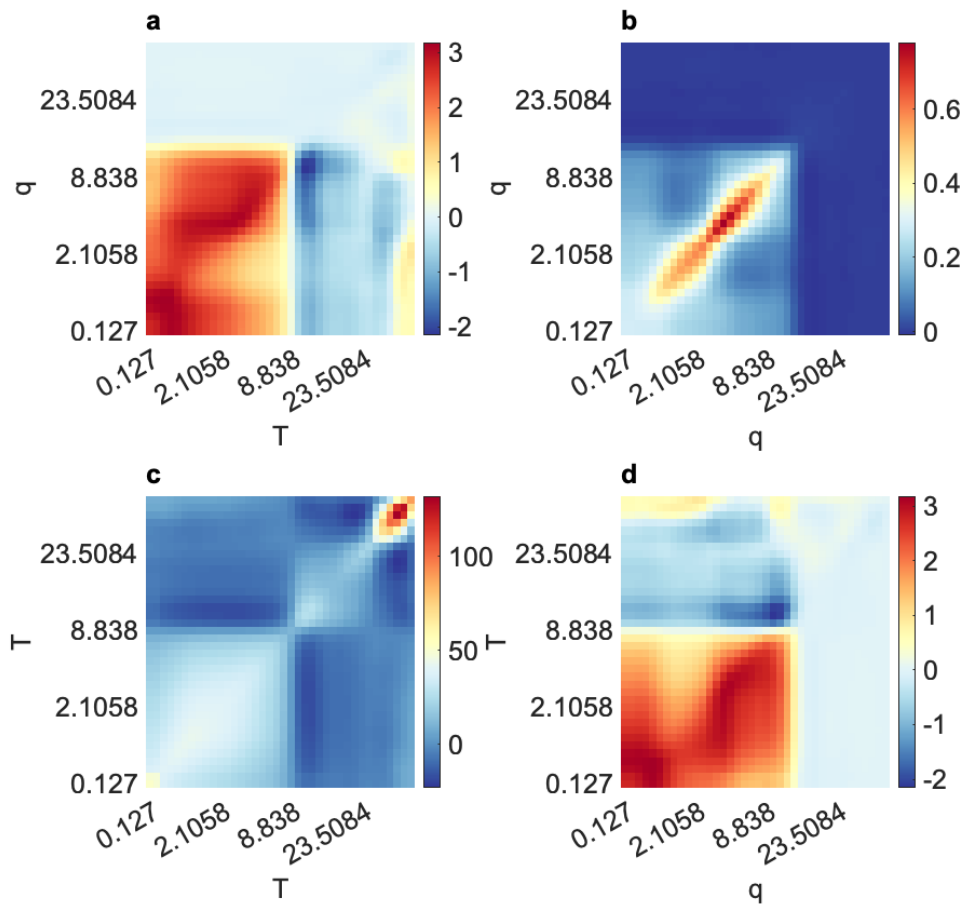

Figure 4.17: *A priori* covariance matrix $\boldsymbol{S_a}$. Here, the label T represents temperature, and q represents the logarithm of the water vapor concentration. All units along the axes are in km.

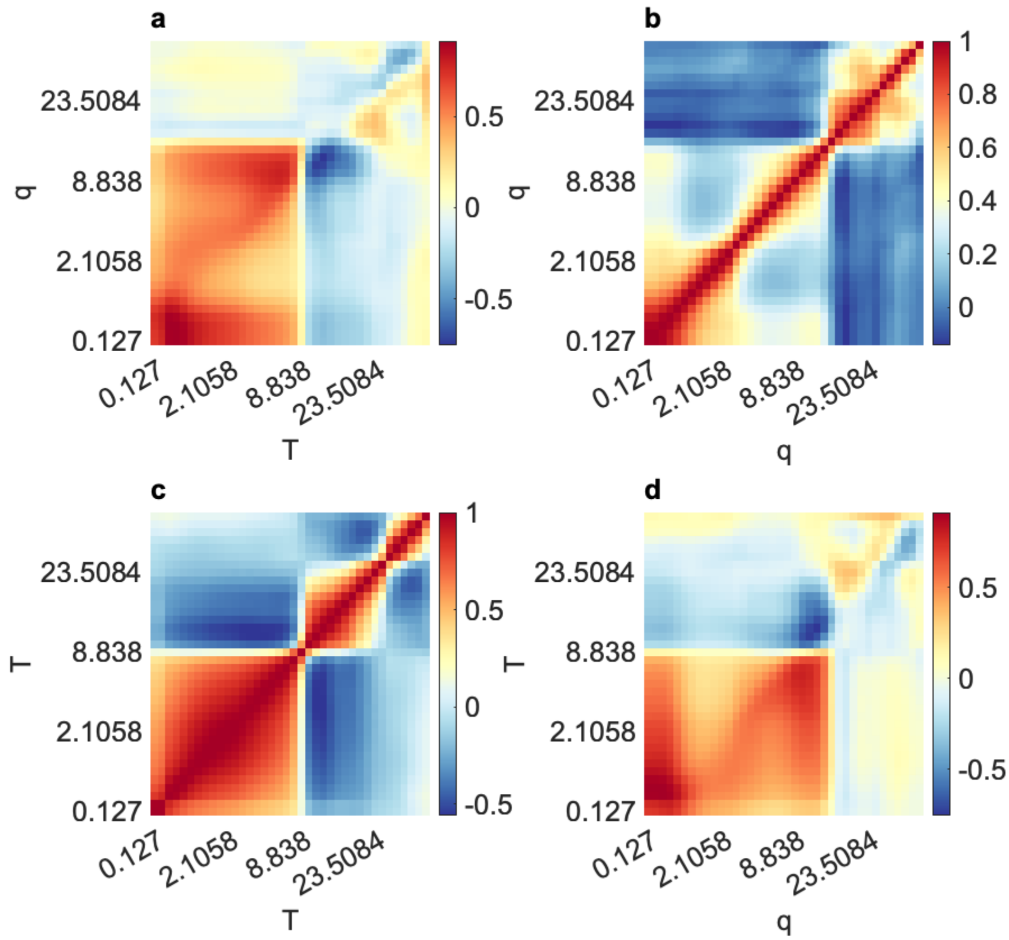

Figure 4.18: *A priori* correlation coefficient matrix $\boldsymbol{C_a}$. Here, the label T represents temperature, and q represents the logarithm of the water vapor concentration. All units along the axes are in km.

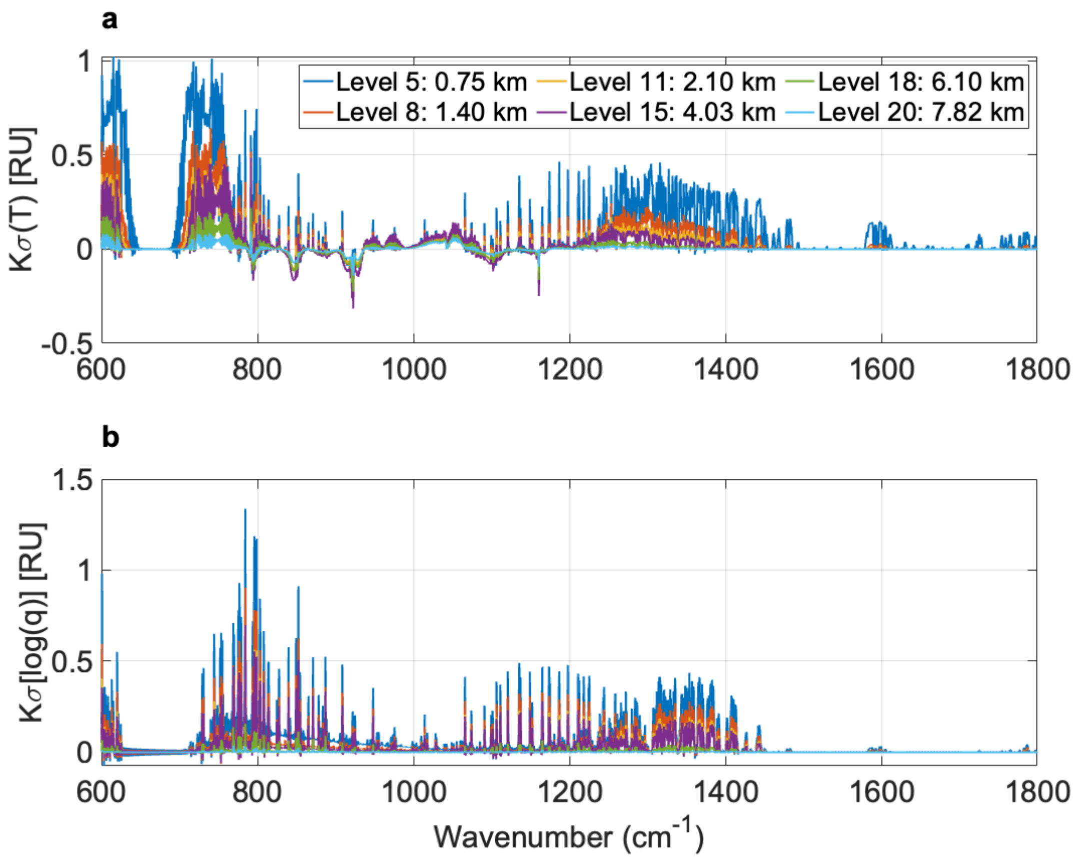

Figure 4.19: (a) $\boldsymbol{K_{AERI,T}} \times \sigma(\boldsymbol{T})$ at selected levels. This shows the product of the temperature Jacobian, $\boldsymbol{K_{AERI,T}}$, and the standard deviation of the temperature profiles in the *a priori* dataset, $\sigma(\boldsymbol{T})$. (b) $\boldsymbol{K_{AERI,q}} \times \sigma[log(\boldsymbol{q})]$ at selected levels. This presents the product of the water vapor Jacobian, $\boldsymbol{K_{AERI,q}}$, and the standard deviation of the water vapor concentration profiles in the *a priori* dataset, $\sigma[log(\boldsymbol{q})]$. Note that we use the logarithm of water vapor concentration to calculate the water vapor Jacobian.

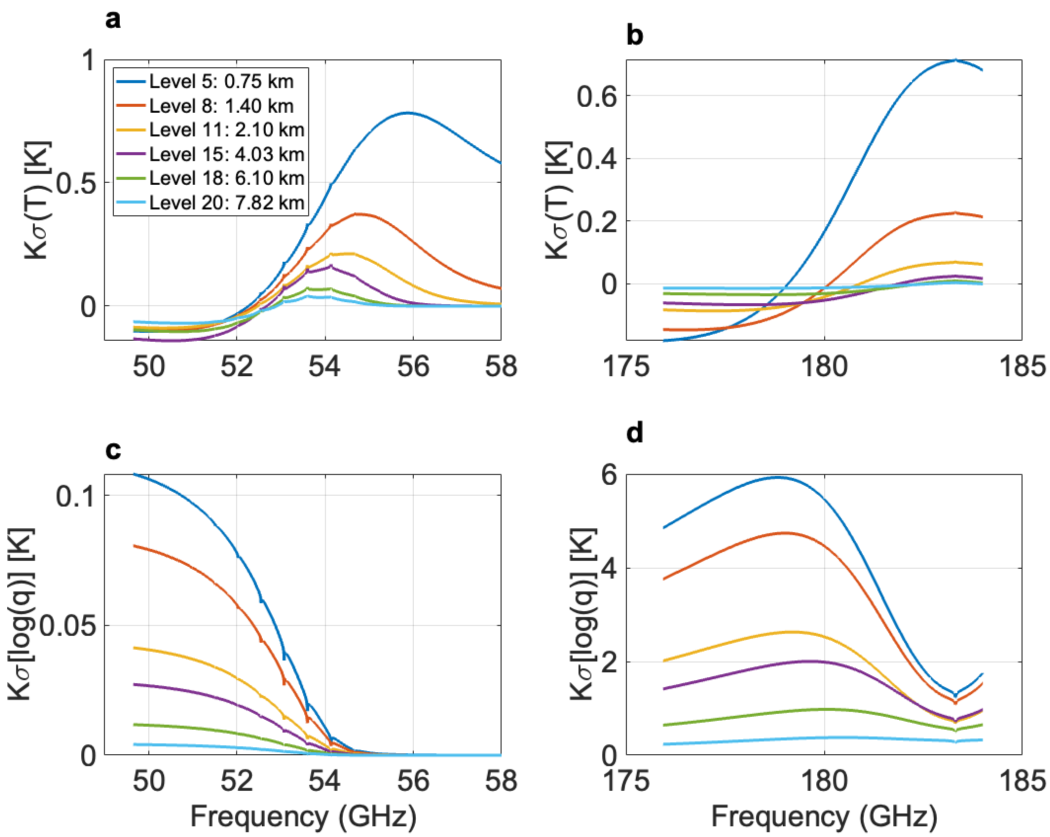

Figure 4.20: The same as Figure 4.19 but for HiSRAMS ground based zenith-pointing Jacobians. (a) $\boldsymbol{K_{HiSRSAMS,T}} \times \sigma(\boldsymbol{T})$ in the oxygen band. (b) $\boldsymbol{K_{HiSRSAMS,T}} \times \sigma(\boldsymbol{T})$ in the water vapor band. (c) $\boldsymbol{K_{HiSRAMS\,,q}} \times \sigma[log(\boldsymbol{q})]$ in the oxygen band. (d) $\boldsymbol{K_{HiSRAMS\,,q}} \times \sigma[log(\boldsymbol{q})]$ in the water vapor band.

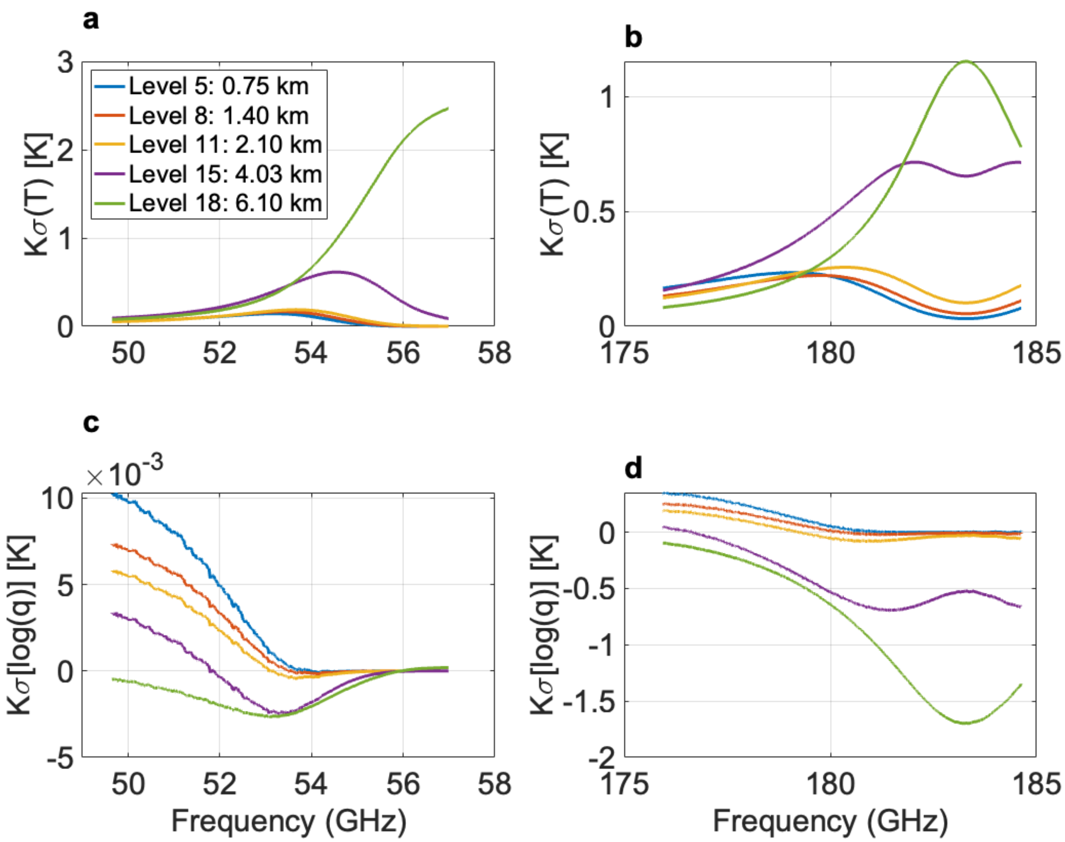

Figure 4.21: The same as Figure 4.20 but for HiSRAMS airborne nadir-pointing Jacobians. The observational height is set at 6.8 km.

Chapter 5 CONCLUSIONS AND FUTURE WORK

Hyperspectral instruments have proven invaluable in detecting and understanding climate change, providing evidence of shifts in the energy balance, insights into the drivers of these changes, and enabling the retrieval of vertical thermodynamic states.

5.1 Summary of Results

The long-term record of downwelling longwave radiance (DLR) observed by the hyperspectral infrared radiometer, Atmospheric Emitted Radiance Interferometer (AERI), has been homogenized at the Southern Great Plains (SGP) site. This long-term "hyperspectral radiative Keeling Curve" is instrumental for its unique capability in detecting and attributing climate change.

Employing a weighted linear regression method, we have identified long-term trends in DLR under various sky conditions at the SGP site. Notably, significant positive trends in DLR across different sky conditions in the temperature-sensitive channels of AERI indicate that ground-based hyperspectral instruments can detect surface warming signals. Furthermore, these long-term trends in DLR reveal climate change signals from various meteorological variables. For instance, a positive trend under clear-sky conditions in the window band suggests an increasing water vapor concentration over time, while negative trends in the all-sky DLR record hint at a cooling effect from cloud changes on the surface.

A pivotal aspect of our research has been the analysis of trend uncertainty, which allowed us to assess the significance level of climate change signals. Our algorithms take into account both measurement uncertainty and interannual variability, revealing that climate change signals in the weak absorption channels of AERI can be detected earlier than surface air temperature warming signals. This early detection is attributed to the reinforcing effects of increases in greenhouse gas concentration and temperature on DLR. We found that interannual variability is the primary contributor to the uncertainty of climate change signals.

The AERI, a rigorously tested and precisely calibrated hyperspectral infrared radiometer, has played a crucial role in various climate change studies. It enables key applications, including the determination of surface greenhouse gas forcings, retrieval of atmospheric thermodynamic states (especially the near-surface temperature and water vapor profiles), and the detection of fog and aerosols, all dependent on AERI's exceptional radiometric accuracy. Demonstrating homogenized long-term DLR records, this study highlights AERI's capability in detecting climate change as an SI-traceable instrument with absolute radiometric precision.

On the other hand, the novel High Spectral Resolution Airborne Microwave Sounder (HiSRAMS) awaits validation of its radiometric accuracy for climate change research applications. Through three field campaigns under clear-sky conditions in Ottawa, Canada, and implementing radiative closure tests, we introduced an innovative method to assess the radiometric accuracy of various hyperspectral instruments. Our findings reveal that, after correcting for a detected warm bias in the window band, AERI demonstrates a relatively minor brightness temperature bias across a wide range of total column optical depths during radiative closure tests. HiSRAMS' nadir-pointing measurements exhibit radiometric accuracy comparable to corrected AERI data. However, its zenith-pointing measurements show lesser radiometric precision, likely due to calibration processes, with brightness temperature bias closely related to environmental temperature.

Following the radiometric validation of both HiSRAMS and AERI, we conducted simultaneous clear-sky temperature and water vapor profile retrievals to evaluate the capability of hyperspectral microwave instrumentation in monitoring atmospheric states. With both instruments stationed on the ground for zenith-pointing measurements, the hyperspectral infrared radiometer outperformed the hyperspectral microwave radiometer in retrieving clear-sky temperature and water vapor in terms of retrieval information content, the retrieval accuracy, and the resolvability of fine vertical features. This superiority is primarily due to the higher signal-to-noise ratio of hyperspectral infrared measurements. Utilizing "sandwich" measurements, which combine ground-based zenith-pointing hyperspectral infrared measurements with airborne nadir-pointing hyperspectral microwave measurements, we achieved enhanced retrieval performance compared to retrievals using a single hyperspectrometer. This synergy resulted in higher information content, reduced retrieval uncertainty, and a more accurate representation of temperature and water vapor profiles, extending from the surface to the altitude of the airborne instrument.

5.2 Future work

The distinctive application of hyperspectral radiative measurements for detecting and understanding climate change, connecting both Earth's energy balance and atmospheric states, warrants further exploration into attributing climate change and evaluating climate models, alongside retrieving all-sky thermodynamic states.

5.2.1 Climate change attribution and global climate model evaluation

Observational data and model simulations are fundamental to advancing our understanding of climate change. Observational radiative records provide us with rich climate change signals, which can be used to evaluate global climate models (GCMs). In turn, the analysis of model radiative outputs, which usually offer better temporal and spatial sampling compared to observations, helps to guide observational efforts.

The long-term trends in DLR observed by AERI at the SGP site encapsulate the climate change signals from a range of meteorological variables, including air temperature, greenhouse gas concentrations, and clouds, underscoring the potential of these observations in separating the impacts of different climatic drivers. A forthcoming objective is to determine the contributions of these meteorological variables to the observed changes in DLR. Despite the spectral overlap of these variables' radiative effects, their unique spectral signatures permit the separation of their individual contributions using the optimal fingerprinting method (Hasselmann, 1997; Huang, Leroy, & Anderson, 2010; Huang, Leroy, Gero, et al., 2010). This approach facilitates the quantification of longwave surface forcings and feedbacks, including those related to CO_2, O_3, water vapor, air temperature, and clouds.

GCMs serve as indispensable tools for identifying climate feedbacks, necessitating accurate evaluation to ensure reliable climate projections. The longwave surface forcings and feedbacks observed at the SGP site provide a benchmark for assessing GCM performance, particularly regarding surface cloud feedback, where observational data can help to address the significant uncertainties present in the models. Analyses of the contributions from various meteorological variables enable us to elucidate the agreement or discrepancy between observational data and GCM outputs, thereby providing insights to refine the models further.

Moreover, our established framework for climate change detection, attribution, and model evaluation—anchored on long-term, spectrally resolved radiance records—holds applicability across a broad array of datasets, whether originating from model outputs or direct observations, at the top of the atmosphere (TOA) or at the surface. For instance, data from the Atmospheric Infrared Sounder offer long-term, spectrally resolved insights into outgoing longwave radiation, allowing an analysis of Earth's energy balance at TOA and aiding in the detection and understanding of climate change from a TOA perspective.

This systematic approach allows for a global analysis of climate change signals, enhancing both regional and global climate change detection and offering guidance for optimizing ground-based observation networks and satellite mission planning, based on model-detected regional climate change patterns. Furthermore, the simulation of future scenarios using GCMs is invaluable for planning the continuous monitoring of climate change.

5.2.2 All-sky temperature and water vapor retrievals

Achieving high temporal frequency in the vertical profiling of temperature and water vapor is essential for detecting long-term climate change, evaluating climate models, and improving weather forecasting. The integration of newly developed hyperspectral instruments into climate studies necessitates a series of methodological steps for successful thermodynamic state retrievals. These steps include developing radiative transfer forward models and retrieval algorithms, conducting field campaigns under desirable weather conditions, performing radiative closure tests to ascertain the instrument's radiometric accuracy, and ultimately conducting thermodynamic vertical profile retrievals. Addressing the radiometric accuracy of HiSRAMS through further calibrations is a priority, given its potential for enhancing the retrieval of all-sky temperature and water vapor profiles.

In light of the unique potential of hyperspectral microwave measurements for comprehensive all-sky retrievals, we intend to construct a cloudy-sky radiative transfer model specific to HiSRAMS, which integrates gas absorption parameterization, surface emissivity models, cloud parameterization schemes, and a radiative solver. Building on this cloudy-sky radiative forward model, we aim to develop a simultaneous retrieval algorithm for HiSRAMS, capable of processing an array of atmospheric variables, including temperature, water vapor, and cloud properties. Furthermore, by examining the synergistic application of hyperspectral microwave and infrared measurements across diverse viewing geometries, we anticipate improvements in the performance of our retrieval operations.

The inclusion of clouds in observational detection introduces significant challenges, primarily due to the difficulty in obtaining reliable cloud truth data necessary for validating radiative forward models and retrieval outcomes. Initiating our efforts with single-layer low cloud field campaigns, which allow for the collection of collocated hyperspectral measurements (from both AERI and HiSRAMS), in-situ cloud observations, and radiosonde data, presents a pragmatic starting point. Following a methodology similar to the workflow established for clear-sky HiSRAMS measurements, we aim to evaluate the performance of the all-sky HiSRAMS radiative forward model through radiative closure tests, subsequently performing comprehensive all-sky temperature, water vapor, and cloud retrievals based on a combination of hyperspectral measurements.

BIBLIOGRAPHY

Aires, F., Prigent, C., Orlandi, E., Milz, M., Eriksson, P., Crewell, S., Lin, C. C., & Kangas, V. (2015). Microwave hyperspectral measurements for temperature and humidity atmospheric profiling from satellite: The clear-sky case. *Journal of Geophysical Research: Atmospheres, 120*(21), 11,334-311,351.

Allan, R. P., Willett, K. M., John, V. O., & Trent, T. (2022). Global changes in water vapor 1979–2020. *Journal of Geophysical Research: Atmospheres*, *127*(12), e2022JD036728.

Allen, G., Illingworth, S., O'Shea, S. J., Newman, S., Vance, A., Bauguitte, S.-B., et al. (2014). Atmospheric composition and thermodynamic retrievals from the ARIES airborne TIR-FTS system–Part 2: Validation and results from aircraft campaigns. *Atmospheric Measurement Techniques, 7*(12), 4401-4416.

Andrews, T., Forster, P. M., & Gregory, J. M. (2009). A surface energy perspective on climate change. *Journal of Climate*, *22*(10), 2557-2570.

Aumann, H. H., & Strow, L. (2001). AIRS, the first hyper-spectral infrared sounder for operational weather forecasting. Paper presented at the 2001 IEEE Aerospace Conference Proceedings (Cat. No. 01TH8542), Big Sky, USA.

Auriacombe, O., Bliankinshtein, N., Gabriel, P., Wolde, M., Huang, Y., Embretsén, J., et al. (2022). High Spectral Resolution Airborne Microwave Sounder (HiSRAMS). Paper presented at the 2022 47th International Conference on Infrared, Millimeter and Terahertz Waves (IRMMW-THz), Delft, Netherlands.

Bani Shahabadi, M., & Huang, Y. (2014). Measuring stratospheric H2O with an airborne spectrometer. *Journal of Atmospheric and Oceanic Technology, 31*(7), 1502-1515.

Barrientos-Velasco, C., Deneke, H., Hünerbein, A., Griesche, H. J., Seifert, P., & Macke, A.

(2022). Radiative closure and cloud effects on the radiation budget based on satellite and shipborne observations during the Arctic summer research cruise, PS106. *Atmospheric Chemistry and Physics, 22*(14), 9313-9348.

Blackwell, W. J., Bickmeier, L. J., Leslie, R. V., Pieper, M. L., Samra, J. E., Surussavadee, C., & Upham, C. A. (2010). Hyperspectral microwave atmospheric sounding. *IEEE Transactions on Geoscience and Remote Sensing, 49*(1), 128-142.

Bliankinshtein, N., Gabriel, P., Auriacombe, O., Huang, Y., Wolde, M., Xu, S., Liu, L., & Angevain, J.-C. (2023). Radiometric calibration of a hyperspectral microwave sounder. Paper presented at the 48th International Conference on Infrared, Millimeter and Terahertz Waves (IRMMW-THz), Montreal, Canada.

Bliankinshtein, N., Gabriel, P., Huang, Y., Wolde, M., Olvhammar, S., Emrich, A., Kores, M., & Midthassel, R. (2019). Airborne Measurements of Polarized Hyperspectral Microwave Radiances to Increase the Accuracy of Temperature and Water Vapor Retrievals: an Information Content Analysis. Paper presented at the AGU Fall Meeting Abstracts, San Francisco, USA.

Bliankinshtein, N., Gabriel, P., Wolde, M., Huang, Y., Embretsen, J., Krus, M., & Angevain, J.-C. (2022). HiSRAMS flight tests and radiation closure. Paper presented at the 2022 ESA Living Planet Symposium, Bonn, Germany.

Bliankinshtein, N., Liu, L., Gabriel, P., Xu, S., Bala, K., Wolde, M., et al. (2023). Airborne validation of HiSRAMS atmospheric soundings. Paper presented at the 2023 IEEE International Geoscience and Remote Sensing Symposium (IGARSS), Pasadena, USA.

Blumberg, W., Turner, D., Löhnert, U., & Castleberry, S. (2015). Ground-based temperature and humidity profiling using spectral infrared and microwave observations. Part II: Actual retrieval performance in clear-sky and cloudy conditions. *Journal of Applied Meteorology and Climatology, 54*(11), 2305-2319.

Blumberg, W., Wagner, T., Turner, D., & Correia, J. (2017). Quantifying the accuracy and uncertainty of diurnal thermodynamic profiles and convection indices derived from the Atmospheric Emitted Radiance Interferometer. *Journal of Applied Meteorology and Climatology, 56*(10), 2747-2766.

Brindley, H., & Bantges, R. (2016). The spectral signature of recent climate change. *Current Climate Change Reports, 2*(3), 112-126.

Carminati, F., Xiao, X., Lu, Q., Atkinson, N., & Hocking, J. (2019). Assessment of the hyperspectral infrared atmospheric sounder (HIRAS). *Remote Sensing, 11*(24), 2950.

Cess, R. D. (1974). Radiative transfer due to atmospheric water vapor: Global considerations of the earth's energy balance. *Journal of Quantitative Spectroscopy and Radiative Transfer*, *14*(9), 861-871.

Clerbaux, C., Boynard, A., Clarisse, L., George, M., Hadji-Lazaro, J., Herbin, H., et al. (2009). Monitoring of atmospheric composition using the thermal infrared IASI/MetOp sounder. *Atmospheric Chemistry and Physics*, *9*(16), 6041-6054.

Clough, S., Brown, P., Miller, N., Liljegren, J., & Shippert, T. (1994). Residual analysis of surface spectral radiances between instrument observations and line-by-line calculations. Paper presented at the Proceedings of the Fourth Atmospheric Radiation Measurement (ARM) science team meeting, Charleston, USA.

Clough, S. A., Shephard, M. W., Mlawer, E. J., Delamere, J. S., Iacono, M. J., Cady-Pereira, K., Boukabara, S., & Brown, P. D. (2005). Atmospheric radiative transfer modeling: a summary of the AER codes. *Journal of Quantitative Spectroscopy and Radiative*

Transfer, 91(2), 233-244.

Colman, R. (2015). Climate radiative feedbacks and adjustments at the Earth's surface. *Journal of Geophysical Research: Atmospheres*, *120*(8), 3173-3182.

Cunningham, P., & Delany, S. J. (2020). k-Nearest neighbour classifiers: (with Python examples). *arXiv preprint arXiv:2004.04523*.

Delamere, J., Clough, S., Payne, V., Mlawer, E., Turner, D., & Gamache, R. (2010). A far-infrared radiative closure study in the Arctic: Application to water vapor. *Journal of Geophysical Research: Atmospheres, 115*(D17).

Divakarla, M. G., Barnet, C. D., Goldberg, M. D., McMillin, L. M., Maddy, E., Wolf, W., Zhou, L., & Liu, X. (2006). Validation of Atmospheric Infrared Sounder temperature and water vapor retrievals with matched radiosonde measurements and forecasts. *Journal of Geophysical Research: Atmospheres, 111*(D9).

Doherty, G. M., & Newell, R. E. (1984). Radiative effects of changing atmospheric water vapour. *Tellus B: Chemical and Physical Meteorology*, *36*(3), 149-162.

Durre, I., Vose, R. S., & Wuertz, D. B. (2006). Overview of the integrated global radiosonde archive. *Journal of Climate, 19*(1), 53-68.

Eriksson, P., Buehler, S., Davis, C., Emde, C., & Lemke, O. (2011). ARTS, the atmospheric radiative transfer simulator, version 2. *Journal of Quantitative Spectroscopy and Radiative Transfer, 112*(10), 1551-1558.

Feldman, D. R., Collins, W. D., Gero, P. J., Torn, M. S., Mlawer, E. J., & Shippert, T. R. (2015). Observational determination of surface radiative forcing by CO2 from 2000 to 2010. *Nature, 519*(7543), 339-343.

Feldman, D. R., Collins, W. D., Biraud, S., Risser, M., Turner, D., Gero, P. J., et al. (2018).

Observationally derived rise in methane surface forcing mediated by water vapour trends. *Nature Geoscience*, *11*(4), 238-243.

Feltz, W., Smith, W., Howell, H. B., Knuteson, R., Woolf, H., & Revercomb, H. (2003). Near-continuous profiling of temperature, moisture, and atmospheric stability using the Atmospheric Emitted Radiance Interferometer (AERI). *Journal of Applied Meteorology, 42*(5), 584-597.

Feltz, W., Smith, W. L., Knuteson, R. O., Revercomb, H. E., Woolf, H. M., & Howell, H. B. (1998). Meteorological applications of temperature and water vapor retrievals from the ground-based Atmospheric Emitted Radiance Interferometer (AERI). *Journal of Applied Meteorology, 37*(9), 857-875.

Gelaro, R., McCarty, W., Suárez, M. J., Todling, R., Molod, A., Takacs, L., et al. (2017). The modern-era retrospective analysis for research and applications, version 2 (MERRA-2). *Journal of Climate, 30*(14), 5419-5454.

Gero, P. J., & Turner, D. D. (2011). Long-Term Trends in Downwelling Spectral Infrared Radiance over the U.S. Southern Great Plains. *Journal of Climate, 24*(18), 4831-4843.

Guo, J., Yan, Y., Chen, D., Lv, Y., Han, Y., Guo, X., et al. (2020). The response of warm-season precipitation extremes in China to global warming: an observational perspective from radiosonde measurements. *Climate Dynamics, 54*, 3977-3989.

Han, Y., & Westwater, E. R. (1995). Remote sensing of tropospheric water vapor and cloud liquid water by integrated ground-based sensors. *Journal of Atmospheric and Oceanic Technology, 12*(5), 1050-1059.

Hansell, R., Liou, K., Ou, S., Tsay, S., Ji, Q., & Reid, J. (2008). Remote sensing of mineral dust aerosol using AERI during the UAE2: A modeling and sensitivity study. *Journal of*

Geophysical Research: Atmospheres, 113(D18).

Harries, J. E., Brindley, H. E., Sagoo, P. J., & Bantges, R. J. (2001). Increases in greenhouse forcing inferred from the outgoing longwave radiation spectra of the Earth in 1970 and 1997. *Nature, 410*(6826), 355-357.

Hasselmann, K. (1997). Multi-pattern fingerprint method for detection and attribution of climate change. *Climate Dynamics*, *13*, 601-611.

Hersbach, H., Bell, B., Berrisford, P., Hirahara, S., Horányi, A., Muñoz-Sabater, J., et al. (2020). The ERA5 global reanalysis. *Quarterly Journal of the Royal Meteorological Society, 146*(730), 1999-2049.

Hilliard, L., Racette, P., Blackwell, W., Galbraith, C., & Thompson, E. (2013). Hyperspectral Microwave Atmospheric Sounder (HyMAS) architecture and design accommodations. Paper presented at the 2013 IEEE Aerospace Conference, Big Sky, USA.

Hilton, F., Armante, R., August, T., Barnet, C., Bouchard, A., Camy-Peyret, C., et al. (2012). Hyperspectral Earth observation from IASI: Five years of accomplishments. *Bulletin of the American Meteorological Society*, *93*(3), 347-370.

Holdridge, D. (2020). Balloon-borne sounding system (SONDE) instrument handbook. In R. Stafford (Ed.), (Ed.). U.S. Department of Energy. DOE/SC-ARM/TR-029.

Huang, Y. (2013a). A simulated climatology of spectrally decomposed atmospheric infrared radiation. *Journal of Climate, 26*(5), 1702-1715.

Huang, Y. (2013b). On the longwave climate feedbacks. *Journal of Climate*, 26(19), 7603-7610.

Huang, Y., & Bani Shahabadi, M. (2014). Why logarithmic? A note on the dependence of radiative forcing on gas concentration. *Journal of Geophysical Research: Atmospheres, 119*(24), 13,683-613,689.

Huang, Y., Chou, G., Xie, Y., & Soulard, N. (2019). Radiative control of the interannual variability of arctic sea ice. *Geophysical Research Letters, 46*(16), 9899-9908. https://doi.org/10.1029/2019gl084204

Huang, Y., Leroy, S. S., & Anderson, J. G. (2010). Determining longwave forcing and feedback using infrared spectra and GNSS radio occultation. *Journal of Climate, 23*(22), 6027-6035.

Huang, Y., Leroy, S., Gero, P. J., Dykema, J., & Anderson, J. (2010). Separation of longwave climate feedbacks from spectral observations. *Journal of Geophysical Research: Atmospheres*, *115*(D7).

Huang, Y., & Ramaswamy, V. (2009). Evolution and Trend of the Outgoing Longwave Radiation Spectrum. *Journal of Climate, 22*(17), 4637-4651.

Huang, Y., Ramaswamy, V., Huang, X., Fu, Q., & Bardeen, C. (2007). A strict test in climate modeling with spectrally resolved radiances: GCM simulation versus AIRS observations. *Geophysical Research Letters, 34*(24).

Huang, Y., Ramaswamy, V., & Soden, B. (2007). An investigation of the sensitivity of the clear-sky outgoing longwave radiation to atmospheric temperature and water vapor. *Journal of Geophysical Research, 112*(D5).

Inness, A., Ades, M., Agustí-Panareda, A., Barré, J., Benedictow, A., Blechschmidt, A.-M., et al. (2019). The CAMS reanalysis of atmospheric composition. *Atmospheric Chemistry and Physics, 19*(6), 3515-3556.

Jacobson, A. R., Schuldt, K. N., Miller, J. B., Oda, T., Tans, P., Arlyn, A., et al. (2020). CarbonTracker CT2019B. Retrieved from https://www.esrl.noaa.gov/gmd/ccgg/carbontracker/CT2019B/

Kapsch, M.-L., Graversen, R. G., Tjernström, M., & Bintanja, R. (2016). The effect of downwelling longwave and shortwave radiation on Arctic summer sea ice. *Journal of Climate, 29*(3), 1143-1159.

Keeling, C. D., Bacastow, R. B., Bainbridge, A. E., Ekdahl Jr, C. A., Guenther, P. R., Waterman, L. S., & Chin, J. F. (1976). Atmospheric carbon dioxide variations at Mauna Loa observatory, Hawaii. *Tellus*, *28*(6), 538-551.

King, M. D., Kaufman, Y. J., Menzel, W. P., & Tanre, D. (1992). Remote sensing of cloud, aerosol, and water vapor properties from the moderate resolution imaging spectrometer(MODIS). *IEEE Transactions on Geoscience and Remote Sensing, 30*(1), 2-27.

Knuteson, R., Revercomb, H., Best, F., Ciganovich, N., Dedecker, R., Dirkx, T., et al. (2004a). Atmospheric emitted radiance interferometer. Part I: Instrument design. *Journal of Atmospheric and Oceanic Technology, 21*(12), 1763-1776.

Knuteson, R., Revercomb, H., Best, F., Ciganovich, N., Dedecker, R., Dirkx, T., et al. (2004b). Atmospheric emitted radiance interferometer. Part II: Instrument performance. *Journal of Atmospheric and Oceanic Technology, 21*(12), 1777-1789.

Knuteson, R., Whitney, B., Revercomb, H., & Best, F. (1999). The history of the University of Wisconsin Atmospheric Emitted Radiance Interferometer (AERI) prototype during the period April 1994 through July 1995. The University of Wisconsin-Madison, Space Science and Engineering Center.

Lan, X., Tans, P., & Thoning, K. W. (version 2023-06). Trends in globally-averaged CO2 determined from NOAA Global Monitoring Laboratory measurements.

Langland, R. H., & Baker, N. L. (2004). Estimation of observation impact using the NRL atmospheric variational data assimilation adjoint system. *Tellus A: Dynamic Meteorology and Oceanography, 56*(3), 189-201.

Laroche, S., & Sarrazin, R. (2010). Impact study with observations assimilated over North America and the North Pacific Ocean on the MSC global forecast system. Part I: Contribution of radiosonde, aircraft and satellite data. *Atmosphere-ocean, 48*(1), 10-25.

Leroy, S. S., Anderson, J. G., & Ohring, G. (2008). Climate signal detection times and constraints on climate benchmark accuracy requirements. *Journal of Climate, 21*(4), 841-846.

Liebmann, B., & Smith, C. A. (1996). Description of a complete (interpolated) outgoing longwave radiation dataset. *Bulletin of the American Meteorological Society, 77*(6), 1275-1277.

Lin, B., Stackhouse Jr, P. W., Minnis, P., Wielicki, B. A., Hu, Y., Sun, W., Fan, T. F., & Hinkelman, L. M. (2008). Assessment of global annual atmospheric energy balance from satellite observations. *Journal of Geophysical Research: Atmospheres*, *113*(D16).

Liu, L., Bliankinshtein, N., Huang, Y., Gyakum, J. R., Gabriel, P. M., Xu, S., & Wolde, M. (2023). Radiative closure tests of collocated hyperspectral microwave and infrared radiometers. *Atmospheric Measurement Techniques Discussions, 2023*, 1-23.

Liu, L., Huang, Y., Gyakum, J. R., Turner, D. D., & Gero, P. J. (2022). Trends in Downwelling Longwave Radiance over the Southern Great Plains. *Journal of Geophysical Research: Atmospheres, 127*(6), e2021JD035949.

Loeb, N. G., Su, W., & Kato, S. (2016). Understanding climate feedbacks and sensitivity using observations of Earth's energy budget. *Current Climate Change Reports*, *2*, 170-178.

Loeb, N. G., Doelling, D. R., Wang, H., Su, W., Nguyen, C., Corbett, J. G., et al. (2018). Clouds and the earth's radiant energy system (CERES) energy balanced and filled (EBAF) top-of-atmosphere (TOA) edition-4.0 data product. *Journal of Climate*, *31*(2), 895-918.

Loveless, D. M. (2021). Developing a Synergy Between Space-based Infrared Sounders and the Ground-based Atmospheric Emitted Radiance Interferometer (AERI) to Improve Thermodynamic Profiling of the Planetary Boundary Layer. The University of Wisconsin-Madison.

Loveless, D. M., Wagner, T. J., Knuteson, R. O., Turner, D. D., & Ackerman, S. A. (2022). Information Content of a Synergy of Ground-Based and Space-Based Infrared Sounders. Part I: Clear-Sky Environments. *Journal of Atmospheric and Oceanic Technology, 39*(6), 771-787.

Lubin, D. (1994). The role of the tropical super greenhouse effect in heating the ocean surface. *Science, 265*(5169), 224-227.

McNally, A., & Watts, P. (2003). A cloud detection algorithm for high-spectral-resolution infrared sounders. *Quarterly Journal of the Royal Meteorological Society: A journal of the atmospheric sciences, applied meteorology and physical oceanography, 129*(595), 3411-3423.

Palchetti, L., Brindley, H., Bantges, R., Buehler, S., Camy-Peyret, C., Carli, B., et al. (2020). unique far-infrared satellite observations to better understand how Earth radiates energy to space. *Bulletin of the American Meteorological Society, 101*(12), E2030-E2046.

Pan, F., Huang, X., Strow, L. L., & Guo, H. (2015). Linear trends and closures of 10-yr observations of AIRS stratospheric channels. *Journal of Climate, 28*(22), 8939-8950.

Peters, W., Jacobson, A. R., Sweeney, C., Andrews, A. E., Conway, T. J., Masarie, K., et al. (2007). An atmospheric perspective on North American carbon dioxide exchange:

CarbonTracker. *Proceedings of the National Academy of Sciences, 104*(48), 18925-18930.

Petzold, A., Thouret, V., Gerbig, C., Zahn, A., Brenninkmeijer, C. A., Gallagher, M., et al. (2015). Global-scale atmosphere monitoring by in-service aircraft–current achievements and future prospects of the European Research Infrastructure IAGOS. *Tellus B: Chemical and Physical Meteorology, 67*(1), 28452.

Pougatchev, N., August, T., Calbet, X., Hultberg, T., Oduleye, O., Schlüssel, P., et al. (2009). IASI temperature and water vapor retrievals–error assessment and validation. *Atmospheric Chemistry and Physics*, *9*(17), 6453-6458.

Revercomb, H. E., Buijs, H., Howell, H. B., LaPorte, D. D., Smith, W. L., & Sromovsky, L. (1988). Radiometric calibration of IR Fourier transform spectrometers: solution to a problem with the High-Resolution Interferometer Sounder. *Applied Optics, 27*(15), 3210-3218.

Revercomb, H. E., Turner, D. D., Tobin, D., Knuteson, R. O., Feltz, W., Barnard, J., et al. (2003). The ARM program's water vapor intensive observation periods: Overview, initial accomplishments, and future challenges. *Bulletin of the American Meteorological Society, 84*(2), 217-236.

Rodgers, C. D. (2000). Inverse methods for atmospheric sounding: theory and practice (Vol. 2): World scientific.

Rosenkranz, P. (2017). Line-by-line microwave radiative transfer (non-scattering): Remote Sensing Code Library.

Rowe, P. M., Neshyba, S. P., Cox, C. J., & Walden, V. P. (2011). A responsivity-based criterion for accurate calibration of FTIR emission spectra: identification of in-band low-responsivity wavenumbers. *Optics express, 19*(7), 5930-5941.

Rowe, P. M., Neshyba, S. P., & Walden, V. P. (2011). Responsivity-based criterion for accurate calibration of FTIR emission spectra: theoretical development and bandwidth estimation. *Optics express, 19*(6), 5451-5463.

Seo, J., Choi, H., & Oh, Y. (2022). Potential of AOD Retrieval Using Atmospheric Emitted Radiance Interferometer (AERI). *Remote Sensing, 14*(2), 407.

Shupe, M. D., & Intrieri, J. M. (2004). Cloud Radiative Forcing of the Arctic Surface: The Influence of Cloud Properties, Surface Albedo, and Solar Zenith Angle. *Journal of Climate, 17*(3), 616-628.

Simmer, C. (1999). Contribution of microwave remote sensing from satellites to studies on the Earth energy budget and the hydrological cycle. *Advances in Space Research*, 24(7), 897-905.

Smith, W. L., Revercomb, H., Weisz, E., Tobin, D., Knuteson, R., Taylor, J., & Menzel, W. P. (2021). Hyperspectral satellite radiance atmospheric profile information content and its dependence on spectrometer technology. *IEEE Journal of Selected Topics in Applied Earth Observations and Remote Sensing, 14*, 4720-4736.

Soden, B. J., Held, I. M., Colman, R., Shell, K. M., Kiehl, J. T., & Shields, C. A. (2008). Quantifying climate feedbacks using radiative kernels. *Journal of Climate*, *21*(14), 3504-3520.

Sokolowsky, G. A., Clothiaux, E. E., Baggett, C. F., Lee, S., Feldstein, S. B., Eloranta, E. W., et al. (2020). Contributions to the Surface Downwelling Longwave Irradiance during Arctic Winter at Utqiaġvik (Barrow), Alaska. *Journal of Climate, 33*(11), 4555-4577.

Stephens, G. L., Li, J., Wild, M., Clayson, C. A., Loeb, N., Kato, S., et al. (2012). An update on

Earth's energy balance in light of the latest global observations. *Nature Geoscience, 5*(10), 691-696.

Stubenrauch, C., Cros, S., Guignard, A., & Lamquin, N. (2010). A 6-year global cloud climatology from the Atmospheric InfraRed Sounder AIRS and a statistical analysis in synergy with CALIPSO and CloudSat. *Atmospheric Chemistry and Physics, 10*(15), 7197-7214.

Susskind, J., Barnet, C. D., & Blaisdell, J. M. (2003). Retrieval of atmospheric and surface parameters from AIRS/AMSU/HSB data in the presence of clouds. *IEEE Transactions on Geoscience and Remote Sensing*, *41*(2), 390-409.

Susskind, J., Blaisdell, J. M., Iredell, L., & Keita, F. (2010). Improved temperature sounding and quality control methodology using AIRS/AMSU data: The AIRS science team version 5 retrieval algorithm. *IEEE Transactions on Geoscience and Remote Sensing*, *49*(3), 883-907.

Thorne, P. W., Lanzante, J. R., Peterson, T. C., Seidel, D. J., & Shine, K. P. (2011). Tropospheric temperature trends: History of an ongoing controversy. *Wiley Interdisciplinary Reviews: Climate Change, 2*(1), 66-88.

Tiao, G. C., Reinsel, G. C., Xu, D., Pedrick, J., Zhu, X., Miller, A., et al. (1990). Effects of autocorrelation and temporal sampling schemes on estimates of trend and spatial correlation. *Journal of Geophysical Research: Atmospheres, 95*(D12), 20507-20517.

Toporov, M., & Löhnert, U. (2020). Synergy of satellite-and ground-based observations for continuous monitoring of atmospheric stability, liquid water path, and integrated water vapor: Theoretical evaluations using reanalysis and neural networks. *Journal of Applied Meteorology and Climatology*, *59*(7), 1153-1170.

Trenberth, K. E., Fasullo, J. T., & Kiehl, J. (2009). Earth's Global Energy Budget. *Bulletin of the American Meteorological Society, 90*(3), 311-324.

Turner, D. D. (2003). Microphysical properties of single and mixed-phase Arctic clouds derived from ground-based AERI observations. The University of Wisconsin-Madison.

Turner, D. D., & Blumberg, W. G. (2018). Improvements to the AERIoe thermodynamic profile retrieval algorithm. *IEEE Journal of Selected Topics in Applied Earth Observations and Remote Sensing, 12*(5), 1339-1354.

Turner, D. D., Feltz, W. F., & Ferrare, R. A. (2000). Continuous water vapor profiles from operational ground-based active and passive remote sensors. *Bulletin of the American Meteorological Society, 81*(6), 1301-1318.

Turner, D., Knuteson, R., Revercomb, H., Lo, C., & Dedecker, R. (2006). Noise reduction of Atmospheric Emitted Radiance Interferometer (AERI) observations using principal component analysis. *Journal of Atmospheric and Oceanic Technology, 23*(9), 1223-1238.

Turner, D. D., & Gero, P. J. (2011). Downwelling 10µm radiance temperature climatology for the Atmospheric Radiation Measurement Southern Great Plains site. *Journal of Geophysical Research, 116*(D8).

Turner, D. D., Lesht, B. M., Clough, S. A., Liljegren, J. C., Revercomb, H. E., & Tobin, D. (2003). Dry bias and variability in Vaisala RS80-H radiosondes: The ARM experience. *Journal of Atmospheric and Oceanic Technology, 20*(1), 117-132.

Turner, D. D., & Löhnert, U. (2014). Information content and uncertainties in thermodynamic profiles and liquid cloud properties retrieved from the ground-based Atmospheric Emitted Radiance Interferometer (AERI). *Journal of Applied Meteorology and Climatology, 53*(3), 752-771.

Turner, D. D., & Löhnert, U. (2021). Ground-based temperature and humidity profiling: combining active and passive remote sensors. *Atmospheric Measurement Techniques, 14*(4), 3033-3048.

Turner, D. D., Tobin, D., Clough, S. A., Brown, P. D., Ellingson, R. G., Mlawer, E. J., et al. (2004). The QME AERI LBLRTM: A closure experiment for downwelling high spectral resolution infrared radiance. *Journal of the atmospheric sciences, 61*(22), 2657-2675.

Vuille, M., & Bradley, R. S. (2000). Mean annual temperature trends and their vertical structure in the tropical Andes. *Geophysical Research Letters*, *27*(23), 3885-3888.

Wang, J., Cole, H. L., Carlson, D. J., Miller, E. R., Beierle, K., Paukkunen, A., & Laine, T. K. (2002). Corrections of humidity measurement errors from the Vaisala RS80 radiosonde—Application to TOGA COARE data. *Journal of Atmospheric and Oceanic Technology, 19*(7), 981-1002.

Wang, J., Dai, A., & Mears, C. (2016). Global water vapor trend from 1988 to 2011 and its diurnal asymmetry based on GPS, radiosonde, and microwave satellite measurements. *Journal of Climate, 29*(14), 5205-5222.

Warwick, L., Brindley, H., Di Roma, A., Fox, S., Havemann, S., Murray, J., et al. (2022). Retrieval of Tropospheric Water Vapor From Airborne Far-Infrared Measurements: A Case Study. *Journal of Geophysical Research: Atmospheres, 127*(7), e2020JD034229.

Weatherhead, E. C., Reinsel, G. C., Tiao, G. C., Meng, X.-L., Choi, D., Cheang, W.-K., et al. (1998). Factors affecting the detection of trends: Statistical considerations and applications to environmental data. *Journal of Geophysical Research: Atmospheres, 103*(D14), 17149-17161.

Westwater, E. R. (1997). Remote sensing of tropospheric temperature and water vapor by integrated observing systems: The remote sensing lecture. *Bulletin of the American Meteorological Society, 78*(9), 1991-2006.

Wielicki, B. A., Wong, T., Allan, R. P., Slingo, A., Kiehl, J. T., Soden, B. J., et al. (2002). Evidence for large decadal variability in the tropical mean radiative energy budget. *Science, 295*(5556), 841-844.

Wild, M., Folini, D., Schär, C., Loeb, N., Dutton, E. G., & König-Langlo, G. (2012). The global energy balance from a surface perspective. *Climate Dynamics, 40*(11-12), 3107-3134.

Xu, S., Bliankinshtein, N., Gabriel, P., Liu, L., Wolde, M., Huang, Y., et al. (2023). Low-level processing of passive hyperspectral microwave measurements from HiSRAMS. Paper presented at the 2023 IEEE International Geoscience and Remote Sensing Symposium (IGARSS), Pasadena, USA.

Zhao, H., Ma, X., Jia, G., Mi, Z., & Ji, H. (2022). Synergistic Retrieval of Temperature and Humidity Profiles from Space-Based and Ground-Based Infrared Sounders Using an Optimal Estimation Method. *Remote Sensing, 14*(20), 5256.

Zhou, C., Wang, J., Dai, A., & Thorne, P. W. (2021). A new approach to homogenize global subdaily radiosonde temperature data from 1958 to 2018. *Journal of Climate, 34*(3), 1163-1183.